UNIVERSITY OF NAPLES " Federico II "

PhD Program in Fundamental and Applied Physics

XXIV cycle

Candidate: Srdjan SARIKAS

Neutrino Oscillations at High Densities: Cosmological and Astrophysical Aspects

Advisors : Dr. Gianpiero MANGANO - INFN Naples
Prof. Gennaro MIELE - INFN Naples
- University "Federico II"

Contents

Introduction

In the era of the quest for physics beyond the Standard Model, the discovery of neutrino oscillations is celebrated as the first direct observation that we are on the right path. The first hints of this effect came from the detection of neutrinos from the sun.From the beginning of the 1970s until the late 1990s, all measurements of the solar neutrino flux yielded values two or three times lower than expected. This discrepancy was known as the solar neutrino problem. The work of Wolfenstein (1977), and Mikheev and Smirnov (1986) offered an explanation in terms of the neutrino oscillations in matter, but the alternative explanations in terms of the inefficiency of detection, poorly understood nuclear cross sections and flaws in the solar model were given preference.

The first clear signature of neutrino oscillations came in 1998, when the Super-Kamiokande collaboration published indications of so-called atmospheric oscillations: In the decay cascade of primary cosmic rays in the atmosphere a large number of GeV muon neutrinos are produced. Since the flux of cosmic rays is isotropic, the flux of neutrinos should be isotropic as well. The measured flux of the sub-GeV ν_μ's indeed was isotropic, but for the GeV energies the flux showed a clear zenith-angle dependence with a substantial up–down asymmetry. This could be explained only by the oscillations of the up-going neutrinos as they travel through the earth.

Shortly after, physicists were able to tag neutral current events, and the results of the Sudbury neutrino observatory showed that electron neutrinos were *de facto* less abundant in the total solar flux: More than half of the electron neutrinos produced in the interior of the sun changed flavor while propagating through its outer layers, exactly as theorized by Wolfenstein, Mikheev and Smirnov. These two measurements were milestones in the development of neutrino physics.

It was not long before physicists conducted the oscillation experiments with completely controlled sources. Today we measure the parameters of neutrino mixing with percent level uncertainty, but there are still questions to be answered. What is the absolute scale of the neutrino masses. What is their relative arrangement? Are neutrinos their own antiparticles? The data we did acquire so far are enough to influence the astrophysics and cosmology. That is why today we discuss the cosmological upper bounds on absolute masses, and determining the number of neutrino families with cosmological tools such as big bang nucleosynthesis and cosmic microwave background analysis. We may even extract information on the neutrino mass hierarchy from a next supernova explosion.

Much of these questions refer to systems that are much denser than anything we can create on earth. For example, the density in the core of a supernova can reach 10^{12} g/cm^3! In such extreme conditions, the difference between interaction and propagation states makes neutrino evolution highly nontrivial and sometimes counter intuitive. Who would have thought that two species that mix in vacuum do not mix in the presence of asymmetries at high densities? Or that they can completely swap spectra while streaming from a supernova core? The thorough treatment of neutrino oscillations at high densities is a necessary prerequisite to extracting their properties from observations.

My doctoral work focused neutrinos in two environments: (*i*) in the early Universe, with an emphasis on their role during primordial nucleosynthesis; and (*ii*) the free-stream regime from a supernova core, with special attention paid to analytic and semi-analytic aspects of the problem.

In the first chapter, I give a general framework for the physics of neutrino oscillations. The second and third chapters are devoted to the cosmological role of neutrinos during the primordial nucleosynthesis with and without large asymmetries. I show in the second chapter how various observations of primordial abundances point to different numbers of relativistic degrees of freedom in the early Universe. The third chapter clears the ground for the next precision measurements of the cosmic microwave background, such as Planck, that will provide independent and complementary answers to the same question. I show what is the maximal contribution of asymmetric neutrinos to the total energy density of the Universe and make a clear statement on the significance of the future Planck measurement.

The next two chapters are devoted to the treatment of neutrinos streaming from a supernova. In the fourth, I explain the general framework of supernova physics and the evolution of neutrino fluxes. I concentrate on the effects we expect and the numerical problems present. In the fifth chapter, I present the stability analysis and the semi-analytical solution it gives for questions posed in the previous chapter.

CHAPTER 1

Neutrino oscillations at high densities

1.1 Neutrinos in SM

In the standard model neutrinos appear as members of the weak isospin doublets:

$$\begin{pmatrix}\nu_e\\ e\end{pmatrix}_L \quad \begin{pmatrix}\nu_\mu\\ \mu\end{pmatrix}_L \quad \begin{pmatrix}\nu_\tau\\ \tau\end{pmatrix}_L \quad . \tag{1.1}$$

They are introduced as massless, exclusively left-handed fermions, which interact only weakly. With Z boson though the neutral current and with W bosons through the charged current

$$\mathcal{L}_{\text{weak}} = -\frac{g}{\cos\theta_{\text{w}}}\, Z_\mu J^\mu_{\text{NC}} - \frac{g}{\sqrt{2}}\left(W^+_\mu J^\mu_{\text{CC}} + W^-_\mu J^{\mu\dagger}_{\text{CC}}\right) \quad , \tag{1.2}$$

where g is the coupling constant of the $SU(2)_L$ group and θ_{w} is the Weinberg angle. The charged and neutral currents are

$$\begin{aligned} J^\mu_{\text{CC}} &= \bar{\nu}_{l\,L}\,\gamma^\mu\, l_L + \text{quark terms} \quad , \\ J^\mu_{\text{NC}} &= \frac{1}{2}\,\bar{\nu}_{l\,L}\,\gamma^\mu\,\nu_{l\,L} - \frac{1}{2}\,\bar{l}_L\,\gamma^\mu\, l_L + \sin^2\theta_{\text{w}}\,\bar{l}_L\,\gamma^\mu\, l_L + \text{quark terms} \quad , \end{aligned} \tag{1.3}$$

where the index l runs through three lepton generations $l = e, \mu, \tau$. The quark terms are omitted for brevity.

At energies well below the masses of the gauge bosons ($E \lesssim 100$ GeV), it is safe to integrate them out and obtain an effective description, the 4-fermions point interaction, as proposed by Fermi before the fundamental theory:

$$\mathcal{L}_{\text{eff}} = -\frac{4\,G_{\text{F}}}{\sqrt{2}}\left(J^\mu_{\text{NC}}\, J^\dagger_{\text{NC}\mu} + J^\mu_{\text{CC}}\, J^\dagger_{\text{CC}\mu}\right) \quad , \tag{1.4}$$

where Fermi constant G_{F} in close relation with the mass of the W boson m_{w}

$$G_{\text{F}} = \frac{g^2}{4\sqrt{2}\, m^2_{\text{w}}} = 1.166 \times 10^{-5}\,\text{GeV}^{-2} \quad . \tag{1.5}$$

1.2 Neutrino Oscillations

In Eq. 1.3 it evident that only left chiral components of neutrinos interact. In fact, as originally proposed by Glashow, Salam and Weinberg, the model of electroweak interaction did not need right-handed neutrinos, because neutrinos were taken to be massless. Even before the Standard Electroweak Model, during the 1960's, Maki, Nakagawa and Sakata [Maki 1962] and independently Pontecorvo [Pontecorvo 1968] proposed that neutrinos could have non-zero masses and that their mass eigenstates need not coincide with their interaction eigenstates. Therefore, we could observe mixing between different neutrino flavors. Since then, numerous experiments have observed neutrino oscillations, proving that neutrinos have mass.

1.2.1 Neutrino masses and mixings

Neutrino flavor eigenstates $(\nu_e, \nu_\mu, \nu_\tau)$ and mass eigenstates (ν_1, ν_2, ν_3) are related through a 3×3 matrix U

$$\begin{pmatrix} \nu_e \\ \nu_\mu \\ \nu_\tau \end{pmatrix} = U \begin{pmatrix} \nu_1 \\ \nu_2 \\ \nu_3 \end{pmatrix} \quad . \tag{1.6}$$

If neutrinos are Dirac particles, the transformation is unitary and it is convenient to parametrize the mixing matrix in terms of three mixing angles θ_{12}, θ_{23}, θ_{13} and one CP-violating phase δ

$$U = \begin{pmatrix} c_{12} & s_{12} & 0 \\ -s_{12} & c_{12} & 0 \\ 0 & 0 & 1 \end{pmatrix} \begin{pmatrix} c_{13} & 0 & s_{13}e^{-\mathrm{i}\delta} \\ 0 & 1 & 0 \\ -s_{13}e^{\mathrm{i}\delta} & 0 & c_{13} \end{pmatrix} \begin{pmatrix} 1 & 0 & 0 \\ 0 & c_{23} & s_{23} \\ 0 & -s_{23} & c_{23} \end{pmatrix} \quad , \tag{1.7}$$

where $s_{ij} = \sin\theta_{ij}$ and $c_{ij} = \cos\theta_{ij}$, with $\theta_{ij} \in [0, \pi/2]$ and $\delta \in [0, 2\pi]$.

The most sensitive probes of the neutrino masses are oscillation experiments, but they are sensitive only to the squared-mass differences $m_i^2 - m_j^2$,not the absolute masses. We have only upper bounds on the absolute masses from cosmology ($\sum m_\nu \lesssim 0.5\,\mathrm{eV}$ [Abazajian 2011]) or from β-decay experiments ($m_{\nu_e} \leq 2.3\,\mathrm{eV}$ [Kraus 2005]) while the time-of-flight experiments are in conflict with relativity [Adamson 2007, Adam 2011]. For Majorana neutrinos the neutrinoless double β-decay experiments report a value comparable to cosmological limits ($m_{\nu_e} \equiv |\sum U_{ei}^2 m_{\nu_i}| \lesssim 0.3 - 0.7\,\mathrm{eV}$ [Andreotti 2011]).

The squared-mass difference between the second and first mass eigenstates[1]

$$\Delta m_{21}^2 = m_2^2 - m_1^2 > 0 \tag{1.8}$$

[1] $m_2 > m_1$ as seen from the solar neutrino experiments

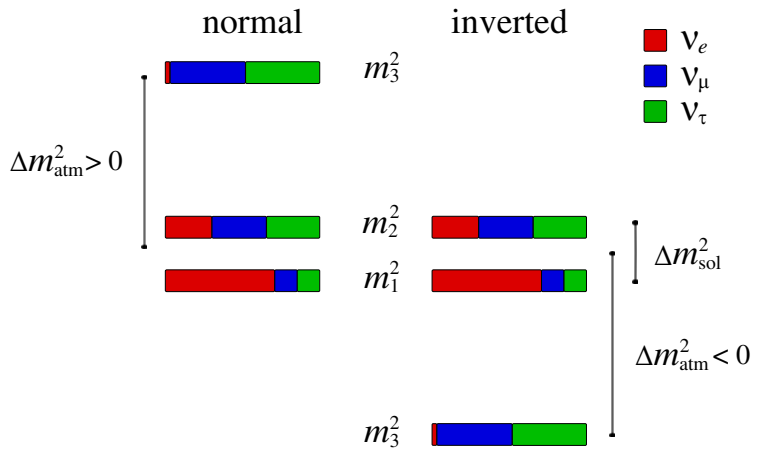

Figure 1.1: Neutrino mass eigenstates and the corresponding hierarchies. Flavor content is given in color coding.

is called the solar squared-mass difference, $\Delta m^2_{\odot}$. It is experimentally observed that it is much smaller than the other two $\Delta m^2_{21} \ll \Delta m^2_{31}, \Delta m^2_{32}$. The atmospheric mass difference is defined as

$$\Delta m^2_{\text{atm}} = m_3^2 - \frac{m_1^2 + m_2^2}{2} \quad . \tag{1.9}$$

It can be both positive and negative. In the first case we are dealing with the normal hierarchy and in the latter with the inverted (see Fig. 1.1).

Experiments have constrained five parameters governing neutrino mixing as summarized in Table 1.1. The sign of Δm^2_{13} and the value of the CP-violating phase δ are still unknown. Until very recently, only an upper bound on $\sin^2\theta_{13}$ existed, but in the last year global-fit analyses gave the first indications of non-zero θ_{13} [Fogli 2011, Schwetz 2011]. These analyses were further strengthened by the T2K long-baseline experiment's search for the appearance of electron neutrinos through $\nu_\mu \to \nu_e$ transitions [Abe 2011] and Double Chooz, a reactor neutrino experiment looking at a disappearance of $\bar{\nu}_e$'s produced in a nuclear reactor [De Kerret 2011]. These results open the possibility of measuring, in a not so distant future, the neutrino mass hierarchy and a possible CP violation in the leptonic sector [Nunokawa 2008].

As already mentioned, the original model of leptons did not contain mass terms for neutrinos, because there was no indication of their masses. Presently, we are confident of the existence of neutrino masses, but only for the interacting left chiral projection. We cannot tell whether the ν_R, needed to construct Dirac mass terms, actually exists. Moreover, as genuinely neutral particles,

Table 1.1: Results of the global 3ν oscillation analysis [Fogli 2011], in terms of best-fit values and allowed 1, 2 and 3σ ranges for the mass-mixing parameters.

$\Delta m^2_{\odot}/10^{-5}$ eV^2	$\sin^2\theta_{12}$	$\sin^2\theta_{13}$	$\sin^2\theta_{23}$	$\Delta m^2_{\rm atm}/10^{-3}$ eV^2
7.58	0.306	0.021	0.42	2.35
7.32 – 7.80	0.291 – 0.324	0.013 – 0.028	0.39 – 0.50	2.26 – 2.47
7.16 – 7.99	0.275 – 0.342	0.008 – 0.036	0.36 – 0.60	2.17 – 2.57
6.99 – 8.18	0.259 – 0.359	0.001 – 0.044	0.34 – 0.64	2.06 – 2.67

neutrinos are the only candidates to also have a Majorana nature, so the most general mass term one can introduce in the Lagrangian is

$$-\frac{1}{2}\left(\overline{\nu_L},\overline{\nu_L^C}\right)\begin{pmatrix} m_L & m_D \\ m_D & m_R\end{pmatrix}\begin{pmatrix}\nu_R^C \\ \nu_R\end{pmatrix}+\text{h.c.}\ , \tag{1.10}$$

where $m_{L(R)}$ stands for the left(right) handed Majorana mass and m_D is the Dirac mass. Charge-conjugate states $\nu^C_{L,R} \equiv (\nu^C)_{L,R} = (\nu_{R,L})^C$ have opposite chiralityand are not independent on the particle states. Majorana terms unavoidably violate lepton number, making neutrinoless double beta decay possible. In the early Universe, they introduce a mixing between left-handed and right-handed (and hence super-weakly interacting, sterile) neutrinos, so a system initially consisting of only left-handed, active components can also populate the sterile sector. In the effective description such processes are typically suppressed by a factor $(m/E)^2$ with m being a typical neutrino mass and E their energy. This manuscript considers only the relativistic neutrinos, neglecting the processes induced by Eq. 1.10. In this approximation the right-handed components ν_R and ν^C_L decouple from other species, and we are left with only two left-handed degrees of freedom ν_L and ν^C_R per flavor, which will be referred to as neutrinos and antineutrinos respectively.

Neutrinos will always be considered as propagating at the speed of light, yet with a dispersion relation

$$E^2 = \mathbf{p}^2 + M^2\ , \tag{1.11}$$

where $\mathbf{p}$ is the momentum of the neutrino and M its phenomenological mass, which in general depends on the Dirac and Majorana terms[2] of Eq. 1.10. In practice, we will neglect the mass term ($E = p$), except for the oscillations it induces.

[2]All possible effects of neutrinos masses and interactions on velocities will be neglected, including also the recent observation of superluminal neutrinos at the order of 10^{-5} [Adam 2011].

1.2.2 Vacuum oscillations in the one-particle formalism

Probably the most pedagogical and descriptive way of understanding the neutrinos oscillations is in the wave function formalism. To account for multiflavor nature of the neutrino state, it is represented by an N-dimensional vector in flavor space $|\psi\rangle$, N being the number of flavors. Such a state of the energy $\Omega^0 = \sqrt{p^2 + M^2}$ propagating in vacuum obeys the Schrödiger equation

$$\mathrm{i}\partial_t|\psi\rangle = \Omega^0|\psi\rangle \sim \left(p + \frac{M^2}{2p}\right)|\psi\rangle \ . \tag{1.12}$$

The mass eigenstate basis is defined as the one in which the mass matrix M is diagonal, so in the flavor basis it is rotated by the PMNS mixing matrix:

$$M = U\, M_{\mathrm{diag}}\, U^\dagger \ . \tag{1.13}$$

In general one is interested in calculating probability of transition from one state to another

$$P_{\nu_\alpha\to\nu_\beta} = \left|\langle\nu_\beta|e^{-\mathrm{i}\,\Omega^0\,t}|\nu_\alpha\rangle\right|^2 \ . \tag{1.14}$$

All the terms in Ω^0 proportional to the unity matrix vanish under the modulus and only the traceless part of it carries information about flavor conversions. It is therefore customary to reduce the mass matrix to its traceless contribution.

For most practical purposes, it is possible to consider only two flavors ν_e and ν_x with a vacuum mixing angle θ_0:

$$\begin{aligned} \nu_e &= \cos\theta_0\,\nu_1 + \sin\theta_0\,\nu_2 \\ \nu_x &= -\sin\theta_0\,\nu_1 + \cos\theta_0\,\nu_2 \ . \end{aligned} \tag{1.15}$$

The mass matrix then reduces to

$$\begin{aligned} M^2 \quad &= \quad \begin{pmatrix} c_{\theta_0} & s_{\theta_0} \\ -s_{\theta_0} & c_{\theta_0} \end{pmatrix} \begin{pmatrix} m_1^2 & 0 \\ 0 & m_2^2 \end{pmatrix} \begin{pmatrix} c_{\theta_0} & -s_{\theta_0} \\ s_{\theta_0} & c_{\theta_0} \end{pmatrix} \\ &\xrightarrow{-\mathrm{Tr}} \quad \begin{pmatrix} c_{\theta_0} & s_{\theta_0} \\ -s_{\theta_0} & c_{\theta_0} \end{pmatrix} \begin{pmatrix} -\frac{\Delta m^2}{2} & 0 \\ 0 & +\frac{\Delta m^2}{2} \end{pmatrix} \begin{pmatrix} c_{\theta_0} & -s_{\theta_0} \\ s_{\theta_0} & c_{\theta_0} \end{pmatrix} \ . \end{aligned} \tag{1.16}$$

The probability for the transition $\nu_e \to \nu_x$ now is given by the usual oscillation formula

$$\begin{aligned} P_{\nu_e\to\nu_x} &= \left| (0 \quad 1) \begin{pmatrix} c_{\theta_0} & s_{\theta_0} \\ -s_{\theta_0} & c_{\theta_0} \end{pmatrix} \begin{pmatrix} e^{\mathrm{i}\,\frac{\Delta m^2}{4p}\,t} & 0 \\ 0 & e^{-\mathrm{i}\,\frac{\Delta m^2}{4p}\,t} \end{pmatrix} \begin{pmatrix} c_{\theta_0} & -s_{\theta_0} \\ s_{\theta_0} & c_{\theta_0} \end{pmatrix} \begin{pmatrix} 1 \\ 0 \end{pmatrix} \right|^2 \\ P_{\nu_e\to\nu_x} &= \sin^2 2\theta_0\, \sin^2 \frac{\Delta m^2}{4p}\, t \end{aligned} \tag{1.17}$$

1.2.3 Matrices of occupation numbers

The most straightforward generalization of the one-particle formalism to multi-particle one is through a definition of the density matrix $\overset{(-)}{\varrho} = |\psi\rangle\langle\psi|$ for (anti)neutrino state $|\psi\rangle$. The equation of motion follows directly from 1.12

$$\mathrm{i}\partial_t \overset{(-)}{\varrho} = \pm\left[\Omega^0, \overset{(-)}{\varrho}\right] = \pm\left[\frac{\mathsf{M}^2}{2p}, \overset{(-)}{\varrho}\right] \ , \tag{1.18}$$

where M^2 is the traceless part of the mass matrix and the upper (lower) sign refers to (anti)neutrinos. In the two flavor case the squared-mass matrix follows from Eq.1.16

$$\mathsf{M} = \frac{\Delta m^2}{2}\begin{pmatrix} -\cos 2\theta_0 & \sin 2\theta_0 \\ \sin 2\theta_0 & \cos 2\theta_0 \end{pmatrix} \ . \tag{1.19}$$

For a complete treatment of the neutrino ensemble in contact with a thermal bath, it is natural to generalize the density matrix to a matrix of occupation numbers [Dolgov 1981, Stodolsky 1987, Raffelt 1993, Sigl 1993]. In this formalism, an ensemble consisting of two flavors of neutrinos is described by a hermitian matrix

$$\varrho_{\mathbf{p}} = \begin{pmatrix} n_{\nu_e}(\mathbf{p}) & n_{\nu_e\nu_x}(\mathbf{p}) \\ n_{\nu_x\nu_e}(\mathbf{p}) & n_{\nu_x}(\mathbf{p}) \end{pmatrix} \ , \tag{1.20}$$

whose diagonal entries represent the usual occupation numbers at momentum $\mathbf{p}$ for the corresponding flavor $n_{\nu_e} = \int \frac{\mathrm{d}^3\mathbf{p}}{(2\pi)^3}\, n_{\nu_e}(\mathbf{p})$, while the off-diagonal elements $n_{\nu_x\nu_e} = n^*_{\nu_e\nu_x}$ describe the mixing between the flavors and encode the information related to coherence of the system. In vacuum ϱ matrices also obey the Eq. 1.18. For antineutrinos analogous matrices are defined.

In the 2×2 case it is sometimes convenient to expand all the matrices in terms of the Pauli matrices. For this purpose we introduce the polarization vector $\mathbf{P}$

$$\varrho = \frac{n_{\nu_e} + n_{\nu_x}}{2} + \frac{n_{\nu_e} - n_{\nu_x}}{2}\, \mathbf{P}\cdot\sigma \ , \tag{1.21}$$

and similarly $\overline{\mathbf{P}}$ for antineutrinos. The normalization of the second term is arbitrary and changes depending on the context and author. Here it is chosen so that a pure system of $\nu_{e(x)}$ corresponds to $\mathbf{P} = (0, 0, \pm 1)$, while for an equal mixture of both species $P_z = 0$.

It is common to write the equations of motion as the precession equation for the polarization vectors

$$\dot{\mathbf{P}} = \omega\, \mathbf{B}\times\mathbf{P} \ , \qquad \dot{\overline{\mathbf{P}}} = -\omega\, \mathbf{B}\times\mathbf{P} \ , \tag{1.22}$$

with ω the frequency of oscillation

$$\omega = \frac{\Delta m^2}{2p} \tag{1.23}$$

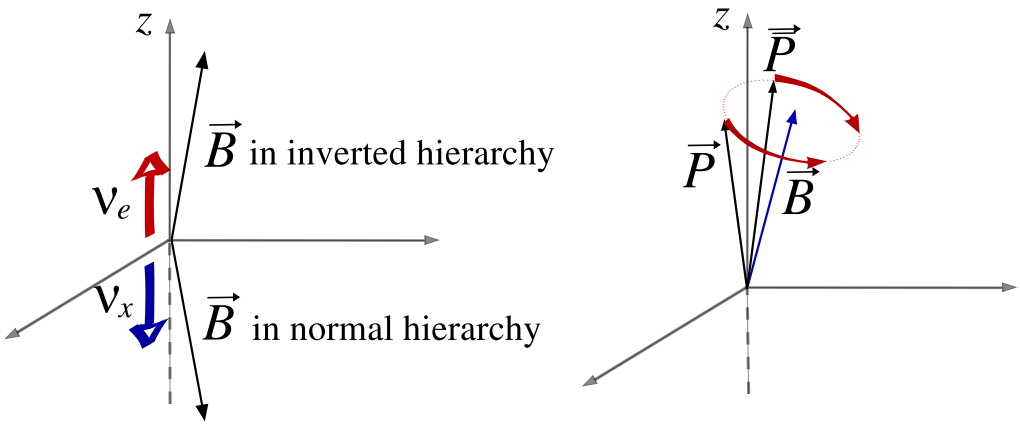

Figure 1.2: *Left Panel:* Mass direction vector **B** in different hierarchies. A small angle (2θ) between **B** and the z axis corresponds then to inverted and the large angle ($\pi - 2\theta$) to normal mass hierarchy. *Right Panel:* Polarization vectors for particles **P** and antiparticles $\overline{\mathbf{P}}$ precessing around **B**.

and a unit vector **B**

$$\mathbf{B} = (\sin 2\theta_0, 0, -\cos 2\theta_0)^T \ . \tag{1.24}$$

The form of the precession Eqs. 1.22 makes it clear that the vacuum conversions do not change the overall content of the system — the length of the polarization vector **P** remains unchanged.

Visual interpretation of the vacuum evolution is given in Fig. 1.2.3*a*. The vector **B**, of unit length, plays the role of the magnetic field around which the two polarization vectors **P** and $\overline{\mathbf{P}}$ precess in opposite directions with an energy-dependent frequency ω. For a small mixing angle, in the normal hierarchy, **B** is almost anticollinear to the z axis. Inverted hierarchy corresponds to $\omega \to -\omega$, but since ω always shows up multiplied by **B**, it is sometimes convenient to keep the frequency $\omega > 0$ and to sweep the hierarchy transformation in the definition of **B**, so that in the inverted hierarchy **B** is almost collinear with the z axis (see Fig. 1.2.3*b*).

1.3 Matter potential

Neutrino interactions with matter, although very weak, will influence their propagation. For normal matter (electrons, neutrons and protons), only the charged current will affect flavor content, because the neutral current interactions are flavor blind and contribute equally in all flavors. The Hamiltonian

describing charged current interactions between electron neutrinos and electrons is

$$H_{CC} = \frac{2G_{\rm F}}{\sqrt{2}} \left[\bar{\nu}_{e\,L}\, \gamma^{\alpha}\, \nu_{e\,L} \right] \left[\bar{e}\, \gamma_{\alpha}\, (1-\gamma^5)\, e \right] \ . \tag{1.25}$$

The average of the Hamiltonian over the electron background in the rest frame of the medium is given by

$$H_{CC} = \frac{2G_{\rm F}}{\sqrt{2}} \left[\bar{\nu}_{e\,L}\, \gamma^{\alpha}\, \nu_{e\,L} \right] \int \frac{{\rm d}^3\mathbf{p}}{2E(2\pi)^3}\, f_e(\mathbf{p},T) \\ \frac{1}{2} \sum_{h=\pm 1} \langle e(p,h)|\, \bar{e}\, \gamma_{\alpha}\, (1-\gamma^5)\, e\, |e(p,h)\rangle \ . \tag{1.26}$$

We consider only forward scattering, with no momentum or helicity exchange between electron and neutrino, so the initial and final states are the same. The sum over helicities as usual reduces to a trace

$$\frac{1}{2} \sum_{h=\pm 1} \langle e(p,h)|\, \bar{e}\, \gamma_{\alpha}\, (1-\gamma^5)\, e\, |e(p,h)\rangle \tag{1.27}$$

$$= \frac{1}{2}\, {\rm Tr} \left[\left(\sum_{h=\pm 1} u(p,h) \overline{u}(p,h) \right) \gamma_{\alpha}\, (1-\gamma^5) \right] \tag{1.28}$$

$$= \frac{1}{2}\, {\rm Tr} \left[(\not{p} + m)\ \gamma_{\alpha}\, (1-\gamma^5) \right] = 2\, p_{\alpha} \ . \tag{1.29}$$

The Hamiltonian becomes

$$H_{CC} = \sqrt{2} G_{\rm F}\, \bar{\nu}_{e\,L} \left(\int \frac{{\rm d}^3\mathbf{p}}{2E(2\pi)^3}\, f_e(\mathbf{p},T)\, 2\not{p} \right) \nu_{e\,L} \tag{1.30}$$

$$= \sqrt{2} G_{\rm F}\, \bar{\nu}_{e\,L} \left(\int \frac{{\rm d}^3\mathbf{p}}{(2\pi)^3}\, f_e(\mathbf{p},T)\, \frac{1}{E} (E\gamma^0 - \mathbf{p}\boldsymbol{\gamma}) \right) \nu_{e\,L} \ . \tag{1.31}$$

We are usually dealing with a background of homogeneous and isotropic electrons, so $f_e(\mathbf{p},T) = f_e(p,T)$ and the integral over momenta can be performed

$$\int \frac{{\rm d}^3\mathbf{p}}{(2\pi)^3}\, f_e(\mathbf{p},T)\, \frac{1}{E} (E\gamma^0 - \mathbf{p}\boldsymbol{\gamma}) = \gamma^0 \int \frac{{\rm d}^3\mathbf{p}}{(2\pi)^3}\, f_e(\mathbf{p},T) = n_e \gamma^0 \ , \tag{1.32}$$

where n_e is the electron number density. The integral over $\mathbf{p}$ vanishes due to its symmetry. The same procedure for positrons yields and opposite sign in the result, so the effective Hamiltonian from a background of electrons and positrons is simply

$$H_{CC} = G_{\rm F} \sqrt{2}\, (n_e - n_{\bar{e}})\ \bar{\nu}_e \gamma^0 \nu_e \ . \tag{1.33}$$

Therefore, while traveling through a see of electrons, electron neutrinos experience a positive energy shift proportional to the density of electrons,

$$\lambda = G_{\mathrm{F}}\sqrt{2}\,(n_e - n_{\bar{e}}) \ , \tag{1.34}$$

due to repulsive interaction with the background. In the language of flavor matrices, this potential is represented by a diagonal contribution to Hamiltonian $\mathrm{diag}(\lambda, 0, 0)$, whose trace-free part in the 2×2 case reads $\mathsf{H}_{CC} = \frac{\lambda}{2}\,\mathrm{diag}(+1, -1)$. Together with the vacuum contribution, the Hamiltonian now reads

$$\mathsf{H} = \frac{1}{4E}\begin{pmatrix} -\Delta m^2\cos 2\theta_0 + 2E\lambda & \Delta m^2 \sin 2\theta_0 \\ \Delta m^2 \sin 2\theta_0 & \Delta m^2 \cos 2\theta_0 - 2E\lambda \end{pmatrix} \ . \tag{1.35}$$

1.3.1 Finite gauge boson mass corrections to the matter potential

The potential shift of Eq. 1.34 has been calculated from the effective four fermion interaction governed only by the Fermi constant G_{F}. However, in some environments such as the early Universe, the finite masses of gauge bosons might be relevant. Table 1.2 shows neutrino potentials from electroweak interactions with background electrons, protons and neutrons calculated at tree level [Notzold 1988]. Note how the same first-order contributions to electron and μ (τ) neutrino potential in the background of electrons cancel out. Corrections of the order $G_{\mathrm{F}}/M_{\mathrm{w}}^2$ are due to gauge-boson propagator expansion

$$\frac{-1}{k^2 - M_{\mathrm{w}}^2} \simeq \frac{1}{M_{\mathrm{w}}^2} + \frac{k^2}{M_{\mathrm{w}}^4} = \frac{1}{M_{\mathrm{w}}^2} - \frac{2E_\nu m_e}{M_{\mathrm{w}}^4} \tag{1.36}$$

and can be relevant in a CP-symmetric plasma such as in the early Universe, where the electron asymmetry is of the order of the baryon one, fixed by WMAP to $\sim 10^{-10}$.

Although not directly, a neutrino can also interact with a background photon by exchanging an electron. However, such a potential is $\mathcal{O}(\alpha)$ times smaller than the $G_{\mathrm{F}}/M_{\mathrm{w}}^2$ contribution, which itself is already a correction, so the neutrino–photon interactions are irrelevant in the early Universe.

1.3.2 MSW effect

The diagonalization of Hamiltonian 1.35 makes it natural to define the effective mass splitting Δm_m^2 in the medium and the mixing angle θ_m in the medium such that

$$U_m \mathsf{H}\, U^{m\dagger} \equiv \frac{\Delta m_m^2}{4E}\begin{pmatrix} -\cos 2\theta_m & \sin 2\theta_m \\ \sin 2\theta_m & \cos 2\theta_m \end{pmatrix} \ , \tag{1.37}$$

Table 1.2: Potentials for neutrinos propagating through an isotropic non-relativistic background. The upper sign is for neutrinos, the lower for antineutrinos. n_f is the number density of fermions in the background medium.

ν flavor	Background	Potential shift
ν_e	e	$\pm\frac{G_\mathrm{F}}{\sqrt{2}}(4\sin^2\theta_\mathrm{w}+1)(n_e-n_{\bar{e}})-\frac{8\sqrt{2}G_\mathrm{F}}{3M_\mathrm{w}^2}E_\nu(\rho_e+\rho_{\bar{e}})$
ν_μ,ν_τ	e	$\pm\frac{G_\mathrm{F}}{\sqrt{2}}(4\sin^2\theta_\mathrm{w}-1)(n_e-n_{\bar{e}})$
ν_e,ν_μ,ν_τ	n	$\mp\frac{G_\mathrm{F}}{\sqrt{2}}(n_n-n_{\bar{n}})$
ν_e,ν_μ,ν_τ	p	$\mp\frac{G_\mathrm{F}}{\sqrt{2}}(4\sin^2\theta_\mathrm{w}-1)(n_p-n_{\bar{p}})$

with U_m transforming the flavor eigenstates and mass eigenstates in the medium

$$\begin{aligned}\nu_e &= \cos\theta_m\,\nu_1^m+\sin\theta_m\,\nu_2^m\\ \nu_x &= -\sin\theta_m\,\nu_1^m+\cos\theta_m\,\nu_2^m\ .\end{aligned}\tag{1.38}$$

These two parameters are functions of vacuum values $(\Delta m^2,\theta_0)$ and neutrino energy:

$$\Delta m_m^2=\Delta m^2\frac{\sin 2\theta_0}{\sin 2\theta_m}\tag{1.39}$$

and

$$\sin^2 2\theta_m=\frac{\sin^2 2\theta_0}{\sin^2 2\theta_0+(\cos 2\theta_0-\frac{2E\lambda}{\Delta m^2})^2}\ .\tag{1.40}$$

The oscillation probability $P(\nu_e\to\nu_e)$ in matter has the same form as Eq. 1.17, with $\theta_0\to\theta_m$ and $\Delta m^2\to\Delta m_m^2$.

From Eq. 1.40 we observe a resonant dependence of the mixing angle $\theta(\lambda)$ with a maximum at

$$\cos 2\theta_0=\frac{2E\lambda}{\Delta m^2}\ ,\tag{1.41}$$

leading to the famous Mikheyev-Smirnov-Wolfenstein (MSW) effect [Wolfenstein 1978, Mikheev 1986]. The MSW resonant conversions happen for neutrinos in the normal mass hierarchy and for antineutrinos in the inverted one (for antineutrinos one must change $\lambda\to-\lambda$).

1.3.3 Matter potential as a vector

In the language of polarization vectors, the matter potential appears as a constant vector pointing along the z axis (i.e. toward the electron flavor)

$$\mathbf{V} = (0, 0, \lambda)^T \ , \tag{1.42}$$

so that the equations of motion for the polarization vectors are

$$\dot{\mathbf{P}} = (\omega\,\mathbf{B} + \mathbf{V}) \times \mathbf{P} \ , \qquad \dot{\overline{\mathbf{P}}} = (-\omega\,\mathbf{B} + \mathbf{V}) \times \mathbf{P} \ . \tag{1.43}$$

The polarization vectors now precess around $\mathbf{V}$ *and* $\mathbf{B}$. The system behaves as in vacuum but with a smaller mixing angle — $\mathbf{P}$'s precess around a vector closer to the z axis, the effect known as the matter suppression.

1.4 Coherence vs. decoherence

When we consider realistic ensembles in which neutrinos in general have continuous energy distributions, we define a frequency-dependent (and through Eq. 1.23 also energy-dependent) polarization vector $\mathbf{P}_\omega$, properly normalized so that total $\mathbf{P} = \int \mathrm{d}\omega \mathbf{P}_\omega$ has the same physical meaning as before. Consider a system starting in pure weak-interaction eigenstate with all $\mathbf{P}_\omega$'s collinear with the z axis and without the ordinary matter term. As each mode precesses with different frequency, eventually all of them will fan out in cone centered on $\mathbf{B}$ with the total $\mathbf{P}$ collinear to it. We call this a kinematical decoherence.

Ordinary matter can postpone the decoherence. A large matter term ($|\mathbf{V}| \gg \omega$) in the previous picture, typically not energy dependent, makes all modes precess quickly around it. Since this precession is the same for all (particle and antiparticle) modes, we can change perspective and go to a frame corotating around z in which the matter term does not exist. In this frame $\mathbf{B}$ rotates fast around the z axis with frequency λ, so the transverse part of $\mathbf{B}$ averages to zero — only the z component of $\mathbf{B}$ survives. If we start from a pure state with all the polarization vectors along the z axis, the system remains stuck in its initial state. This preserves the original coherence for a longer time. Neutrino self-interaction is even more effective in keeping the coherence and can stack all modes together, making them oscillate with common frequency.

1.5 Neutrino self-interaction

In extreme environments, such as supernovae and the early Universe, the density of neutrinos can be so high that the they themselves create a refractive

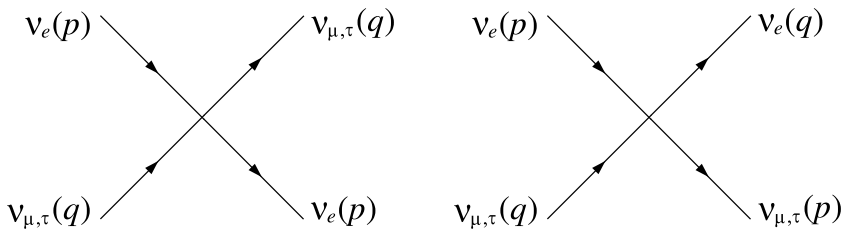

Figure 1.3: Feynman diagrams for neutrino self-interactions.

index to their own propagation [Notzold 1988, **?**]. These self-interactions arise from considering the Feynman diagrams shown in Figure 1.5. Following the same reasoning as for the background of charged leptons, we can derive the potential for ν_e's

$$V_{\nu_e\nu_e} = 2\,G_{\rm F}\sqrt{2}\,(n_{\nu_e} - n_{\bar\nu_e}) + G_{\rm F}\sqrt{2}\,(n_{\nu_x} - n_{\bar\nu_x}) \ , \tag{1.44}$$

where the factor of 2 for the background of the same flavor originates from the fact that there is no distinction between initial and final states and ν_e's can in fact exchange momenta. The potential for the other flavor is the same with $\nu_e \leftrightarrow \nu_x$.

However, proper treatment of the system must also include the zero-momentum-transfer processes in which neutrinos exchange flavors, corresponding to the right panel of Fig. 1.5 for $\nu_\alpha \neq \nu_\beta$. These processes correspond to a Hamiltonian

$$H_{\nu_e\nu_x} = \frac{G_{\rm F}}{\sqrt{2}}\,[\,\bar\nu_{x\,L}(\mathbf{p})\,\gamma^\alpha\,(1-\gamma^5)\,\nu_{e\,L}(\mathbf{p})\,]\,[\,\bar\nu_e(\mathbf{q})\,\gamma_\alpha\,(1-\gamma^5)\,\nu_x(\mathbf{q})\,]\ , \tag{1.45}$$

which introduces an additional off-diagonal potential

$$V_{\nu_e\nu_x} = \frac{G_{\rm F}}{\sqrt{2}}\,(n_{\nu_e\nu_x} - n_{\bar\nu_e\bar\nu_x}) \ , \tag{1.46}$$

where n_{ex} and $\bar n_{ex}$ are the off-diagonal elements of the ϱ matrices introduced in Eq. 1.20. Since the contributions proportional to the identity matrix do not change the physics, we can subtract the common terms $G_{\rm F}\sqrt{2}\,(n_{\nu_e} - n_{\bar\nu_e}) + G_{\rm F}\sqrt{2}\,(n_{\nu_x} - n_{\bar\nu_x})$ from the diagonal elements of the potential, leaving us with the effective Hamiltonian of the neutrino–neutrino interaction

$$H_{\nu\nu} = \sqrt{2}G_{\rm F}(\varrho - \bar\varrho) \ . \tag{1.47}$$

While this form holds for homogeneous and isotropic systems, in order to develop a general formalism, we should make the integration over momenta explicit

$$H_{\nu\nu} = \sqrt{2}G_{\rm F}\int \frac{{\rm d}\mathbf{p}}{(2\pi)^3}(\varrho_{\mathbf{p}} - \bar\varrho_{\mathbf{p}})(1-\cos^2\beta) \ , \tag{1.48}$$

where β is the angle between the two neutrinos originating from the angular dependence of the scattering amplitude. This feature will prove very important for the treatment of neutrinos streaming from a supernova (see Ch. 4). Here I will comment on the isotropic case.

The equations of motion for polarization vectors in the presence of the neutrino self-interaction (with collisions neglected) are now

$$\begin{aligned} \dot{\mathbf{P}}_\omega &= (+\omega\mathbf{B} + \mathbf{V} + \mu(\mathbf{P} - \overline{\mathbf{P}})) \times \mathbf{P}_\omega \ , \\ \dot{\overline{\mathbf{P}}}_\omega &= (-\omega\mathbf{B} + \mathbf{V} + \mu(\mathbf{P} - \overline{\mathbf{P}})) \times \overline{\mathbf{P}}_\omega \ , \end{aligned} \tag{1.49}$$

where the strength of self-interaction μ depends on the normalization of the polarization vectors and in general is proportional to neutrino densities. If they are normalized according to Eq. 1.21 $\mu = \sqrt{2}\, G_{\rm F}(n_{\nu_e} - n_{\nu_x})$.

1.5.1 Synchronized neutrino oscillations in the early Universe

Inclusion of neutrino self-interactions in the equations of motion makes the system inherently non-linear. One must know the neutrino background to determine how an individual neutrino oscillates, but one must know the flavor of every individual neutrino to determine the background. First investigations [Samuel 1993] by brute-force numerical computation led to a discovery of synchronized oscillations: instead of a quick mode dephasing due to different frequencies, when the ν–ν potential is comparable to or higher than a typical vacuum frequency, the modes get locked to each other, forming one common vector that oscillates with a common frequency $\omega_{\rm synch}$ corresponding to an average vacuum frequency.

The first analytical investigations of this counter-intuitive effect appeared 10 years after it was first discovered in numerical simulations [Pastor 2002]. Suppose there exists only a self-interaction term. The equations of motion for both neutrinos and antineutrinos are then

$$\dot{\mathbf{P}}_\omega = \mu\mathbf{J} \times \mathbf{P}_\omega \ , \tag{1.50}$$

where $\mathbf{J}$ is the total polarization vector $\mathbf{J} = \int {\rm d}\omega \mathbf{P}_\omega$. Of course, if all neutrinos are initially prepared in a specific flavor state, all $\mathbf{P}_\omega$'s, and therefor $\mathbf{J}$, lie in the z axis, and no precession takes place. The evolution is also trivial if the system is in a perfect incoherent state with all vectors pointing in different directions so that $\mathbf{J} = 0$.

Consider, however, a system in which the $\mathbf{P}_\omega$'s point in different directions, but do not sum to zero. All of them precess around a common direction $\mathbf{J}$ with a common frequency μ. We now switch on the vacuum term and suppose

it is much weaker than the self-interaction term ($\langle\omega\rangle \ll \mu$). A typical $\mathbf{P}_\omega$ then precesses around $\mathbf{J}$ much faster than around $\mathbf{B}$, so that its projection on total vector $\mathbf{P}_\omega|_\mathbf{J} = \hat{\mathbf{J}}(\hat{\mathbf{J}} \cdot \mathbf{P}_\omega)$ is the only component external $\mathbf{B}$ field sees, since its transverse part averages to zero. Slow movement of $\mathbf{J}$ around $\mathbf{B}$ is therefore followed by every individual $\mathbf{P}_\omega$, so they all precess around $\mathbf{B}$ with a common frequency ω_{synch}

$$\dot{\mathbf{J}} = \omega_{\text{synch}}\, \mathbf{B} \times \mathbf{J} \ . \tag{1.51}$$

It is straightforward now to get the synchronization frequency. From the definition of $\mathbf{J}$ it follows that

$$\begin{aligned} \dot{\mathbf{J}} &= \int \mathrm{d}\omega\, \dot{\mathbf{P}}_\omega = \int \mathrm{d}\omega\, \dot{\mathbf{P}}_\omega|_\mathbf{J} \\ &= \int \mathrm{d}\omega\, \omega\, \mathbf{B} \times \mathbf{P}_\omega|_\mathbf{J} \\ &= \mathbf{B} \times \hat{\mathbf{J}} \int \mathrm{d}\omega\, \omega\, \mathbf{P}_\omega \cdot \hat{\mathbf{J}} \ . \end{aligned} \tag{1.52}$$

With Eq. 1.51 this yields

$$\omega_{\text{synch}} = \frac{1}{|\mathbf{J}|} \int \mathrm{d}\omega\, \omega\, \mathbf{P}_\omega \cdot \hat{\mathbf{J}} \ . \tag{1.53}$$

In particular, if the system was initially in a coherent state, i.e. all modes had started aligned,

$$\omega_{\text{synch}} \equiv \langle\omega\rangle = \frac{\int \mathrm{d}\omega\omega|\mathbf{P}_\omega|}{\int \mathrm{d}\omega|\mathbf{P}_\omega|} \ . \tag{1.54}$$

1.5.2 Bipolar oscillations

The above picture for neutrinos is easily generalized to include antineutrinos as well. The system behaves the same way, except that the role of total angular momentum is now played by $\mathbf{I} = \mathbf{J} - \bar{\mathbf{J}}$. Antiparticles appear on the same footing as particles, but they rotate in the opposite sense. Vector $\mathbf{I}$ is the one that precesses slowly around $\mathbf{B}$

$$\mathbf{I} = \omega_{\text{synch}}\mathbf{B} \times \mathbf{I} \ , \tag{1.55}$$

while all the individual $\mathbf{P}_\omega$ and $\overline{\mathbf{P}}_\omega$ are stuck to it. The synchronization frequency is now

$$\omega_{\text{synch}} = \frac{1}{|\mathbf{I}|} \left(\int \mathrm{d}\omega\omega \hat{\mathbf{I}} \cdot \mathbf{P}_\omega + \int \mathrm{d}\omega\omega \hat{\mathbf{I}} \cdot \overline{\mathbf{P}}_\omega \right) \ . \tag{1.56}$$

Starting from a coherent state of perfect chemical equilibrium (vanishing $\mathbf{I}$), the evolution is trivial. Although it might seem irrelevant, the inclusion of antineutrinos leads to a qualitatively new phenomenon — bipolar

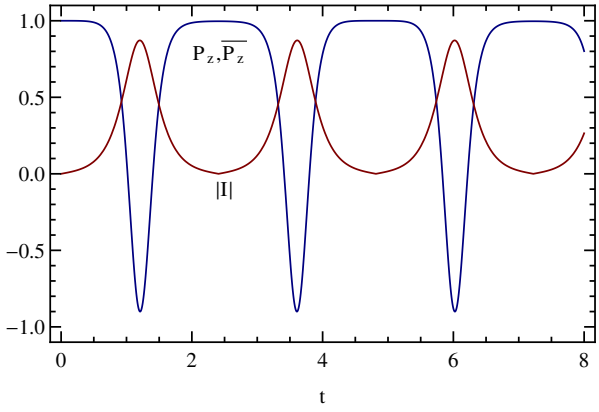

Figure 1.4: The behavior of P_z and $\overline{P}_z$ for a schematic system with only one frequency $\omega = 1$, in inverted mass hierarchy with a mixing angle $\theta_0 = 0.02$ and strong neutrino self-interaction $\mu = 10$.

oscillations. Suppose we are dealing with an ensemble very close to but not at a vanishing chemical equilibrium. In this case $\mathbf{I}$ is very small, corresponding to large ω_{synch}. If the mixing is large ($\mathbf{B}$ tilted substantially away from the z axis), the effect of self-interactions is to increase the precession frequency of individual polarization vectors to ω_{synch}.

If the mixing is small, the evolution strongly depends on the mass hierarchy. The situation closely resembles a pendulum in flavor space in a homogeneous force field $\omega\mathbf{B}$ [Hannestad 2006]. In this picture the inverse of ν-ν interaction strength μ^{-1} has the role of the moment of inertia while $\mathbf{I}$ acts as the pendulum orbital angular momentum. Since the force field $\omega\mathbf{B}$ determines the preferred direction, switching between mass hierarchies can be understood only as switching the angle of $\mathbf{B}$ with respect to the z axis (as shown in Fig. 1.2.3). In the case of normal hierarchy, $\mathbf{B}$ points to a direction opposite to $\mathbf{P}$ and $\overline{\mathbf{P}}$, so the system is in the minimum of potential energy. The role of self-interaction then increases the oscillation frequency beyond the typical vacuum values.

For the inverted mass hierarchy, the preferred direction $\mathbf{B}$ is almost aligned with the z axis, i.e. almost collinear to $\mathbf{P}$ and $\overline{\mathbf{P}}$. A small seed of $|\mathbf{I}|$ is enough to drive $\mathbf{P}$ and $\overline{\mathbf{P}}$ in the opposite directions away from their initial orientations until the state of almost complete flavor conversions. The inertia the system has acquired then drives it back to a situation close to the initial one and the evolution repeats (see Fig. 1.4). We call this behavior bipolar oscillations. It is important to stress that the these flavor conversions are of a different nature than the MSW effect.

This effect is known to be able to suppress flavor evolution. In the early Universe, a "pathological" case may exist with two species of neutrinos having opposite chemical potentials (see Sec. 3.1) $\mathbf{P} = -\overline{\mathbf{P}}$, so the resulting total angular momentum is large $\mathbf{I} = \mathbf{P} - \overline{\mathbf{P}} = 2\mathbf{P}$. On the other hand, $\omega_{\rm synch} = 0$, so the initial conditions remain frozen until neutrinos dilute enough so that the self-interaction does not dominate the evolution.

The suppression of the evolution is also observed in the context of supernovae (see Sec. 4.3.1). The usual flux hierarchy $F_{\nu_e} > F_{\bar{\nu}_e} > F_{\nu_x}$ ensures that the two polarization vectors initially have different lengths $\mathbf{P} - \overline{\mathbf{P}} = \epsilon$. In fact, if the asymmetry ϵ is big enough, the self-interaction dominates the evolution.

1.6 Collision term

So far we have treated the evolution of the neutrino ensembles in the absence of collisions. Whenever mentioned, the decoherence was purely kinematical, with the origin in dephasing of different polarization vectors due to their different frequencies. Collisions fundamentally change this picture introducing momentum exchanging processes.

The collision term $C[\varrho_{\mathbf{p}}]$ must account for creation and annihilation processes and all the momentum exchanging processes of neutrinos with the background and among neutrinos themselves. The general expression accounting exactly for all the effects is rather complicated and lengthy [Sigl 1993]. The useful approximations for the applicable in the early Universe are given in [Bell 1999, McKellar 1994].

1.6.1 Collisional integral

The diagonal entries of the collision term are the Boltzmann collisional integrals in the usual sense. Suppose for a moment that there is no neutrino oscillations. The distribution function for each species n_{ν_α} would then evolve independently and the collisional term would have just the collisional integrals on the diagonal. The element for one representative species f_ν has the form

$$\mathcal{C}[f_\nu] = \sum \frac{1}{2(2\pi)^5} \int \mathrm{d}\Omega \; \Lambda(f_1, f_2, f_3, f_4) M^2 \delta^4(\bar{p}_1 + \bar{p}_2 - \bar{p}_3 - \bar{p}_4), \qquad (1.57)$$

where $p_1 \equiv q$, $f_1 \equiv f_\nu$ and $\mathrm{d}\Omega$ is the phase space element of the integration over all the momenta except $\mathbf{q}$

$$\mathrm{d}\Omega = \frac{\mathrm{d}^3\mathbf{p}_2}{2E_2} \frac{\mathrm{d}^3\mathbf{p}_3}{2E_3} \frac{\mathrm{d}^3\mathbf{p}_4}{2E_4} \quad . \qquad (1.58)$$

Table 1.3: Neutrino reactions relevant in the early Universe and the corresponding square matrix elements.

Reaction	M^2
$\nu_i + \bar{\nu}_i \to e^- + e^+$	$32G_{\rm F}^2\left[(C_V + C_A)^2 Q_3 + (C_V - C_A)^2 Q_2 + (C_V^2 - C_A^2)Q_4\right]$
$\nu_i + e^- \to \nu_i + e^-$	$32G_{\rm F}^2\left[(C_V + C_A)^2 Q_1 + (C_V - C_A)^2 Q_3 - (C_V^2 - C_A^2)Q_5\right]$
$\nu_i + e^+ \to \nu_i + e^+$	$32G_{\rm F}^2\left[(C_V + C_A)^2 Q_3 + (C_V - C_A)^2 Q_1 - (C_V^2 - C_A^2)Q_5\right]$
$\nu_i + \bar{\nu}_i \to \nu_i + \bar{\nu}_i$	$128G_{\rm F}^2 Q_3$
$\nu_i + \bar{\nu}_i \to \nu_j + \bar{\nu}_j$	$32G_{\rm F}^2 Q_3$
$\nu_i + \bar{\nu}_j \to \nu_i + \bar{\nu}_j$	$32G_{\rm F}^2 Q_3$
$\nu_i + \nu_k \to \nu_i + \nu_k$	$32G_{\rm F}^2 Q_1$

Pauli blocking factors are included in through

$$\Lambda(f_1, f_2, f_3, f_4) \equiv f_4 f_3 (1 - f_2)(1 - f_1) - f_1 f_2 (1 - f_3)(1 - f_4), \tag{1.59}$$

and M^2 is the matrix element squared and summed over initial and final spin states; $\bar{p}_i$ are four-momenta of the incoming (1,2) and outgoing (3,4) particles, and the sum is taken over all reactions involving f_1. In the ealy Universe, it is enough to consider the reactions presented in Table 1.3, along with the respective matrix elements [Hannestad 1995]. Indecies i, j, k run over electron, muon, and tau neutrino, with the exception that $j \neq i$.

Quantities Q_i are defined as follows:

$$\begin{aligned} Q_1 &= (\bar{p}_1 \cdot \bar{p}_2)(\bar{p}_3 \cdot \bar{p}_4), \\ Q_2 &= (\bar{p}_1 \cdot \bar{p}_3)(\bar{p}_2 \cdot \bar{p}_4), \\ Q_3 &= (\bar{p}_1 \cdot \bar{p}_4)(\bar{p}_2 \cdot \bar{p}_3), \\ Q_4 &= m^2(\bar{p}_1 \cdot \bar{p}_2), \\ Q_5 &= m^2(\bar{p}_1 \cdot \bar{p}_3), \end{aligned} \tag{1.60}$$

where m is the electron mass. It has been shown [Hannestad 1995] that the integrals over $\mathrm{d}^3\mathbf{p}_4$ and over angles in $\mathrm{d}^3\mathbf{p}_2$ and $\mathrm{d}^3\mathbf{p}_3$ can be computed analytically, yielding

$$\mathcal{C}[f_\nu] = \sum \frac{1}{2(2\pi)^5} \int \frac{p_2^2 \mathrm{d}p_2}{2E_2} \frac{p_3^2 \mathrm{d}p_3}{2E_3} \Lambda(f_1, f_2, f_3, f_4) F(p_1, p_2, p_3) \ . \tag{1.61}$$

We will omit here the exact form of functions $F(p_1, p_2, p_3)$, but the form of diagonal entries in Eq. 1.61 is the one to be implemented numerically.

1.6.2 Damping function

Damping is easy to illustrate if one includes the possibility of neutrino creation and absorption by the charged-current reactions $\nu_e n \leftrightarrow pe$. An initial ν_e is subsequently found to be a ν_μ with an average probability $\frac{1}{2}\sin^2 2\theta$. As ν_μ, it cannot take part in the weak interactions. So, per CC-reaction, a ν_μ is produced shrinking the length of the initial polarization vector until a perfect chemical equilibrium is reached with $\mathbf{P} = (0,0,0)$. The rate at which it happens is $\frac{1}{2}\sin^2 2\theta\,\Gamma$, where Γ is a typical interaction rate for the ambient physical conditions. One should note that in this case the final length of the total polarization vector is zero, while in the case of a simple dephasing, the off-diagonal elements survive (although in kinematical decoherence).

Moreover, the simple dephasing does not change the projection $\mathbf{P}\cdot\mathbf{B}$, so it is very common to define the damping factor D such that the precession formulas are now

$$\dot{\mathbf{P}} = (\omega\mathbf{B} + \mathbf{V}) \times \mathbf{P} - D\mathbf{P}_T \ , \tag{1.62}$$

where $\mathbf{P}_T$ is the component of the polarization vector transverse to $\mathbf{B}$ and represents the off-diagonal elements of the ϱ matrices. The exact form of the damping parameter is determined by the scattering amplitudes on the background.

In general, for N interactiong species, in the limit of small momuntum transfer in the reactions, the damping factor is [Raffelt 1993]

$$D = \int \mathrm{d}\mathbf{p}\,\mathrm{d}\mathbf{p}'\,S(\mathbf{p}-\mathbf{p}')|G|^2 \ , \tag{1.63}$$

where G is the matrix of coupling constants. For practical purposes, we have adopted the damping factors as in [McKellar 1994]

$$D = \frac{1}{2}F\Big[16+3(n_{\nu_e}+n_{\nu_x})+(8s_{\mathrm{w}}^4+4s_{\mathrm{w}}^2+4)n_{\bar{\nu}_e}+(8s_{\mathrm{w}}^4-4s_{\mathrm{w}}^2+4)n_{\bar{\nu}_x}\Big] \ , \tag{1.64}$$

where the collision rate F is

$$F = \frac{49G_{\mathrm{F}}^2}{12\pi^2}\frac{\zeta^2(4)}{\zeta(3)}T^5 \ . \tag{1.65}$$

Chapter 2

Standard big bang nucleosynthesis

The observation that the Universe is expanding today leads naturally to a hypothesis of a big bang. The large-scale homogeneity and isotropy of the galaxy distributions and an almost perfect black-body spectrum of cosmic microwave background (CMB) radiation further strengthen the idea that the Universe went through a phase whet it was hot and dense enough for photons to be in equilibrium with electrons and protons ($T \sim$ eV). Going even further back in time, we allow the Universe to be even hotter ($T \sim$ MeV) and to act as a thermonuclear reactor, synthesizing the light elements from a primordial plasma. This process is known as the big bang nucleosynthesis (BBN). Based upon well known physics, it has become one of the main pillars of the hot big bang model. It constrains the properties of the Universe when it was a few seconds old, corresponding to temperatures of the MeV scale and is still the earliest cosmological probe available. Its products, the main observables to measure, are the predicted abundances of light elements ^{2}H, ^{3}He, ^{4}He and ^{7}Li.

Probably the most famous result of BBN is the determination of the baryon-to-photon ratio η long before any possibility of extracting it from other probes, such as the CMB (see Fig. 2.1). The agreement between the predicted and measured abundances of light elements, spanning more than nine orders of magnitude, confirmed the consistency and credibility of BBN as a method. Eventually other probes gained advantage in measuring η, and data on the primordial light-element abundances accumulated, so BBN application shifted towards other non-constrained properties of the early Universe, such as concerning neutrinos, extra dimensions, decaying dark matter, etc.. The value of η is now used as an input, usually fixed to its WMAP measurement [Komatsu 2011]

$$\eta = (6.19 \pm 0.14) \times 10^{-10} \quad . \tag{2.1}$$

In this chapter I describe the flow of BBN with an emphasis on the role of non-mixed neutrinos. I briefly discuss measurements of the primordial abundances of light elements and how different values for helium-4 lead to qualitatively different conclusions on the number of light thermalized species in the early Universe. Finally, I motivate the detailed study of asymmetric oscillating neutrinos in the following chapter.

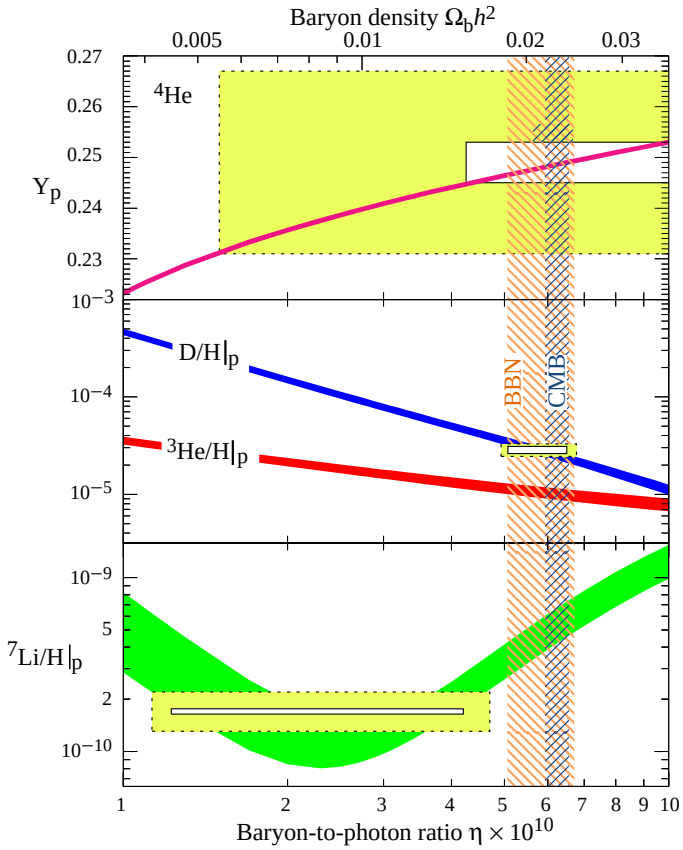

Figure 2.1: The dependence of the light element abundances produced during BBN on the value of baryon-to-photon ratio η. The with of the line represents the theoretical uncertainty and the boxes depict the $\pm 2\sigma$ regions (smaller boxes include only statistical errors and larger box statistical and systematical errors). The narrow vertical band indicates the CMB measure of the cosmic baryon density, while the wider band indicates the BBN concordance range (both at 95% CL). Plot taken from PDG [Nakamura 2010].

2.1 Standard cosmology

The isotropy and homogeneity single out the Friedmann-Robertson-Walker (FRW) metric for the Universe. In comoving spherical coordinates we have

$$\mathrm{d}s^2 = g_{\mu\nu}\mathrm{d}x^\mu \mathrm{d}x^\nu = \mathrm{d}t^2 - a^2(t)\left[\frac{\mathrm{d}r^2}{1-kr^2} + r^2(\mathrm{d}\theta^2 + \sin^2\theta \mathrm{d}\phi^2)\right] \quad , \qquad (2.2)$$

where $a(t)$ is the scale-factor and $k = 1, 0, -1$ determines the spatial curvature for closed, flat and open Universe respectively. For simplicity, we will restrict to a flat Universe, favored by present observations. The expansion of the Universe is governed by the Einstein equations relating the metric with the

total energy-momentum tensor. For the FRW metric, Einstein equations give the Friedmann equation for the Hubble parameter

$$H^2 \equiv \left(\frac{\dot{a}}{a}\right)^2 = \frac{8\,\pi\,G_{\rm N}}{3}\,\rho\ , \tag{2.3}$$

where $G_{\rm N}$ is the Newton gravitational constant and ρ is the energy density of the Universe, which accounts all the species present in the plasma (photons, neutrinos, baryons, electrons, dark matter, etc..). This equation should be complemented with the covariant conservation of energy-momentum tensor ($\partial_\nu T^{\mu\nu}$), which for a perfect fluid of density ρ and pressure p reduces to

$$\frac{{\rm d}(\rho a^3)}{{\rm d}a} = -3\,P\,a^2\ , \tag{2.4}$$

where P is the pressure of the fluid filling the Universe.

At the temperatures of interest, radiation is the dominant form of energy content of the Universe, with the equation of state $P = \rho/3$ and the equations 2.3 and 2.4 give the typical scaling of the energy density with the scale parameter $\rho \sim a^{-4}$, or in terms of temperature $T = T_0 a^{-1}$. We can take the present value of the photon temperature $T_0 = 2.73$ K, since the photons have always scaled the same way.

As usual, the present values of radiation and baryon energy densities are expressed in terms of the parameters $\Omega_i = \rho_i^0/\rho_{\rm cr}$, $i = r, b$, with $\rho_{\rm cr} = 3H_0^2/(8\pi G_{\rm N})$ the critical density today, and the Hubble parameter today $H_0 = 100\,h$ km s^{-1} Mpc^{-1}, with $h = 0.73^{+0.04}_{-0.03}$ [Nakamura 2010]. For baryons, their ratio with photons $\eta = n_b/n_\gamma$ is also commonly used. It is proportional to the initial baryon-antibaryon asymmetry per comoving volume produced at some early stage of the universe evolution. This ratio is constant after the e^+e^- annihilation phase at the value of [Serpico 2004]

$$\eta_{10} \equiv \eta \cdot 10^{10} \simeq 273.45\,\Omega_b h^2\ . \tag{2.5}$$

In thermodynamic equilibrium each particle species i is described by a homogeneous and isotropic phase space distribution function,

$$f_i(p,T) = \left[\exp\left(\frac{E_i(p)}{T} - \xi_i\right) \pm 1\right]^{-1}\ , \tag{2.6}$$

where $E_i(p) = \sqrt{p^2 + m_i^2}$ is the energy, $+/-$ corresponds to the Fermi-Dirac/Bose-Einstein statistics, and ξ_i the chemical potential. For particles that can be emitted and absorbed in any number, such as photons, the chemical potential is zero. A system containing more (fewer) particles than antiparticles has a positive (negative) chemical potential. It is worth noting here that

having an equilibrium distribution does not necessarily mean that the species really is in equilibrium — a species decoupled from the rest of the plasma can retain its equilibrium distribution. This is precisely what happened to relic photons at the epoch of recombination. Although the measured spectra of the CMB is the best thermal curve we know, CMB photons are definitely not in thermal equilibrium at present. They have just retained the spectral shape from when they were in thermal equilibrium.

It is convenient to define the asymmetry of a particle species analogously to the baryonic one, which for neutrinos is

$$\eta_{\nu_i} = \frac{n_{\nu_i} - n_{\bar{\nu_i}}}{n_\gamma} = \frac{1}{12\zeta(3)} \left(\frac{T_{\nu_i}}{T_\gamma}\right)^3 \left(\pi^2 \xi_i + \xi_i^3\right) \quad . \tag{2.7}$$

In the comoving frame, the number density and energy density can be expressed as follows

$$n_i(T) = g_i \int \frac{\mathrm{d}^3\mathbf{p}}{(2\,\pi)^3}\, f_i(p,T) \ , \tag{2.8}$$

$$\rho_i(T) = g_i \int \frac{\mathrm{d}^3\mathbf{p}}{(2\,\pi)^3}\, E_i(p)\, f_i(p,T) \ , \tag{2.9}$$

where g_i is the number of internal degrees of freedom. For example, photons and neutrinos can exist in two helicities ($g = 2$), while for electron–positron plasma $g = 2{\times}2 = 4$. For massless species, pressure is given by $P_i = \rho_i/3$ and entropy density

$$s_i = \frac{\rho_i + P_i}{T_i} = \frac{4}{3}\frac{\rho_i}{T_i} \quad . \tag{2.10}$$

Note that the entropy per comoving volume is a conserved quantity ($s(a)a^3 =$ const.), guaranteed by the conservation of energy-momentum (Eq. 2.4).

It is very common to define the total number of relativistic particle species $g_\star$ as the sum over all bosonic states and fermionic ones:

$$g_\star = \sum_b g_b \left(\frac{T_b}{T_\gamma}\right)^4 + \frac{7}{8}\sum_f g_f \left(\frac{T_f}{T_\gamma}\right)^4 \quad , \tag{2.11}$$

where the additional factor of 7/8 comes from the differences in the first momenta of relevant distributions and we allow different temperatures for different species. This permits us now to write the total energy content and the entropy in the radiation era as[1]

$$\rho = g_\star \frac{\pi^2}{30} T^4 \tag{2.12}$$

$$s = g_\star \frac{2\pi^2}{45} T^3 \ . \tag{2.13}$$

[1]The temperature without a subscript is the one of photons.

For example, in equilibrium plasma consisting of photons, $e^{\pm}$ and three types of neutrinos, at temperatures above the electron mass but below the muon mass, $0.5 \lesssim T \lesssim 100$ MeV, the effective number of relativistic species is

$$g_\star = 10.75 \ . \tag{2.14}$$

In this range of temperatures proper time is connected to temperature through [Dodelson 2003]

$$t = 1.477\,\mathrm{s} \left(\frac{1\,\mathrm{MeV}}{T}\right)^2 \ . \tag{2.15}$$

2.2 Big bang nucleosynthesis

2.2.1 Overview

The main paradigm of bang bang model is that in the early Universe all the particle species (electrons, positrons, photons, neutrinos and nucleons) were in kinetic and chemical equilibrium due to the high interaction rates (weak, strong and electromagnetic). All the baryon content was in the form of free protons and neutrons. Any heavier nuclei that form would soon be dissociated by the surrounding plasma, so they constitute a completely negligible fraction of the baryon density. As expansion proceeds, plasma dilutes and cools, and weak processes lose efficiency. When the rate of a process that keeps a particle species in equilibrium drops below the expansion rate H, the species departs from thermodynamical equilibrium with the remaining plasma. This is the case of neutrinos, which only interact via weak processes and *freeze out* at a temperature of a few MeV. Soon after, at a temperature $T_D \sim 0.7$ MeV, charged-current weak interactions transforming protons to neutrons and vice versa also become too slow to guarantee their chemical equilibrium. The n/p density ratio departs from its equilibrium value and freezes out at the value $\mathrm{n/p} = \exp(-\Delta m/T_D) \sim 1/7$, with the neutron–proton mass difference $\Delta m = 1.29$ MeV. It is further reduced by neutron decays. Although the photon temperature is already below the deuterium binding energy $B_D \simeq 2.2$ MeV, no sizable amounts of ^{2}H are formed via the $n + p \rightarrow {}^2\mathrm{H} + \gamma$ process because of the large photon to nucleon density ratio. Namely, photo-dissociation processes are much more efficient than the deuterium synthesis because the number of photons vastly exceeds the number of baryons (there are $\sim 10^{10}$ photons per nucleon) so it delays deuterium synthesis until temperature T_N, such that $\exp(B_D/T_N)\eta \sim 1$, i.e. $T_N \sim 0.1$ MeV. This moment is known as the deuterium bottleneck — once the ^{2}H abundance reaches sizable amounts, the whole nuclear-process network sets in (Fig. 2.2), leading to heavier-nuclei

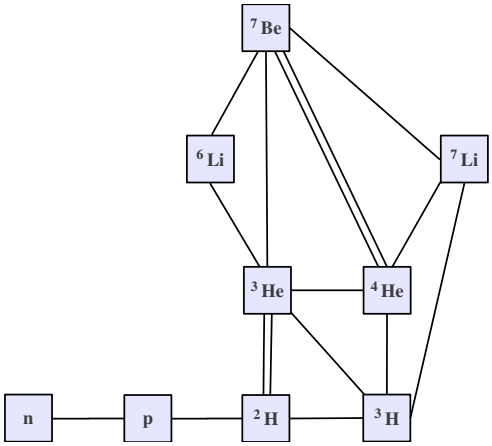

Figure 2.2: The most relevant reactions for the primordial nucleosynthesis.

production (note the rise of tritium and ^{4}He abundance and deuterium depletion at 0.1 MeV). The delicate role of deuterium during BBN makes it a sensitive baryometer as seen from Fig. 2.1 where the BBN-preferred region is dominated by deuterium abundance. As it turns out, with η fixed to the WMAP value, deuterium proves necessary to break degeneracies between dif-

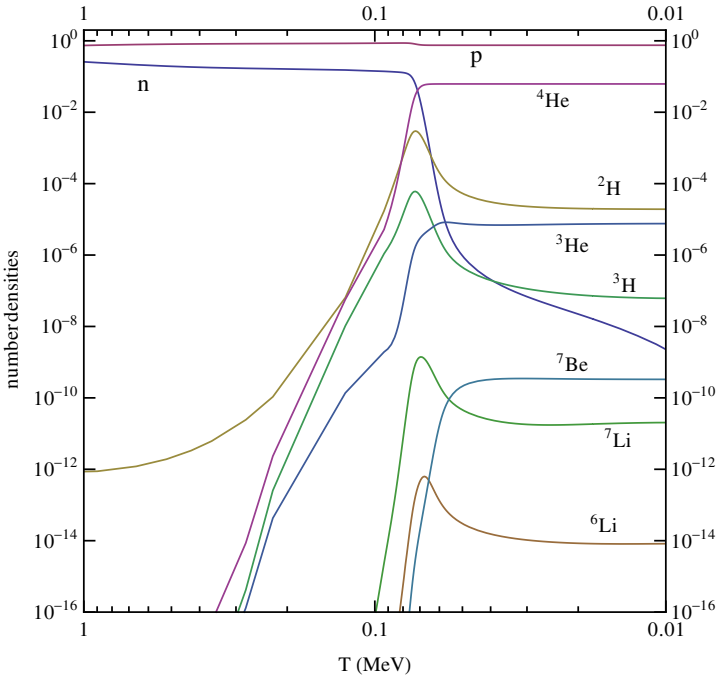

Figure 2.3: The evolution of nuclides with photon temperature.

ferent parameters.

To predict the abundances of various nuclei, one must search for a simultaneous solution to a set of coupled equations governing the evolution of nuclei, the expansion of the Universe, taking into account the covariant conservation of the total–energy momentum tensor, of the baryon number and the electric charge. This is typically done numerically. There are different public codes available that tackle this issue. The research presented in this manuscript is mostly based on results obtained using `PArthENoPE`, a code developed by the Naples Astroparticle Physics Group [Pisanti 2008].

Interestingly, however, it is easy to obtain a qualitative estimate of the main BBN outcome, the abundance of ^{4}He. The final density $n_{^4\mathrm{He}}$ of ^{4}He is relatively insensitive to the whole nuclear network, and a very good approximation is to assume that all neutrons that have not decayed until T_N are eventually bound into helium nuclei. This leads to the famous result for the helium mass fraction $Y_p \equiv 4\, n_{^4\mathrm{He}}/n_b$

$$Y_p \sim \frac{2}{1+\exp(\Delta m/T_D)\exp(t(T_N)/\tau_n)} \sim 0.25 \quad , \tag{2.16}$$

with $t(T_N)$ the value of time at T_N and τ_n the neutron lifetime. All state-of-the-art numerical simulations produce values close to this estimate and, more importantly, experimental measurements cluster around this value.

2.2.2 Neutrino decoupling and effective number of neutrinos

At energies above the MeV scale, the weak interaction rate is high enough to keep neutrinos in thermal equilibrium with the rest of the electromagnetic plasma. When the rate of weak interactions $\Gamma_w \simeq \langle \sigma_w\, v\rangle n_{e^\pm} \sim G_F^2\, T^2 \times T^3$ drops below the Hubble expansion rate at the period ($\Gamma_w < H \sim \sqrt{G_N} T^2$), neutinos decouple from the rest of the plasma, retaining their equilibrium distributions. An accurate estimate of the decoupling temperatures for the electron neutrinos is 2.3 MeV, while for μ and τ is a slightly higher (3.5 MeV), because they interact only via neutral current processes [Dolgov 2002a].

Soon after, at $T \sim m_e$, electrons and positrons annihilate into photons, heating up the thermal bath, which does not communicate anymore with the neutrinos. This is the origin of different temperatures of photons and neutrinos [Kolb 1990]. From the conservation of entropy density per comoving volume, it is possible to get a very good estimate for the ratio of the temperatures. Before the annihilation (but below the muon annihilation epoch), we have

$$(s_{e^\pm,\gamma} + s_\nu)\, a^3 = \text{const.} \quad , \tag{2.17}$$

with both species sharing the temperatures T_{in}. After the $e^{\pm}$ annihilation, we have the separate entropy conservations for electromagnetic plasma and neutrinos

$$\begin{aligned} s_\nu(a_{in})a_{in}^3 &= s_\nu(a_{end})a_{end}^3 \ , \\ s_{e^\pm,\gamma}(a_{in})a_{in}^3 &= s_\gamma(a_{end})a_{end}^3 \ . \end{aligned} \tag{2.18}$$

Taking the ratio of the two equation and just by counting the number of particle species that contribute to the entropy before and after the $e^{\pm}$ annihilation, we arrive to the ratio of neutrino and photon temperature

$$\frac{T_\nu}{T} = \left(\frac{2}{2+4\times 7/8}\right)^{1/3} = \left(\frac{4}{11}\right)^{1/3} \simeq 1.401 \ , \tag{2.19}$$

After the $e^{\pm}$ annihilation, we can express the total energy content of the Universe in terms of the photon energy density $\rho_\gamma = \pi^2 T^4/15$,

$$\rho = \rho_r = \rho_\gamma \left(1 + \frac{7}{8}\left(\frac{4}{11}\right)^{4/3} N_{\rm eff}\right) \ . \tag{2.20}$$

This equation is in fact a definition of the effective number of neutrinos $N_{\rm eff}$, which parametrizes the contribution of neutrinos to energy density.

Naively, one would expect $N_{\rm eff} = 3$ for three species of active neutrinos or $N_{\rm eff} = 4, 5, \ldots$ if there are more than three completely thermalized neutrino-like species. However, being just a historical artifact conveniently expressing the energy content of the Universe, it can have non-integer values. Any deviation from the simplest ($m_\nu = 0$, $\xi_\nu = 0$) equilibrium distribution for neutrinos also leaves a trace in $N_{\rm eff}$. E.g., treating $e^- e^+$ annihilation properly, one finds that the simplest approximation of so-called *instantaneous decoupling* is wrong: electrons from the high-energy distribution tails do have enough energy to annihilate into neutrinos, producing small non-thermal distortions in high-energy parts of neutrino spectra, and making them effectively hotter. This translates into increase of their energy contribution to the standard value of $N_{\rm eff} = 3.04$ [Mangano 2002].

The effect of increased $N_{\rm eff}$ on the primordial abundances of light elements is not difficult to understand: higher energy content means faster expansion, so there is less neutrons decaying before the BBN onset meaning more neutrons to make light nuclei — *increasing* $N_{\rm eff}$ *raises* Y_P *and* ^{2}H/H.

2.2.3 Role of neutrinos in weak rates

Neutrinos enter the set of BBN equations in two places: their mere presence contributes to the total energy density, thus governing the expansion rate

of the Universe through the Friedmann equation 2.3; and electron neutrinos play a direct role in the weak processes regulating the neutron-to-proton ratio through the reactions

$$\begin{aligned} &(a) \quad \nu_e + n \to e^- + p \quad , \qquad (d) \quad \bar{\nu}_e + p \to e^+ + n \ , \\ &(b) \quad e^- + p \to \nu_e + n \quad , \qquad (e) \quad n \to e^- + \bar{\nu}_e + p \ , \\ &(c) \quad e^+ + n \to \bar{\nu}_e + p \quad , \qquad (f) \quad e^- + \bar{\nu}_e + p \to n \ . \end{aligned} \tag{2.21}$$

This means that, to get an accurate theoretical prediction for light-element abundances, processes $(a) - (f)$ require a careful and thorough treatment.

In the so-called Born approximation of the weak rates, the calculation is straightforward, following from V−A theory, in the limit of infinite nucleon mass [Weinberg 2008]. For example, the neutron decay rate takes the form (neglecting the very small neutrino mass)

$$\begin{aligned} \omega_b(n \to e^- \bar{\nu}_e p) = \ & \frac{G_{\rm F}^2}{2\pi^3}(C_{\rm V} + 3C_{\rm A}^2) \\ & \int {\rm d}p_e \, p_e^2 \, p_\nu^2 \, \Theta(p_\nu) \, [1 - f_{\bar{\nu}_e}(p_\nu)] \, [1 - f_e(p_e)] \quad , \end{aligned} \tag{2.22}$$

where $C_{\rm V}$ and $C_{\rm A}$ are the nucleon vector and axial couplings, and $p_\nu = \Delta m - \sqrt{p_e^2 + m_e^2}$. The rates for all the other processes are obtained from 2.22 by changing the statistical factors and the expression for the neutrino energy in terms of the electron energy. An average can be performed at this level of approximation over an equilibrium Fermi-Dirac distribution for leptons, and the accuracy of the so-obtained rates is of the order of 10%, propagating to a few percent accuracy in the final abundances [Serpico 2004]. The main source of uncertainty in weak rates represent the couplings C_A and C_V. Luckily, they enter in the same form in all the processes as in the pure nucleon decay (e) whose half-life is experimentally measured $\tau_n^{ex} = (885.7 \pm 0.8)$ s [Nakamura 2010], so they can be factored out, leaving the neutron lifetime that is the main "theoretical" uncertainty in the calculation of weak rates. In the present-day era of precision cosmology it is necessary to aim for higher accuracy for the weak rates calculation. The inclusion finite-nucleon-mass corrections, electromagnetic radiative corrections and thermal radiative corrections rendered the calculations of weak rates accurate at per mille level [Serpico 2004].

As seen in Eq. 2.22, electron neutrinos enter the BBN equations at a fundamental level, so that their momentum distribution is fully relevant. Any asymmetry (chemical potential) they possess manifests in the weak rates and easily translates to the final abundances. Qualitatively, this effect is also understood directly from reactions $(a) - (f)$: an excess of neutrinos over antineutrinos ($\xi_{\nu_e} > 0$) shifts the chemical equilibrium toward protons, reducing

the n/p ratio and resulting in lower abundances; an excess of antineutrinos ($\xi_{\nu_e} < 0$) leads to an increase of Y_p and ^{2}H/H. There is a degeneracy between electron neutrino chemical potential ξ_{ν_e} and the effective number of neutrinos $\Delta N_{\rm eff}$ — while $\xi_{\nu_e} > 0$ decreases the abundances, $\Delta N_{\rm eff}$ raises n/p ratio, canceling any effect on the final abundances. The situation is further complicated because a non-zero chemical potential also increases the effective number of neutrinos by the amount

$$\Delta N_{\rm eff}^{\xi_i} = \frac{30}{7}\left(\frac{\xi_{\nu_i}}{\pi}\right)^2 + \frac{15}{7}\left(\frac{\xi_{\nu_i}}{\pi}\right)^4 \tag{2.23}$$

per flavor $i = e, \mu, \tau$, so one should not make premature conclusions, but rather perform simulations.

2.3 Observational abundances

Extracting primordial abundances from a variety of observations is not a trivial task. Astrophysical environments are typically altered by the stellar activity throughout the history of the Universe, so when inferring the primordial values of the abundances one must either look at the least contaminated parts of the Universe or know enough physics to extrapolate present measured abundance to their original values.

For example, any ^{2}H nucleus contained in a pre-stellar nebulae is burned out during their collapse, and we don't know of any astrophysical sources of them. Hence, the post-BBN deuterium evolution is expected to be a monotonic function of time, and any astrophysical deuterium measurement can be assumed to represent a lower bound on its primordial abundance. The best values are the ones obtained from the observation of old structures such as high redshift Quasar Absorption Systems (QAS) — hydrogen-rich clouds at high redshifts that absorb light from the background quasars. Although the isotope shift of the absorption line makes the detection relatively easy, only few observations can claim to have measured the primordial deuterium, meeting all the requirements: (i) neutral hydrogen column density in the range[2] $17 \lesssim \log[\mathrm{N(H}_I)/\mathrm{cm}^{-2}] \lesssim 21$; (ii) low metallicity [M/H] to reduce the chances of deuterium astration; and (iii) low internal velocity dispersion of the atoms of the clouds, allowing the isotope shift of only 81.6 km/s to be resolved. For this reason, only a handful of determinations of pristine ^{2}H/H have been made (see Fig. 2.5). In Ref. [Iocco 2009] a consistent analysis of these measurements

[2] There is a lower limit on column density determined by the sensitivity of the detection and a upper limit to avoid saturation.

has been combined, giving a value for the deuterium-to-proton ratio

$$^2\mathrm{H/H} = \left(2.87^{+0.22}_{-0.21}\right) \times 10^{-5} \quad . \tag{2.24}$$

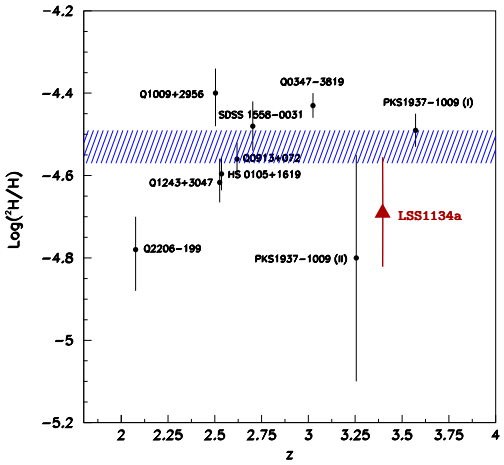

Figure 2.4: The nine measurements of QSA's used in the global analysis in Ref. [Iocco 2009] (black points). The horizontal band represents the value of Eq. 2.24. The red triangle is the observation in Ref. [Fumagalli 2011]. Figure adapted from [Iocco 2009].

All of these measurements have heavy-element abundances that exceed the BBN prediction by many orders of magnitude, so one could in principle argue about their credibility. However, a new observation claims a detection of two genuinely pristine gas clouds with no detectable elements heavier than hydrogen [Fumagalli 2011]. The observed absorbers are at redshift $z \simeq 3.4$, when the Universe was only two billion years old. Only one of them has a detectable deuterium line from which one can infer the deuterium abundance (LLS1134a in Fig. 2.5) in very good agreement with the result of Eq. 2.24.

The situation regarding the primordial abundance of ^{4}He is somewhat the reverse of that of deuterium. In this case, hydrogen burning in the successive stellar population can only increase the amount of ^{4}He. Luckily, stellar activity can also be tagged by measuring the abundance of "metals" (nuclei with $Z > 4$) such as C, N and O. Since the Universe is born with zero metallicity, measuring ^{4}He in old and unevolved systems and extrapolating the ^{4}He–metallicity (O/H, N/H or C/H) correlations to zero gives the primordial abundance of helium-4.

Although this is a very intuitive and reasonable approach, it depends very much on the way one treats systematic uncertainties. That is why there are

different values appearing in the literature. The analysis in Ref. [Iocco 2009] yields a value

$$Y_p = 0.250 \pm 0.003 \ , \tag{2.25}$$

which will be used in most of this manuscript.

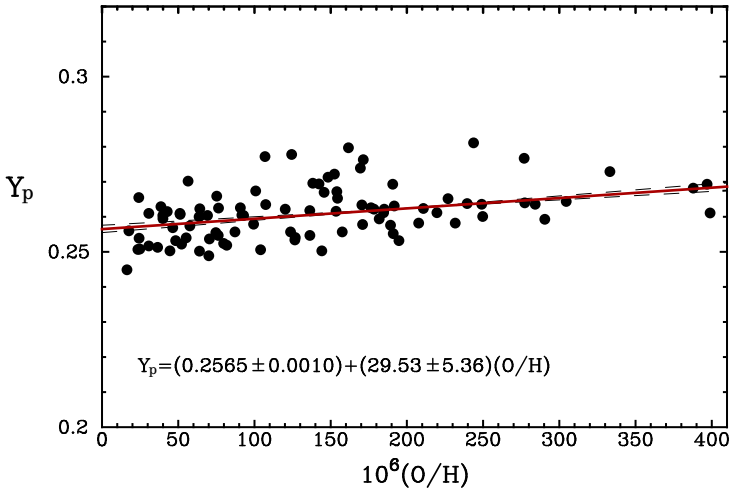

Figure 2.5: Linear regression of the helium mass fraction Y_p vs. oxygen abundance. Figure adapted from [Izotov 2010].

The determination of the abundances of other nuclei produced in primordial nucleosynthesis is still an open question with often different and inconsistent answers. Two of them, of ^{3}He and ^{7}Li, are even famous through the corresponding "^{3}He and ^{7}Li problems". It is expected that ^{3}He should have a similar chemical evolution as ^{4}He and therefore its abundance should have the same type of correlation as Y_p. However, measurements do not show significant dependence on the location (or metallicity) in the Galaxy, so it is common to report only the upper limit to the primordial ^{3}He abundance $^3\mathrm{He/H} < (1.1 \pm 0.2)\times 10^{-5}$ [Steigman 2007]. Numerical simulations typically satisfy this constraint very easily and therefore it does not carry information relevant for physics (??).

The abundance of ^{7}Li, on the other hand, although not difficult to measure, suffers from a very rich post-BBN life. It can be created and destroyed in stars, and the values measured on the surface of very young stars may not reflect the situation deeper in the center because of the turbulent convective flows a star typically exerts. Inferring primordial value from measurements requires thorough and reliable models of the stellar interior. That is why, on the observational side, there are results incompatible at more-than-2σ level. It is generally believed that, as for the lithium problem, a piece of stellar physics

is missing. Therefore, abundances of ^{3}He and ^{7}Li are usually not considered in the conservative statistical BBN analysis and are rather invoked to support a particular non-standard BBN scenario.

2.4 Results

A typical outcome of a BBN analysis is shown in Figure 2.6. For each point of a grid in $(\xi_{\nu_e}, \Delta N_{\rm eff}^{extra})$, a BBN simulation is run with the code `PArthENoPE`. The calculated abundances are then confronted with their measured values to construct a likelihood function

$$\mathcal{L}((\xi_{\nu_e}, \Delta N) \propto \exp\left(-\chi^2(\xi_{\nu_e}, \Delta N)/2\right) \quad , \tag{2.26}$$

with χ^2 constructed from the abundances X_i

$$\chi^2(\xi_{\nu_e}, \Delta N) = \sum_{ij} [X_i(\xi_{\nu_e}, \Delta N) - X_i^{obs}] W_{ij}(\xi_{\nu_e}, \Delta N) [X_j(\xi_{\nu_e}, \Delta N) - X_j^{obs}] \ . \tag{2.27}$$

The proportionality constant can be obtained by requiring normalization to unity, and $W_{ij}(\xi_{\nu_e}, \Delta N)$ denotes the inverse covariance matrix,

$$W_{ij}(\xi_{\nu_e}, \Delta N) = [\sigma_{ij}^2 + \sigma_{i,exp}^2 \delta_{ij} + \sigma_{ij,other}^2]^{-1} \quad , \tag{2.28}$$

where σ_{ij} and $\sigma_{i,exp}$ represent the nuclear rate uncertainties and experimental uncertainties of nuclide abundance X_i, respectively, while by $\sigma_{ij,other}^2$ we denote the propagated squared error matrix due to all other input parameter uncertainties (τ_n, $\Omega_b h^2$, $G_{\rm N}$, etc..). Typically the experimental errors vastly exceed all the others, which can be safely neglected.

From Fig. 2.6 it seems that the results prefer higher effective number of neutrinos, minimizing the χ^2 close to $N_{\rm eff} = 4$. In fact, marginalizing the likelihood over electron neutrino chemical potential does give a similar value, but is it correct to assume uniform distribution for ξ_{ν_e}? In the simplest of scenarios, we would expect the neutrino asymmetry to be of the same order of magnitude as the baryon one $\sim 10^{-10}$ (see Sec. 3). From Eq. 2.7 it reads that the chemical potential and the asymmetry are almost linear and of the same order of magnitude. For the scale of ξ_{ν_e} plotted it is effectively zero, so we should cut the plane at $\xi_{\nu_e} = 0$ after which we are left with a χ^2 as a function of $\Delta N_{\rm eff}$ only. This χ^2 now excludes additional relativistic degrees of freedom ($\Delta N_{\rm eff} = 1$) at 3σ confidence level (see Fig. 2.7).

Recently new measurements and methods have been applied to measure the helium mass fraction [Aver 2010, Izotov 2010]. Typically they agree on a

larger central value with respect to the result of Eq. 2.25:

$$Y_p = 0.2565 \pm 0.0010(\text{stat.}) \pm 0.0050(\text{syst.}) \quad [\text{Izotov 2010}] \ , \quad (2.29)$$

$$Y_p = 0.2573 \pm 0.0033 \quad [\text{Aver 2010}] \ . \quad (2.30)$$

In the so-called Standard BBN, which does not treat neutrino asymmetries, such results seem to exclude $N_{\rm eff} \simeq 3$ at more than 2σ confidence level (see Fig. 2.7) and have been used as an evidence for non-standard big bang nucleosynthesis.

Extra radiation density can also be measured with other cosmological probes. It postpones the epoch of matter-radiation equality; in the CMB power spectrum it boosts the amplitude of the first acoustic peak of the angular power spectrum and shifts all peaks to smaller scales. Moreover, the power spectrum of density fluctuations on small scales is suppressed, leading to observable effects in the cosmic large-scale structures (LSS). However, the sensitivity of CMB and LSS analysis to extra effective number of neutrinos is rather weak. The best answer at present coming from WMAP collaboration is a modest constraint $2.6 \lesssim N_{\rm eff} \lesssim 6$ at 2σ [Komatsu 2011]. Future experiments, such as PLANCK, are designed to have much better precision [Hamann 2008] on this and all the other cosmological parameters. In this case a possible contribution $\Delta N_{\rm eff} \sim 0.2$ can make a difference between discovery of a new degree of freedom or neutrino asymmetry. Considering this a question arises: What is the maximal contribution that active, normal, but asymmetric neutrinos can leave to $\Delta N_{\rm eff}$?

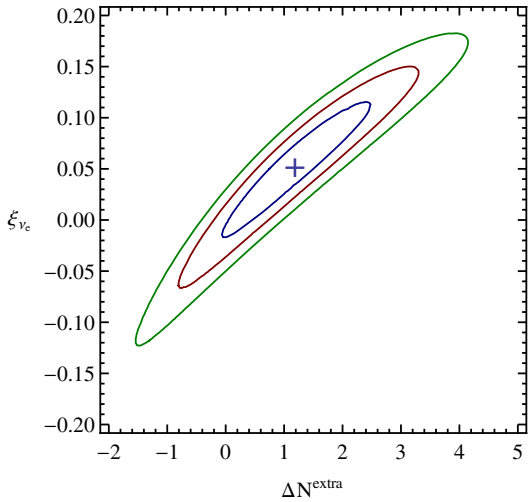

Figure 2.6: BBN bounds on electron chemical potential and the contribution to effective number of neutrinos coming from extra degrees of freedom. The contours represent 1σ-, 2σ- and 3σ-confidence regions. A light preference to $\Delta N_{\rm eff} = 1$ ($N_{\rm eff} = 4$) is observed. For this analysis the values for the experimental abundances of ^{2}H and ^{4}He are taken from Ref. [Iocco 2009] (Eqs. 2.24 and 2.25).

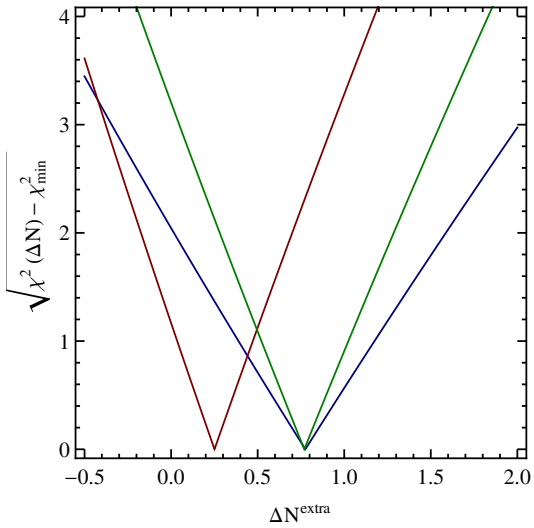

Figure 2.7: $\sqrt{\chi^2(\Delta N_{\rm eff}) - \chi^2_{min}}$ for different values of measured ^{4}He mass fraction: *a*) $Y_p = 0.250(3)$ – red curve, *b*) $Y_p = 0.2565(60)$ – blue curve and *c*) $Y_p = 0.2573(33)$ – green curve.

Chapter 3

Degenerate big bang nucleosynthesis

Neutrino oscillations have implications in many research areas in particle and astroparticle physics. However, the consequences of non-zero neutrino mixing in cosmology are usually not considered relevant, despite the fact that relic neutrinos are the second most abundant particles in the Universe, with almost the same number density as photons. The reason is well known: if we believe that all neutrino flavors were produced thermally in the early hot Universe, then they all had the same energy spectra. Any asymmetry they possessed in the early stages of the Universe was then redistributed between lepton and baryon sector in the sphaleron era leaving the lepton asymmetry of the same order as baryon one, i.e. $\sim 10^{-10}$. Thus neutrino oscillations can not modify the properties of cosmological neutrinos (except for very small effects from non-instantaneous neutrino decoupling [Mangano 2005]). However, lepton asymmetry in the neutrino sector is in principle unconstrained or weakly constrained with the values $\mathcal{O}(1)$ still allowed[1]. There are models in which neutrino asymmetry is orders of magnitude larger than the baryon one; e.g. a small mixture with sterile neutrinos could cause both species to undergo opposite and exponential asymmetry growth sometimes even flipping their original sign [Bell 1999, Enqvist 1999].

Big Bang nucleosynthesis is the most precise method to put bounds on neutrino asymmetries and it is sensitive only to values $|\eta_\nu| \gtrsim 10^{-2}$. Only larger values lead to significant enhancements of neutrino contribution to the energy density or to changes in the weak rates leaving an observable trace in the light element abundances. In particular, the primordial abundance of ^{4}He depends on the presence of an electron neutrino asymmetry and in the case of no extra d.o.f. sets a stringent bound electron neutrino degeneracy parameter

$$-0.021 \leq \xi_{\nu_e} \leq 0.005 \ . \tag{3.1}$$

This corresponds to a cut in Fig. 2.6 at $\Delta N_{\rm eff}^{extra} = 0$. If there were no mixing, the constraints on the total neutrino asymmetry would be very loose, allowing values even of the order of unity.

[1] Charged lepton asymmetry is very well constrain by imposing charge neutrality of Universe.

If neutrino mixing is effective before the the BBN onset, the constraint (3.1) applies to all other flavors as well. This in turn also implies that, *if neutrinos indeed, reach perfect kinetic and chemical equilibrium before they decouple*, any large excess in cosmic radiation density, if observed, must be ascribed to extra relativistic degrees of freedom since the additional contribution to radiation density due to non vanishing ξ_{ν_α} is very small. Assuming that the neutrino distributions are given by their equilibrium form, the BBN bound on the neutrino degeneracies leads to the following upper limit on the excess contribution to $N_{\rm eff}$ [Dolgov 2002b],

$$\Delta N_{\rm eff} = \sum_{\alpha=e,\mu,\tau} \left[\frac{30}{7} \left(\frac{\xi_{\nu_\alpha}}{\pi} \right)^2 + \frac{15}{7} \left(\frac{\xi_{\nu_\alpha}}{\pi} \right)^4 \right] \lesssim 0.0006 \ , \tag{3.2}$$

which is tiny, even compared with the value of $N_{\rm eff} = 3.046$ found solving the neutrino kinetic equations in absence of asymmetries [Mangano 2005].

The problem, however, was proven to be not as simple [Pastor 2009]. Flavor oscillations driven by $\Delta m^2_{\rm atm}$ take place when neutrinos are still fastly scattering off the surrounding medium, so that the changes in their distribution due to oscillations are efficiently readjusted into an equilibrium Fermi-Dirac function. Instead, flavor conversions due to $\Delta m^2_{\rm sol}$ and θ_{12} occur around neutrino decoupling. This implies, at least in principle, that if neutrinos succeed in achieving comparable asymmetries in all flavors before BBN, their distributions might acquire distortions with respect to equilibrium values due to inefficient interactions.

This can be easily understood by a simple example. Suppose that at temperatures higher than $2 - 3$ MeV we start with a vanishing total asymmetry, but $\eta^{\rm in}_{\nu_e} = -2\eta^{\rm in}_{\nu_x} \neq 0$ and we artificially switch-off scattering and pair processes. Due to solar-scale oscillations, in the case of maximal mixing, asymmetries in each flavor will eventually vanish, but the resulting neutrino distributions will not correspond to equilibrium, since averaging two equilibrium distributions with different chemical potential does not yield a Fermi-Dirac function. Only scatterings and pair-processes can drive it back to an equilibrium distribution with, in this case, zero chemical potential.

Although this example is quite extreme and unrealistic it illustrates well that the interplay of neutrino freeze–out and $\Delta m^2_{\rm sol}$ oscillations deserves more careful scrutiny. In fact, depending on the initial flavor neutrino asymmetries and the value of θ_{13}, the final neutrino distributions at the onset of BBN might show non-thermal distortions which change the neutron-proton chemical equilibrium due to the direct role played by electron (anti)neutrinos. Moreover, this corresponds to an asymmetry-depending parameter $N_{\rm eff} > 3$ which is not anymore given by the equilibrium value of 2.23 due to inefficient entropy

transfer from neutrinos to the electromagnetic plasma. These features will prove to be quite important in case of large initial asymmetries and opposite values for ν_e and $\nu_{\mu,\tau}$ chemical potentials. It was shown that with fine-tuned and opposite initial asymmetries, the BBN bound could be respected, with a residual off-equilibrium excess of radiation density.

In papers [Mangano 2011a] and [Mangano 2011b] we have considered a wide range of values of the initial neutrino asymmetries and solved their evolution with the corresponding kinetic equations, including both collisions and oscillations. The obtained shape of the neutrino distributions was then plugged into the BBN dynamics to obtain more accurate bounds on the total lepton asymmetry stored in the neutrino sector, as well as the way it was distributed at some early stage in the ν_e and ν_x flavors.

3.1 Evolution of asymmetric neutrinos

We are interested in calculating the evolution of the active neutrino spectra from large temperatures, when they followed a Fermi-Dirac form, until the BBN epoch. This includes taking into account neutrino interactions among themselves and with charged leptons, as well as flavor oscillations, which become effective at similar temperatures. The equations of motion for the ϱ matrices are

$$\mathrm{i}\,\dot{\varrho}_{\mathbf{p}} = +\left[\frac{\mathsf{M}^2}{2p},\varrho_{\mathbf{p}}\right]+\sqrt{2}\,G_{\mathrm{F}}\left[\left(-\frac{8p}{3m_{\mathrm{w}}^2}\,\mathsf{E}+\varrho-\bar{\varrho}\right),\varrho_{\mathbf{p}}\right]+C[\varrho_{\mathbf{p}}]\ , \quad (3.3)$$

$$\mathrm{i}\,\dot{\bar{\varrho}}_{\mathbf{p}} = -\left[\frac{\mathsf{M}^2}{2p},\bar{\varrho}_{\mathbf{p}}\right]+\sqrt{2}\,G_{\mathrm{F}}\left[\left(-\frac{8p}{3m_{\mathrm{w}}^2}\,\mathsf{E}+\varrho-\bar{\varrho}\right),\bar{\varrho}_{\mathbf{p}}\right]+C[\bar{\varrho}_{\mathbf{p}}]\ . \quad (3.4)$$

In the calculations presented both mass-squared differences and the angles θ_{12} and θ_{23} were fixed to the best-fit values in Ref.[Schwetz 2011]. Varying these parameters within the allowed 3σ ranges does not modify the results. Instead, we considered the whole presently allowed region for θ_{13}, in the range $0.001 < \sin^2\theta_{13} < 0.04$ at 3σ (see Table 1.1) adding the case of zero θ_{13} for comparison.

The small baryon density in the early Universe implies that the refractive matter term proportional to the difference between the charged lepton and antilepton number densities (CP asymmetric) can be neglected compared to the CP symmetric term, proportional to the sum of energy densities [Notzold 1988]. This appears in Eq. 3.4 through the flavor diagonal matrix of charged-lepton energy densities E (see Table 1.2).

The onset of flavor oscillations occurs at a the temperature when the vac-

uum and the background matter terms become equal in magnitude

$$\frac{\Delta m^2}{2p}\cos 2\theta \sim \frac{8\sqrt{2}G_{\rm F}p}{3m_W^2}(\varrho_{l^-}+\varrho_{l^+}) \ . \tag{3.5}$$

There are two flavor oscillations happening. First, at $T \simeq 15$ MeV, $\nu_\tau - \nu_\mu$ mixing driven by Δm^2_{31} and θ_{23} set on [Dolgov 2002b]. That is long before neutrino decoupling, so the weak interactions are still very effective meking the two species reach full equilibrium. That is why, for the rest of the treatment, it is enough to consider the 2×2 case with ν_e's and ν_x's representing both μ and τ species. For the same reason, our numerical calculations start at $T = 10$ MeV with initial degeneracy parameters $\xi_{\nu_x} \equiv \xi_{\nu_\mu} = \xi_{\nu_\tau}$ and ξ_{ν_e}.

For flavor neutrino oscillations involving ν_e's and ν_x's, the relevant parameters in Eq. 3.5 are Δm^2_{31} and θ_{13}, so we get that the oscillations set on at temperature

$$T_c \simeq 19.9\left(\frac{p}{T}\right)^{-1/3}\left(\frac{|\Delta m^2_{31}|}{\mathrm{eV}^2}\right)^{1/6}\ \mathrm{MeV} \tag{3.6}$$

if $\cos 2\theta_{13} \simeq 1$ and $e^\pm$ are taken as relativistic particles. For $|\Delta m^2_{31}| = 2.5\times 10^{-3}$ eV^2 and an average neutrino momentum, one finds $T_c \simeq 5$ MeV. It is this fact that complicates the whole problem – T_c is too close to neutrino decoupling temperature $(2-3$ MeV)! That is why the interplay between mixing (tending only to average two distributions out) and collisions (actually exchanging momenta and driving the distributions ot equilibrium form) is so delicate. A proper analysis of neutrino influence on BBN has to account fo the whole shape of the neutrino distribution(s).

Luckily, the spectral distorsions from the equilibrium shape are proven to be small [Pastor 2009]. So, for the purpose of implementing the effect in the BBN code, it is enough to parametrize the numerically generated spectra with two *effective* parameters ξ_{ν_α} and T_{ν_α}. The emphasis is put that the parameters are just effective, because, strictly speaking, since the spectra are in general off-equilibrium, the degeneracy parameter and the temperature can not be defined. These effective parameters are then included in `PArthENoPE` for each moment in time. This approach is justified since the nuclear network does not give feedback to the neutrino evolution; neutrinos influence nucleosynthesis, but not vice versa.

3.1.1 Examples of neutrino evolution

In Figure 3.1, left upper panel, we show the final energy spectra of relic electron neutrinos and antineutrinos in the extreme case of zero θ_{13} and non-zero total asymmetry ($\eta_\nu = -0.41$, and $\eta^{\rm in}_{\nu_e} = 0.82$). The upper (lower) solid line

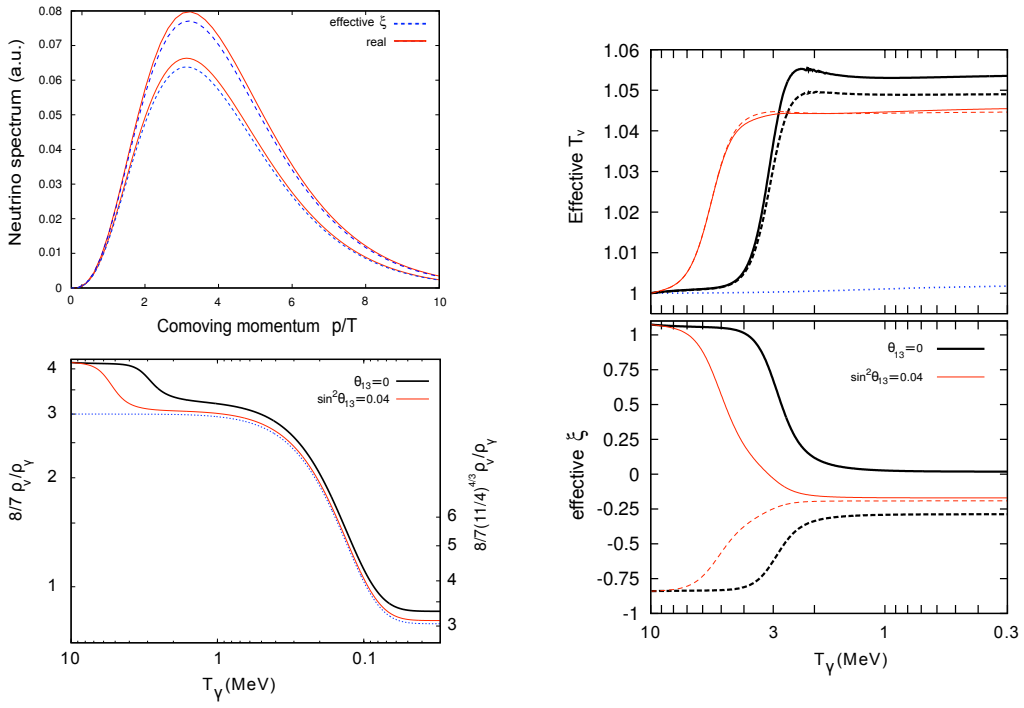

Figure 3.1: *Top Left panel:* The final energy spectra of relic electron neutrinos and antineutrinos in arbitrary units for $\eta_\nu = -0.41$, and $\eta^{\rm in}_{\nu_e} = 0.82$ and with vanishing θ_{13}. Upper (lower) solid line stands for electron neutrino (antineutrino) calculated numerically (label "real"). Upper (lower) dotted line stands for electron neutrino (antineutrino) given by a Fermi/Dirac distribution in terms of the fitted parameters ξ_{ν_α} and T_{ν_α}.
Bottom Left panel: Evolution of the neutrino energy density corresponding to the rigth panel. The vertical axis is marked with $N_{\rm eff}$, left before e^+e^- annihilation, right afterwards. The solid curves correspond to vanishing θ_{13} (upper black line) and $\sin^2\theta_{13} = 0.04$ (lower red line). The case without asymmetries is shown for comparison (blue dotted line).
Right Panel: Evolution of the effective comoving temperatures and degeneracy parameters of electron (solid lines) and muon or tau (dashed lines) neutrinos in the same case. Both the case of vanishing θ_{13} (thick black lines) and $\sin^2\theta_{13} = 0.04$ (thin red lines) are shown. The effective temperature for the case without asymmetries is shown in the upper panel for comparison (blue dotted line).

stands for the spectra of electron neutrinos (antineutrinos) calculated numerically, while the corresponding dotted lines are described by a Fermi/Dirac distribution in terms of the effective electron neutrino chemical potential and temperature. Both cases lead to the same value of the electron neutrino asymmetry but the real calculation shows that an excess of radiation in neutrinos remains. The right panel of the same Figure illustrates precisely that: As soon as the flavor conversions start, the entropy transfer from the residual interactions distorts the equilibrium spectra effectively heating them up. Hotter neutrinos contribute more to the energy density rising the effective number of neutrinos above its equilibrium value.

In the right panel of Fig. 3.1 we show the evolution of the ratio of neutrino to photon energy densities, ρ_ν/ρ_γ, properly normalized so that it corresponds to $N_{\rm eff}$ at early and late times. The fast drop of ρ_ν/ρ_γ at $T \sim 0.2$ MeV represents photon heating by e^+e^- annihilations. The case without asymmetries (dotted line) ends at late times at $N_{\rm eff} = 3.046$ instead of 3 because of residual neutrino heating [Mangano 2005]. We also show (solid lines) the evolution for our main example, where initially $N_{\rm eff} = 4.16$ for our choice of neutrino asymmetries. One can see that as soon as oscillations become effective reducing the flavor asymmetries, the excess of entropy is transferred from neutrinos to the electromagnetic plasma, cooling the former and heating the latter, but this process is only very effective for *large* values of θ_{13}. While the final $N_{\rm eff}$ is 3.1 for $\sin^2\theta_{13} = 0.04$, for vanishing θ_{13} a significant deviation from equilibrium survives and leads to a final enhanced value of $N_{\rm eff} = 3.3$.

Figure 3.2 illustrates how the neutrino asymmetry evolution depends on the value of θ_{13} and the mass hierarchy. Typically, only cases with total asymmetry close to zero (i.e. $\eta_{\nu_e} \simeq -2\eta_{\nu_x}$) satisfy stringent BBN bounds on η_{ν_e}. If $\Delta m^2_{31} > 0$ (normal neutrino mass hierarchy, NH) both terms in Eq. 3.5 have the same sign and neutrino oscillations follow an MSW conversion when the vacuum term overcomes the matter potential at $T \simeq T_c$. The degree of conversion depends in this case on the value of θ_{13} [Dolgov 2002b, Wong 2002, Abazajian 2002], being very efficient compared with $\theta_{13} = 0$ if this mixing angle presents a value close to the upper bound.

The conversion for non-zero θ_{13} is more evident for the inverted mass hierarchy, due to the resonant character of the MSW transition for $\Delta m^2_{31} < 0$. Indeed, for IH the sum of the two terms in Eq. 3.5 vanishes and the equipartition of the total lepton asymmetry among the three neutrino flavors is quickly achieved, even for $\sin^2\theta_{13} \lesssim 0.01$, unless of course θ_{13} is extremely small. Finally, for negligible θ_{13} flavor oscillations are not effective until $T \lesssim 3$ MeV (outer lines in Fig. 3.2), a value that can be found putting Δm^2_{31} in Eq. 3.5.

As mentioned, the moment when flavor oscillations become effective de-

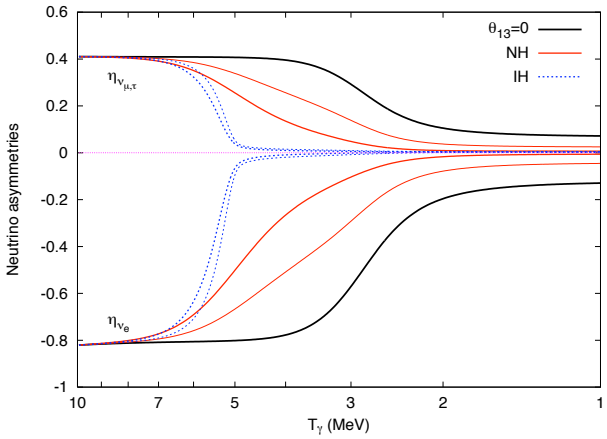

Figure 3.2: Evolution of the flavor neutrino asymmetries when $\eta_{\nu_e}^{\rm in} = -0.82$ and zero total asymmetry. The outer solid curves correspond to vanishing θ_{13} (black lines), while the inner ones (red lines) were calculated in the NH for two values of $\sin^2\theta_{13}$: from left to right, 0.04 and 0.02. The same two values of $\sin^2\theta_{13}$ apply to the cases shown as blue dotted lines, but in the IH.

termines also how much time do weak interactions have to drive the averaged distributions made by mixing to the equilibrium one (the sooner – the better). The smaller the mixing angle θ_{13} is, the spectra are more off-equilibrium, with degeneracy paramters not well defined and the increase of their contribution to total energy budget with respect to the equilibrium value.

A way to see the role of flavor oscillations on the reduction of the final value of $N_{\rm eff}$ from neutrino asymmetries is given in Figure 3.3. Here we have fixed the initial electron neutrino asymmetry to $\eta_{\nu_e}^{\rm in} = -0.82$ as in Figure 3.2, but varied the total asymmetry in the range $-0.8 \leq \eta_\nu \leq 0.8$. In the absence of neutrino mixing the final value of $N_{\rm eff}$ is that given by Eq. 3.2, directly related to the chemical potentials, and for this particular range it can be as large as $N_{\rm eff} \simeq 4.6$. Instead, when oscillations are included the three flavor asymmetries are modified and the contribution of neutrinos is largely reduced, even for $\theta_{13} = 0$. Finally, for $\sin^2\theta_{13} = 0.04$ and both NH or IH, the final flavor asymmetries are given by $\eta_{\nu_\alpha} \simeq \eta_\nu/3$. In such a case, we expect neutrinos to almost follow Fermi-Dirac spectra and $N_{\rm eff}$ as given in Eq. 3.2. For instance, for $\eta_\nu = 0.8$ one expects $\xi_{\nu_{e,\mu,\tau}} \simeq 0.38$ and a total contribution to the radiation energy density of $N_{\rm eff} \simeq 3.19$, very close to what we find in our numerical calculations for $\sin^2\theta_{13} = 0.04$, while we found $N_{\rm eff} \simeq 3.43$ for $\theta_{13} = 0$.

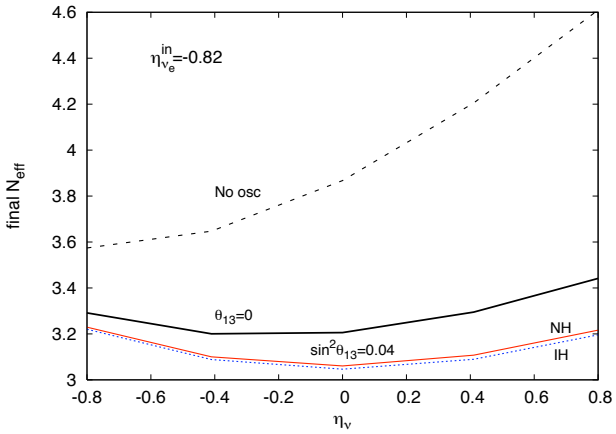

Figure 3.3: Final contribution of neutrinos to the total radiation energy density, parametrized with $N_{\rm eff}$, as a function of the total neutrino asymmetry for a particular value of the initial electron neutrino asymmetry ($\eta^{\rm in}_{\nu_e} = -0.82$). From top to bottom, the various lines correspond, respectively, to the following cases: no neutrino oscillations (η_{ν_e} conserved), $\theta_{13} = 0$, and $\sin^2\theta_{13} = 0.04$ for normal (red solid line) and inverted (blue dotted line) neutrino mass hierarchy.

3.2 Results

Differently than in the previous treatments, where both neutrino asymmetries and the corrisponding $N_{\rm eff}$ were considered as constant parameters, in the analysis presented here we have exactly followed the evolution of the neutrino distribution versus the photon temperature T_γ, which is our evolution parameter. We have changed the public numerical code so that for any given initial values (at $T_\gamma = 10$ MeV) for the total neutrino asymmetry $\eta_\nu = \sum_\alpha \eta_{\nu_\alpha}$, unchanged by flavor oscillations, and electron neutrino asymmetry $\eta^{\rm in}_{\nu_e}$ we obtain the time dependent neutrino distributions, as described in the previous section. The latter are then fitted in terms of Fermi-Dirac functions with the two evolving parameters $T_{\nu_\alpha}(T_\gamma)$ and $\xi_{\nu_\alpha}(T_\gamma)$. Weak rates are then averaged over the corresponding electron (anti)neutrino distribution. The Hubble parameter is also modified to account for the actual evolution of total neutrino energy density. In this way the final abundances of both the ratio ^{2}H/H and the ^{4}He mass fraction, Y_p, are numerically computed as a function of the input parameters η_ν and $\eta^{\rm in}_{\nu_e}$ and compared with the corresponding experimental determinations. We have used the values of Ref. [Iocco 2009], Eqs. 2.25 and 2.24, and Ref. [Aver 2010], Eq. 2.30. While their uncertainties on Y_p are the same, they differ for the central value, actually the smaller and higher of all results

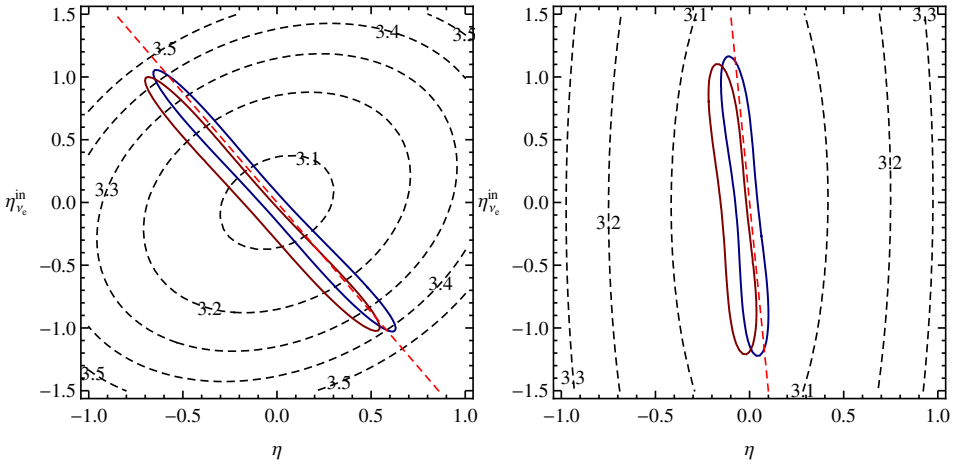

Figure 3.4: The 95% C.L. contours from our BBN analysis in the $\eta_\nu - \eta^{\rm in}_{\nu_e}$ plane for $\theta_{13} = 0$ (left) and $\sin^2\theta_{13} = 0.04$ (right). The two contours correspond to the different choices for the primordial ^{4}He abundances of Eqs. 2.25 (blue) and 2.30 (purple). The (red) dot-dashed line is the set of values of η_ν and $\eta^{\rm in}_{\nu_e}$ which, due to flavor oscillations, evolve towards a vanishing final value of electron neutrino asymmetry $\eta^{\rm fin}_{\nu_e}$. We also report as dashed lines the iso-contours for different values of $N_{\rm eff}$, the effective number of neutrinos after e^+e^- annihilation stage.

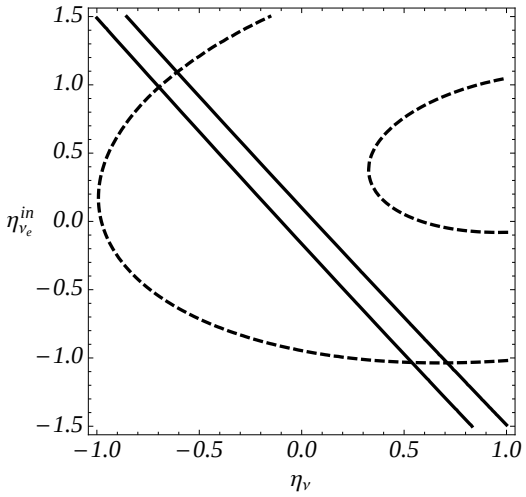

Figure 3.5: Bounds in the $\eta^{\rm in}_{\nu_e}$ - η_ν plane for each nuclear yield. Areas between the lines correspond to 95% C.L. regions singled out by the ^{4}He mass fraction (solid lines) of Eq. 2.25, and deuterium (dashed lines) as in Eq. 2.24.

reported in Chapter 2, a fact which will produce two different bounds on the electron neutrino asymmetry.

3.2.1 Constraints on the asymmetries

Typical outcomes from the analysis described is shown in Fig. 3.4 with the 95% C.L. contours for the total asymmetry η_ν and the initial value of the electron neutrino parameter $\eta^{\rm in}_{\nu_e}$ for the adopted determinations of ^{2}H and ^{4}He and for two different choices of θ_{13}. In both cases the contours are close to and aligned along the red dot-dashed line which represents the set of initial values for the asymmetries which eventually evolve toward a vanishing final electron neutrino asymmetry, $\eta^{\rm fin}_{\nu_e} \simeq 0$, which is preferred by ^{4}He data. We recall that ^{4}He is strongly changed if neutron/proton chemical equilibrium is shifted by a large value of $\nu_e - \bar{\nu}_e$ asymmetry around the freezing of weak rates ($T_\gamma \sim 0.8$ MeV). For large θ_{13}, oscillations efficiently mix all neutrino flavors and at BBN $\eta_{\nu_\alpha} \sim \eta_\nu/3$, so the bounds on η_ν are quite stringent. For a vanishing θ_{13} the contours for η_ν and $\eta^{\rm in}_{\nu_e}$ show a clear anticorrelation, and even values of order unity for both parameters are still compatible with BBN. It worth remembering, however, that this value of θ_{13} is currently in conflict with the results from long baseline experiments.

We stress that for any value of θ_{13} the data on primordial deuterium is crucial for closing the allowed region that the ^{4}He bound fixes along the $\eta^{\rm fin}_{\nu_e} \simeq 0$ line. In fact, though ^{2}H is less sensitive than ^{4}He to neutrino asymmetries and effective temperature which enter the Universe expansion rate, see e.g. [Iocco 2009], yet including it in the analysis breaks the degeneracy between $\eta^{\rm in}_{\nu_e}$ and η_ν which is present when only ^{4}He is used. This can be read from Figure 3.5 where the 95% C.L. in the $\eta^{\rm in}_{\nu_e}$ - η_ν plane are shown for ^{4}He and ^{2}H separately, for the case $\theta_{13} = 0$. The solid lines bound the region of the plane compatible with the ^{4}He measurement, whereas the dashed contours correspond to deuterium observation. The different shape of these two regions is due to the different dependence of nuclide abundances on $\eta^{\rm in}_{\nu_e}$ and η_ν, thus their combination breaks the degeneracy and closes the contour.

The main outcome of our BBN analysis is summarized in Figure 3.6 for the adopted determinations of ^{2}H and ^{4}He. From this plot one can easily see the effect of flavor oscillations on the BBN constraints on the total neutrino asymmetry. In the absence of neutrino mixing the value of η_{ν_e} is severely constrained by ^{4}He data, arising from a narrow region for the electron neutrino degeneracy, $-0.018 \leq \xi_e \leq 0.008$ at 68% C.L. Instead, the asymmetry for other neutrino flavors could be much larger, since the absolute value of total asymmetry is only restricted to the region $|\eta_\nu| \lesssim 2.6$ [Hansen 2002]. As we have previously seen, flavor oscillations modify this picture and an initially

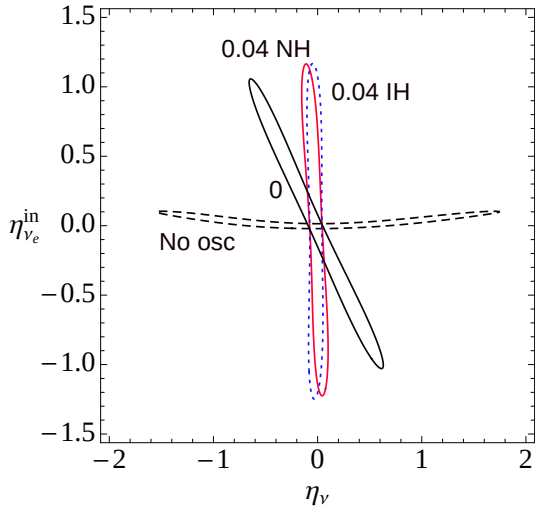

Figure 3.6: 95% C.L. contours from our BBN analysis in the $\eta_\nu - \eta^{\rm in}_{\nu_e}$ plane for several values of $\sin^2\theta_{13}$: 0 (black solid line), 0.04 and NH (red solid line), 0.04 and IH (blue dotted line). The case of no neutrino flavor oscillations is shown for comparison as the black dashed contour.

large $\eta^{\rm in}_{\nu_e}$ can be compensated by an asymmetry in the other flavors with opposite sign. The most restrictive BBN bound on η_{ν_e} applies then to the total asymmetry, an effect that visible Figure 3.6 as a *rotation* of the allowed region from a quasi-horizontal one for zero mixing to an almost vertical region for $\sin^2\theta_{13} = 0.04$, in particular for the IH. In all cases depicted in Figure 3.6 the allowed values of the asymmetries are mainly fixed by the ^{4}He bound, which imposes that the value of η_{ν_e} at BBN must be very close to zero, while the data on primordial deuterium is crucial for closing the region.

For values of θ_{13} close to the upper limits set by experimental data, the combined effect of oscillations and collisions leads to an efficient mixing of all neutrino flavors before BBN. Therefore, the individual neutrino asymmetries have similar values, approximately $\eta_{\nu_\alpha} \simeq \eta_\nu/3$, and the BBN bound on the electron neutrino asymmetry applies to all flavors, and in turn to η_ν as considered in previous analyses [Iocco 2009, Barger 2003b, Barger 2003a, Cuoco 2004, Cyburt 2005, Serpico 2005, Simha 2008]. We find that for $\sin^2\theta_{13} = 0.04$ the allowed region at 95% C.L. is $-0.17(-0.1) \leq \eta_\nu \leq 0.1(0.05)$ for neutrino masses following a normal (inverted) mass hierarchy. Note, however, that in the IH this result approximately holds for any value of $\sin^2\theta_{13}$ within the favoured region by oscilation data, due to the resonant character of the conversions. Instead, as discussed in [Mangano 2011a], in the NH even values of order $|\eta_\nu| \simeq 0.6$ are still compatible with BBN if θ_{13} is very small.

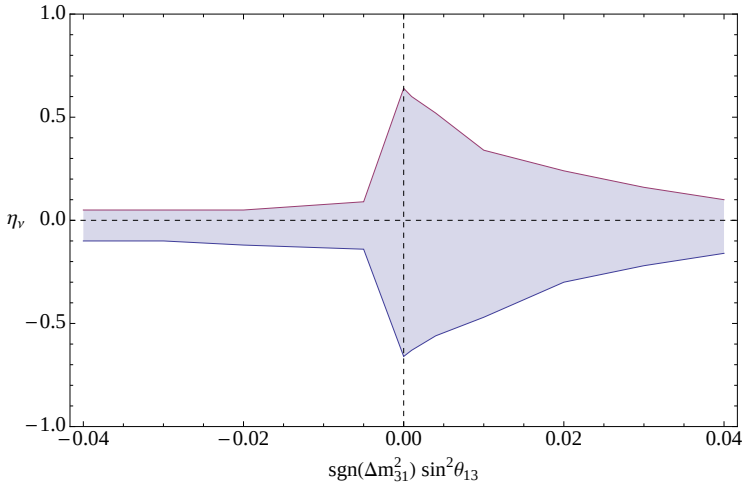

Figure 3.7: The shadowed region corresponds to the values of the total neutrino asymmetry compatible with BBN at 95% C.L., in function of θ_{13} and the neutrino mass hierarchy.

The allowed regions of the total neutrino asymmetry are depicted in Fig. 3.7 in function of the mixing angle θ_{13} and the mass hierarchy.

The analysis presented can be recasted into constrains on the initial flavor degeneracy parameters $\xi^{\rm in}_{\nu_e}$ and $\xi^{\rm in}_{\nu_x}$ as in Fig. 3.8. We found also interesting to consider a new pair of variables: the electron neutrino asymmetry at the onset of BBN $\eta^{\rm fin}_{\nu_e}$, and the difference $\eta^{\rm fin}_{\nu_x} - \eta^{\rm fin}_{\nu_e}$, which in the standard analysis is usually assumed to be vanishing. One can see from this figure that, while the (95% C.L.) bound on $\eta^{\rm fin}_{\nu_e}$ is independent of the value of θ_{13}, the difference between the final ν_e and ν_x asymmetries strongly depends upon this yet unknown mixing angle, as expected. In fact, for large θ_{13} we recover the standard result, $\eta^{\rm fin}_{\nu_x} \sim \eta^{\rm fin}_{\nu_e}$, due to efficient mixing by oscillations and collisions, while for $\theta_{13} = 0$ the two asymmetries can be different.

3.2.2 Constraints on the effective number of neutrinos

In Figures 3.4, 3.8 and 3.9 we also plot iso-contours for the value of the effective number of neutrinos, $N_{\rm eff}$, evaluated after e^+e^- annihilations. For large θ_{13} (right-hand panels of the reported figures) BBN data bound $N_{\rm eff}$ to be very close to the standard value 3.046, since all asymmetries should be very small in this case and flavor oscillations modify the neutrino distributions while neutrinos are still strongly coupled to the electromagnetic bath. Therefore, we do not expect non-thermal features in the neutrino spectra in this case, since scatterings and pair processes allow for an efficient transfer of any entropy

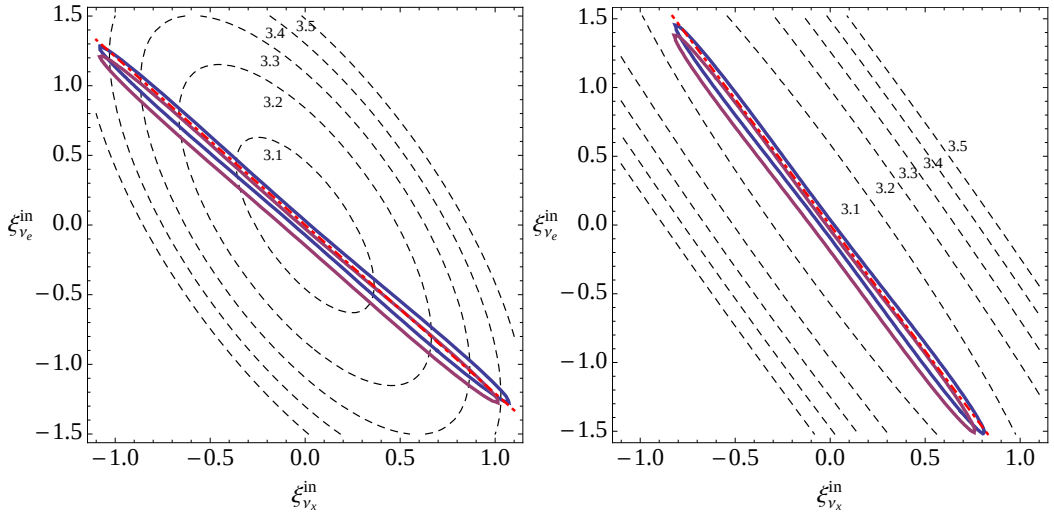

Figure 3.8: Same results as in Figure 3.4 in the plane of initial flavor degeneracy parameters $\xi^{\rm in}_{\nu_x}$ and $\xi^{\rm in}_{\nu_e}$.

excess. On the other hand, for vanishing θ_{13} (left-hand panels of the reported figures), larger values of $N_{\rm eff}$ are still compatible with BBN data, up to values of the order of 3.4 at 95% C.L. The dependence of the largest possible value of $N_{\rm eff}$ on the value of the mixing angle θ_{13}, obtained by spanning in the asymmetry parameter plane the region compatible with BBN, is reported in Fig. 3.10.

It is worth noticing that the final values of $N_{\rm eff}$, in particular for large final asymmetries of ν_x, are also slightly larger than the $N_{\rm eff}$ that one would obtain using the equilibrium expression of Eq. 2.7. For example, if we take $\eta^{\rm fin}_{\nu_e} = 0$ and $\eta^{\rm fin}_{\nu_x} = 0.3$, a point on the boundary of the BBN contours (see Fig. 3.9) and compute the corresponding effective chemical potentials, using Eq. 3.2 one gets $N_{\rm eff} = 3.2$, while the actual value is larger, $N_{\rm eff} = 3.4$, a signal that in this case the interplay of solar-like oscillations and neutrino freeze-out has produced indeed, a mild non-thermal distortion in neutrino distributions.

We notice that our BBN results correspond to a minimal scenario with primordial neutrino asymmetries, as we do not consider a possible extra contribution to $N_{\rm eff}$ coming from relativistic degrees of freedom other than standard active neutrinos. Their effect is known to produce looser bounds on neutrino asymmetries, as they speed up expansion and thus, can compensate the effect of a positive $\nu_e - \bar{\nu}_e$ asymmetry. We have explicitly checked that, for some choices of primordial asymmetries, the addition of extra radiation does not modify the evolution of flavor neutrino asymmetries. Of course, in such a case the contribution to the energy density of the additional relativistic de-

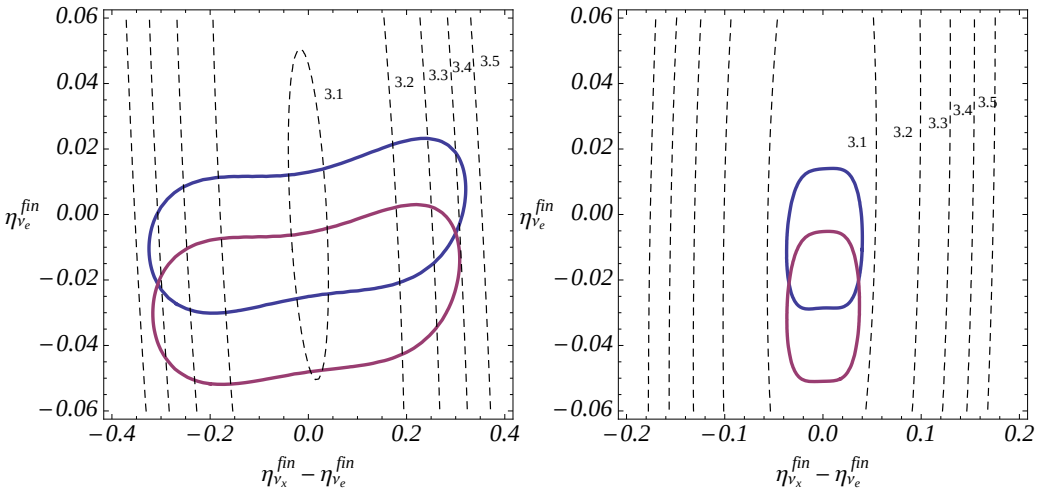

Figure 3.9: Same results as in Fig. 3.4 in the plane of $\eta^{\rm fin}_{\nu_e}$ and the difference $\eta^{\rm fin}_{\nu_x} - \eta^{\rm fin}_{\nu_x}$, where the superscript indicates that the asymmetries are evaluated at the onset of BBN, $T_\gamma \sim 1$ MeV, after flavor oscillations shuffled the initial $\eta^{\rm in}_{\nu_\alpha}$.

grees of freedom adds up to the surviving excess to $N_{\rm eff}$ arising from neutrino asymmetries.

The complete dependence of the largest possible value of $N_{\rm eff}$ from neutrino asymmetries in the region compatible with BBN, as a function of the neutrino mass hierarchy and the mixing angle θ_{13} is reported in Figure 3.10. If the true value of θ_{13} lies in the upper part of the region favoured by oscillation experiments (in particular T2K) or $\Delta m^2_{31} < 0$, the presence of primordial asymmetries can not lead to a contribution to the radiation energy density $N_{\rm eff} > 3.1$. On the other hand, for the NH and very small values of θ_{13}, larger values of $N_{\rm eff}$ are still compatible with BBN data, up to 3.43 at 95% C.L.

3.3 Summary

We have found the BBN constraints on the cosmological lepton number and its associated contribution to the radiation energy density, taking into account the effect of flavor neutrino oscillations. Once the other neutrino mixing parameters have been fixed by oscillation data, we have shown that pinpointing the value of θ_{13} is crucial to establish the degree of conversion of flavor neutrino asymmetries in the early Universe.

The most stringent BBN bound on the total neutrino asymmetry, $|\eta_\nu| \lesssim 0.1$, requires that reactor neutrino experiments in the near future, such as

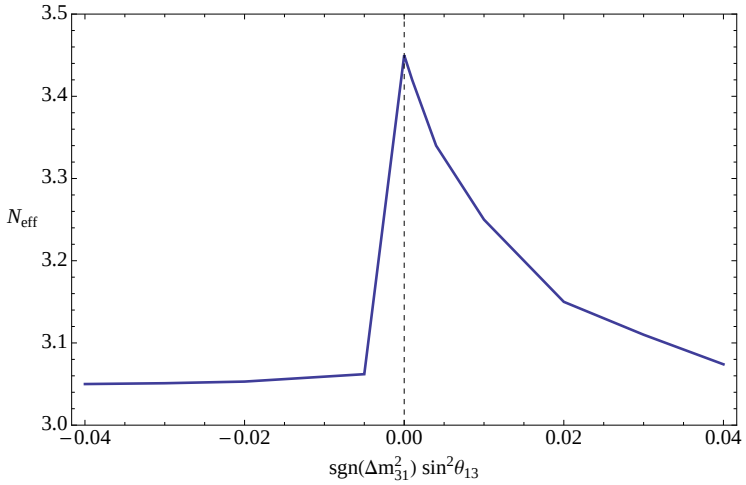

Figure 3.10: Largest values of $N_{\rm eff}$ from primordial neutrino asymmetries compatible with BBN at 95% C.L., as a function of θ_{13} and the neutrino mass hierarchy.

Double Chooz, Daya Bay or Reno, confirm that the value of the third neutrino mixing angle is such that $\sin^2\theta_{13} \gtrsim 0.03$, the central value of the T2K analysis. This conclusion also applies to the whole allowed range of θ_{13} values at 3σ if neutrino masses follow an inverted hierarchy scheme.

Similarly, a measured value $\sin^2\theta_{13} \gtrsim 0.03$ will imply that the maximum contribution of neutrino asymmetries to the radiation content of the Universe can not exceed $N_{\rm eff} \simeq 3.1$, well below the expected sensitivity of the Planck satellite (0.4 at 2σ) [Hamann 2008, Bowen 2002], whose first data release on the anisotropies of the cosmic microwave background (CMB) is expected in one year or so.

Finally, BBN remains the best way to constrain a potential cosmological lepton number, despite the present precision of the measurements of the CMB anisotropies and other late cosmological observables. Bounds on the neutrino asymmetries with these data do not improve those found in our work, but are of course sensitive to other neutrino properties such as their masses.

Chapter 4

Role of neutrinos in supernova dynamics

Historical astronomical classification of supernovae was based purely on the properties of their spectra, such as the presence (Type I) or absence (Type II) of hydrogen lines (see Table 4). According to the present-day theory of stellar evolution, only one type, SN Ia, have different nature then the others: they originate from a white dwarf in a binary system that accretes material from the companion star. Once its mass reaches the Chandarsekhar limit ($M_{\mathrm{Ch}} \approx 1.44 M_{\odot}$), it implodes, triggering the thermonuclear reactions and an explosion of energy carried mostly by the photons. During the explosion all the material of a star is blown away and no compact remnant remains. Because if the same mechanism and precise conditions, all Type Ia supernovae have similar spectra and luminosities which can be calculated. This property makes them the best standard candles in astronomy.

All other types of supernovae are core-collapse supernovae. They are triggered by an implosion of an inner iron core of a massive star, which turns to an explosion that expels the outer layers into space, creating a planetary nebula typically with a pulsar in its center. Core-collapse supernovae are one of the most energetic phenomena in the Universe: one single explosion is capable outshining an entire galaxy made out of billions of stars. Yet, the light amounts to less than one percent of its energy content — all the rest is emitted in the form of neutrinos. Therefore, neutrinos coming from a core-collapse supernova could provide valuable information about the extreme environment such as the supernova core, where the matter is at nuclear densities and energies of the order of 10 MeV. Understanding if the evolution of neutrinos from a supernova core to present detectors on Earth has been a subject of interest in the recent years.

4.1 Physics of core collapse supernovae

4.1.1 Mechanism

By the end if its hydrostatic burning, a massive star has the famous onion-like structure, with shells that are relics of all the previous burning phases

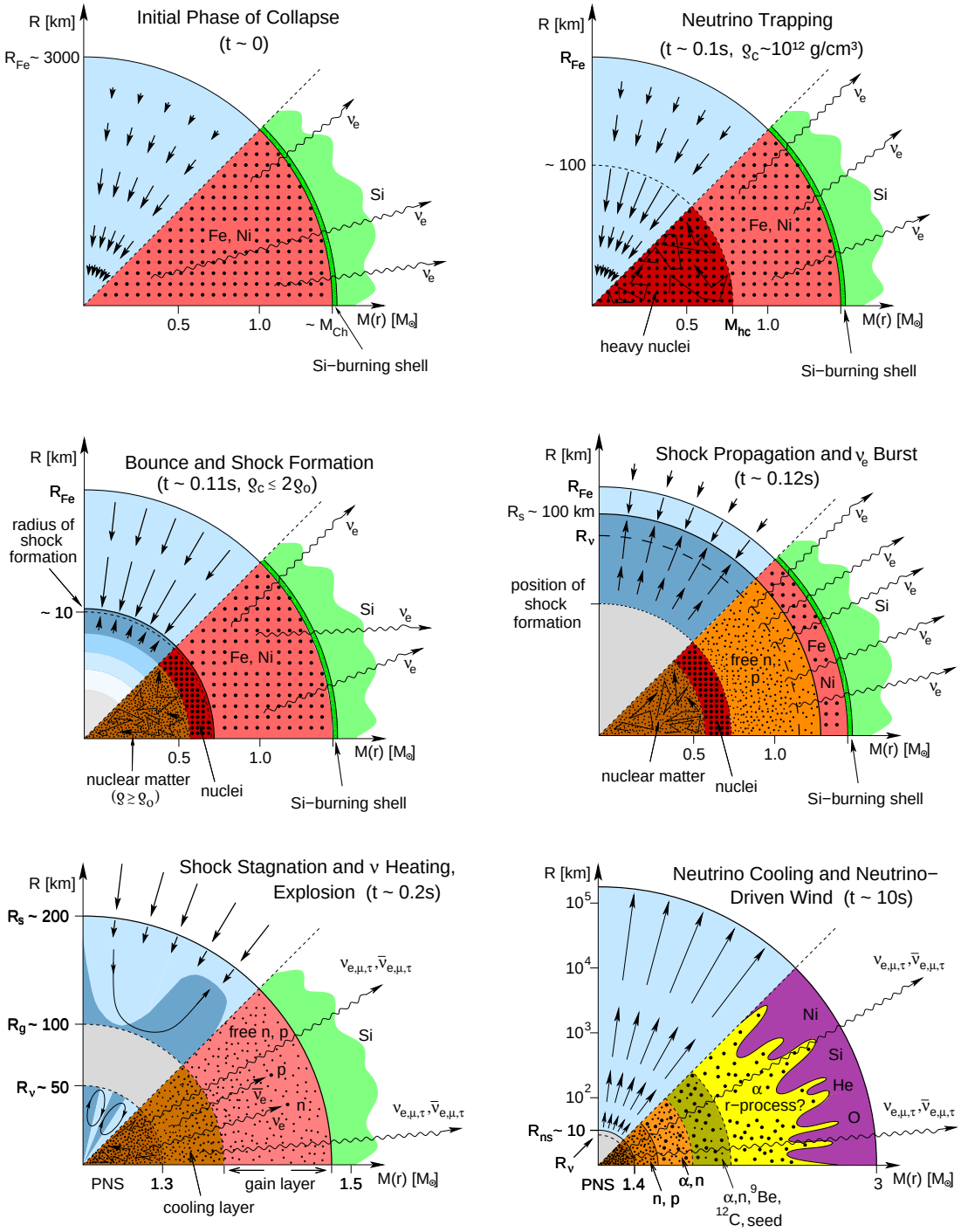

Figure 4.1: Schematic representation of the evolutionary stages of a core collapse SN. The panels display the dynamical conditions in their upper half, with arrows representing velocity vectors. The nuclear composition as well as the nuclear and weak processes are indicated in the lower half of each panel. The horizontal axis gives mass information. $M_{\rm Ch}$ means the Chandrasekhar mass and $M_{\rm hc}$ the mass of the subsonically collapsing, homologous inner core. The vertical axis shows the corresponding radii, with $R_{\rm Fe}$, $R_{\rm s}$, $R_{\rm g}$, $R_{\rm ns}$, and R_ν being the iron core radius, shock radius, gain radius, neutron star radius, and neutrinosphere, respectively. Figure taken from [Janka 2007].

Table 4.1: Classification of supernovae

Spectral Type	Ia	Ib	Ic	II
Spectrum	No Hydrogen			Hydrogen
	Silicon	No Silicon		
		Helium	No Helium	
Physical Mechanism	Nuclear explosion of low-mass star	Core collapse of evolved massive star (may have lost its hydrogen or even helium envelope during red-giant evolution)		
Light Curve	Reproducible	Large variations		
Neutrinos	Insignificant	~ 100 × Visible energy		
Compact Remnant	None	Neutron star (typically appears as pulsar) Sometimes black hole ?		

(hydrogen, helium, carbon, neon, oxygen and silicon). In the final stage iron is synthesized, as the most stable nucleus in the Universe. When the mass of the iron core reaches the Chandarsekhar limit, the electron degeneracy pressure cannot withstand anymore the gravitational potential and the core collapses. The important phase of the explosion that follows are given in Fig. 4.1:

1) In the first phase of the collapse, the electrons are captured on nuclei and transformed into electron neutrinos (via weak reactions $e^- p \rightarrow n \nu_e$), which escape freely. This reduction of electron density increases the compressibility of the core (it takes less gravitational energy to reduce the volume), accelerating the collapse further. In the process, it also shifts the neutron-to-proton ratio towards more neutron rich material.

2) When the core reaches the density $\rho_{\rm trap} = 10^{12}{\rm g/cm}^3$, neutrinos are not free to stream out from the core because their diffusion time due to scattering on nuclei becomes larger than the collapse time. Neutrinos are trapped. As a consequence, inside the core, the β-equilibrium is reached and the Fermi sea of neutrinos builds up.

3) The inner part of the core continues the collapse at subsonic speed, with all its parts in causal contact. Once it reaches nuclear densities, with much lower compressibility, the inner core decelerates and bounces back, forming a shockwave. In the mean time, the outer parts of the core are pulled to the center at supersonic speeds and do not decelerate as the homologous core. Instead, the shockwave propagates through the

infalling material of the outer core and other layers forming an environment in which heavier nuclei can be formed (r-process nucleosynthesis) and eventually expels all out in the interstellar medium.

However, the exact scenario and crucial physical arguments of this appealing and simple *prompt mechanism* of SN explosions are still uncertain and under investigation. Present state-of-the-art simulations suggest that the energy available for the shock is not sufficient to drive the explosion [Buras 2003].

4) Shock eats up its own energy in the outer layer by dissociation of heavy nuclei into free nucleons. Since electron capture rate on free protons is significantly larger then on heavier neutron rich nuclei, a neutronization phase that follows transforms almost all electrons in neutrinos, which then carry the energy away. This neutronization (deleptonization) burst happens mostly outside the inner core and since these neutrinos can free-stream through matter they carry away the lepton number.

5) The shock is weakened so much that it stalls at a radius $r \sim 100 - 200$ km and turns into an accretion shock, with the matter from outer layers still infalling. In the center, the core accretes the surrounding material and a proto-neutron star (PNS) is formed. The PNS will later become a neutron star, or a black hole if its mass is greater than $25 M_{\odot}$. The hot PNS is subsequently cooled by the emission neutrinos, which had lost a part of their energy while drifting through the nuclear material, and therefore exit the PNS with energies $E \sim 10 - 20$ MeV. The sphere at which the environment becomes transparent for neutrinos is called the neutrinosphere. During the cooling, neutrinos will carry away 99% of the total energy of the collapse.

6) On their way out, neutrinos can deposit energy while going through the shockwave and revive it in the *delayed explosion* scenario. This energy deposition is of course flavor discriminating with electron flavor capable of depositing more energy. It has been estimated that if $10-20\%$ energy radiated in the form of electron neutrinos is converted to thermal energy of nucleons and leptons in the gain layer, the shock can be re-energized to make a supernova.[1] The heated material expands and a hot bubble region of matter at lower densities and high temperatures is formed between the shock-wave front and the surface of the PNS. The persisting pressure of neutrinos restarts the explosion and, at the same time, the neutrinosphere radius decreases down to $R_{\nu} \sim 10$ km.

[1] In the perspective of possible flavor and spectral swaps (see Sec. 4.3.2), this feature will prove to be very important for SN simulations.

The first considerations of core collapse supernova dynamics already pointed that the hot bubble region should be convectively unstable. The neutrino heating in the gain radius closer to the PNS is much more effective than at larger distances. The matter at low entropy and higher density outside the shock region can penetrate the hot bubble, get heated close to PNS and expelled again causing the large scale convective motion. Indeed multidimenstional (2D and 3D) hydrodynamic simulations confirmed this expectations. They have also discovered a generic instability of the system to non-radial deformations [Blondin 2003]. This standing accretion shock instability (SASI) causes a bipolar (and quadrupolar) sloshing of the shock with large pulsational expansions and contractions. The turbulent motion caused by it significantly enhances the neutrino heating and thus indirectly helps the shock expansion. As the presence of SASI changes the geometry of the system, it is believed to be the origin of typically asymmetric nebulae born in a SN explosion. A dominant monopole mode can lead to a large recoil of the newly born neutron star and provide a mechanism for pulsar kicks and an unstable $l = 1, m = 1$ SASI mode can create strong rotational flow close to PNS and explain pulsar spins.

Despite the discovery of SASI and the general progress in the area of SN simulation, no selfconsistent explosion for a model of progenitor mass larger than about $12M_{\odot}$ has been observed [Buras 2003]. For each of them one would have to intervene by hand raising the obtained neutrino luminosities to trigger the explosion and it seems at present that a piece of physics is missing. One of the directions in this search for the missing puzzle points toward the physics of neutrinos. In general, SN simulations are performed without neutrinos oscillations. However, if significant neutrino flavor evolution happens between the PNS and the shock, it would have to be included in the simulations. On the contrary, if one could prove that in that region no flavor conversions happen, it would be a consistency check for simulations; it would mean it is not necessary to include the neutrino oscillations in the codes and that the missing physics should be searched for elsewhere.

4.1.2 Neutrinos from supernovae

A simple estimate of the number of neutrinos can be made upon general arguments: Virial theorem states that the average kinetic energy for a non-relativistic particle is half of its potential energy. For a nucleon on the surface of the neutron start it is

$$\langle E_{\rm kin} \rangle = \frac{1}{2} \frac{G_{\rm N}\, M_{\rm ns} m_N}{R_{\rm ns}} \simeq 25 \text{ MeV} \ , \tag{4.1}$$

where m_N is the nucleon mass, G_N is the Newton constant, $M_\mathrm{ns} = 1.5 M_\odot$ is the typical mass of the (proto-)neutron star, and $R_\mathrm{ns} = 15$ km is its typical diameter. For a few seconds, neutrinos are in equilibrium with the nucleons in the PNS, so they share the same kinetic energy of $\mathcal{O}(10)$ MeV. The gravitational binding energy is roughly

$$\frac{G_\mathrm{N}\, M_\mathrm{ns}^2}{R_\mathrm{ns}} \sim 10^{57}\ \mathrm{GeV}\ , \tag{4.2}$$

and it is almost all carried by neutrinos. Dividing by the number of families and the typical energies, we arrive to striking 10^{58} neutrinos per family! About 10% of them are emitted in the initial deleptonization burst and the rest in the cooling phase on a second time scale.

Many effects, known and speculative, leave an imprint on neutrinos on their way from the SN core to detectors on Earth. SASI instabilities, neutrino self-interaction, MSW conversions, Earth-matter effects, possible non-standard interactions, etc. could answer some questions on fundamental physics and the mechanism of SN explosion. Therefore, a detection of high-statistics-SN-neutrino signal is goal of the present day SN neutrino physics. A typical SN at a typical galactic distance of 10 kpc would leave $\mathcal{O}(10^4)$ events in the largest existing low-energy neutrino detector (32 kton mass) Super-Kamiokande [Super-K]. Other terrestrial experiments would also detect neutrinos from a typical galactic SN – SNO (about 400 events), KamLAND (300), LVD (200), MiniBooNE (200), Icarus (200), Borexino (100), Baksan (100) [Scholberg 2007]. The biggest detector on Earth, the 2.5 Mton IceCube on South pole, is not optimized for detection of such low-energy neutrinos, but a systematic increase of background noise would correspond to $\mathcal{O}(10^6)$ of events and would allow us to see the "neutrino light curve" with the possible imprints of SASI [Lund 2010].

With this network of detectors, we would be capable of pinpointing the coordinates of the supernova within few degrees precision [SNEWS]. Since the photons due to their electromagnetic interaction are typically trapped in the accreting material, first light appears hours after neutrinos, which would give time for the community to observe the most energetic phenomena in the Universe with all possible resources.

In the core itself and after the emission, muon and tau neutrinos and antineutrinos share the same physics. They are produced at the same rates, with the same average energies well below the threshold for the production of μ and τ leptons, their luminosities are same, and they interact only via neutral current and therefore feel the same potential. For this reason, in the context of supernova physics, mu and tau neutrinos and antineutrinos are usually referred as unique non-electron flavor ν_x. On the other hand, the distinction

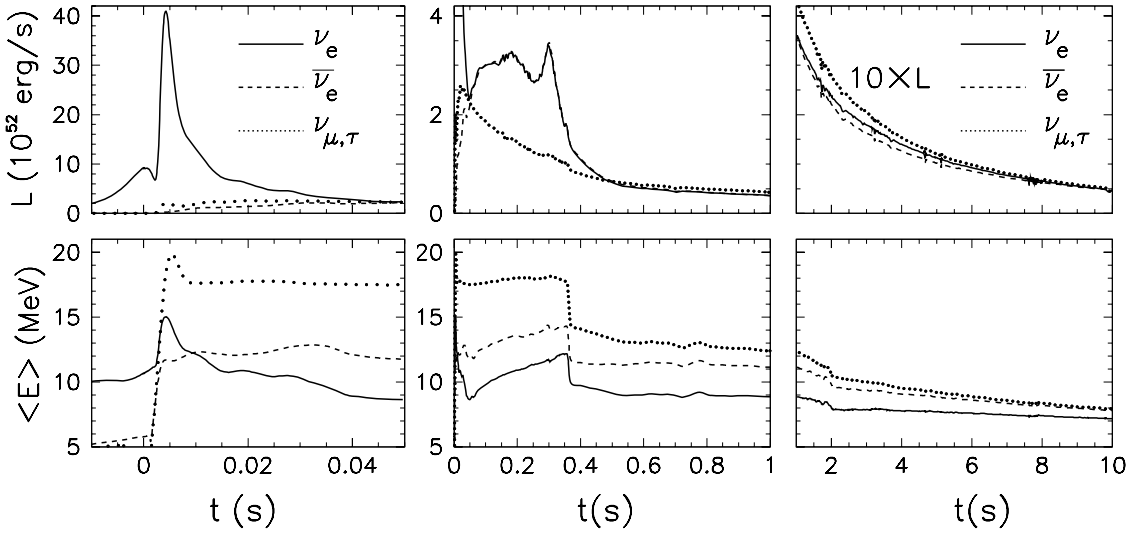

Figure 4.2: Neutrino signal of a core-collapse SN for a 10.8 $M_\odot$ progenitor according to a numerical simulation of the Basel group [Fischer 2010]. All quantities are in the laboratory frame of a distant observer. In this spherically symmetric simulation the explosion was triggered by hand. *Left*: Prompt neutrino burst. *Middle*: Accretion phase. *Right*: Cooling phase. Plot taken from [Wurm 2011].

between electron neutrinos and antineutrinos has to be made, mostly because of the deleptonization of material in the core and around which results in the large chemical potential of electron neutrinos.

Neutrino spectra are formed as they diffuse from the core outwards. Due to decreasing density, at some point the reactions become inefficient that defines the neutrinosphere. In general, however, different species interact with different rates and have different neutrinospheres. The sooner they decouple, the less time they have to scatter down in the momentum space and hence are emitted with higher local average energies. Non-electron neutrinos react only through neutral current and are the first to decouple with energies $E_{\nu_x} \sim 24-27$ MeV. Electron neutrinos and antineutrinos are both affected by β reactions. The proto-neutron star, however, contains more neutrons than protons, which leads to a higher absorption rate for ν_e's than for $\bar{\nu}_e$'s. Therefore, the ν_e sphere lies at a larger radius than the $\bar{\nu}_e$ sphere, so the mean energy of emitted ν_e, $E_{\nu_e} \sim 10-12$ MeV, is always less than the mean energy of $\bar{\nu}_e$, $E_{\bar{\nu}_e} \sim 14-17$ MeV. This reflects in the usual flux hierarchy $F_{\nu_e} > F_{\bar{\nu}_e} > F_{\nu_x}$.

An example of a neutrino light-curve us given in Figure 4.2. The three phases (deleptonization burst, accretion and cooling) are clearly separated.

These luminosities are obtained from a spherically symmetric simulation in which the explosion was triggered by hand. That explains the peak in the ν_e luminosities during the accretion phase.

4.2 Flavor evolution of neutrino fluxes

In order to interpret the future neutrino signal from a supernova, we have to account for all the possible effects neutrinos could have suffered on their way from the core to detectors. First of all, there are the collective conversions in the region close to the supernova. Then, in the outer envelope, the MSW conversions take place, at densities $\rho \sim 10^3 - 10^4$ g/cm^3 for the atmospheric and at $\rho \sim 10 - 100$ g/cm^3 for the solar parameters. After that the mass eigentstates of neutrinos travel independently and if the detector is shadowed by the Earth itself, we have to take into account again the MSW effect. Over the last decade, a plethora of possibilities have been investigated, with a solid conclusion that, if we know all the contributions, we can extract valuable information on the missing ingredient for the SN simulation, and the neutrino properties, such as the last mixing angle θ_{13} and the mass hierarchy. As the last experimental results suggest that the measurement of θ_{13} is just around the corner, the significance of supernova signal has moved to the mass hierarchy[2].

The main uncertainty in the neutrino propagation from the core are the first few hundreds of kilometers, where the neutrinos are largely influenced by their own refractive effects. Any definitive answer on how this region influences the spectra is crucial for understanding the next SN-neutrino signal.

4.2.1 Spatial evolution in spherical symmetry

Once they are emitted from the core, neutrinos free-stream, so no collisions or any momentum changing processes are present, unlike in the early Universe. In Chapter 1, a general equation for matrices of occupation numbers is developed for this situation

$$\mathrm{i}\partial_t \varrho_{\mathbf{p}} = [\mathsf{H}_{\mathbf{p}}, \varrho_{\mathbf{p}}] \quad \text{and} \quad \mathrm{i}\partial_t \bar{\varrho}_{\mathbf{p}} = [\bar{\mathsf{H}}_{\mathbf{p}}, \bar{\varrho}_{\mathbf{p}}] \ , \tag{4.3}$$

where the Hamiltonian for each mode is

$$\mathsf{H}_{\mathbf{p}} = \frac{\mathsf{M}}{2p} + \lambda \mathsf{L} + \sqrt{2}\, G_{\mathrm{F}} \int \frac{\mathrm{d}^3\mathbf{q}}{(2\pi)^3} \left(\varrho_{\mathbf{q}} - \bar{\varrho}_{\mathbf{q}}\right) \left(1 - \mathbf{v}_{\mathbf{q}} \cdot \mathbf{v}_{\mathbf{p}}\right) \ . \tag{4.4}$$

[2] I do not discuss here how a signal from a supernova contributes constraining other physical parameters, such as neutrino magnetic moment, electric charge or mass, or even the presence of other particles. See [Raffelt 1996] for more details.

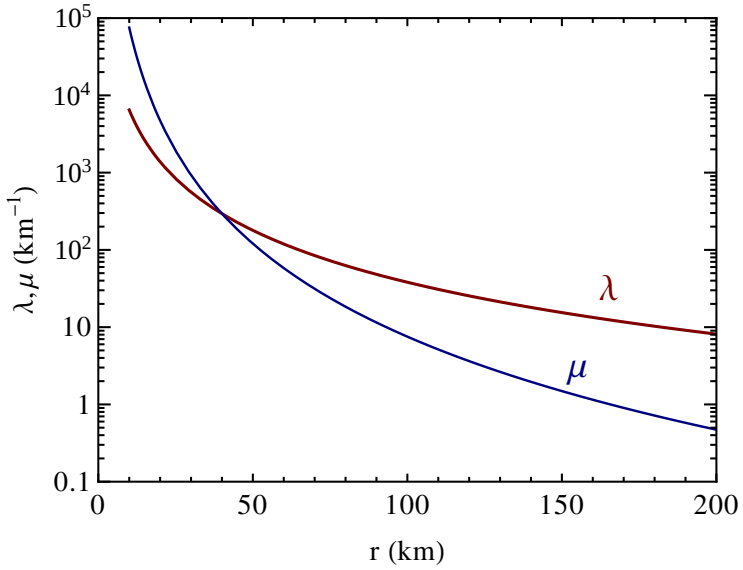

Figure 4.3: Typical radial dependence of ordinary matter potential λ and the neutrino self-coupling strength μ for a supernova in the cooling phase.

The matrix of vacuum oscillation frequencies for relativistic neutrinos is the same as Eq. 1.19. The matter effect is represented by $\lambda = \sqrt{2}\, G_{\rm F}(n_{e^-} - n_{e^+})$ and $\mathsf{L} = \mathrm{diag}(1,0,0)$, given here in the weak interaction basis. We ignore the possible presence of other charged-lepton flavors. The Hamiltonian for antineutrinos $\bar{\mathsf{H}}_{\mathbf{p}}$ is the same with $\mathsf{M} \to -\mathsf{M}$.

It is customary to reduce the system to 2 flavors, ν_e and ν_x, neglecting the solar squared-mass difference $\Delta m^2_{\odot} \ll \Delta m^2_{\rm atm}$. Therefore, for the rest of this manuscript, a generic squared-mass difference will always refer to the atmospheric one $\Delta m^2 \equiv \Delta m^2_{\rm atm}$, and a generic mixing angle $\theta = \theta_{13}$.

Figure 4.3 shows a typical radial profile of parameters relevant for neutrino evolution equations. Natural unit for distance in the supernova physics is km and expressing all the potentials in km^{-1} simplifies the formalism. Matter potential λ scales as electron density (approximately $\propto r^{-2}$), with a strong drop at the radius of the shockwave. For the case shown, the shockwave is already propagated to larger radius. Comparing the value of lambda with the typical vacuum frequency $\omega_0 = \left\langle \frac{\Delta m^2}{2E} \right\rangle \simeq 0.3$ km^{-1} we see that the well understood MSW conversions take place at 10^4 – 10^5 km away from the core, allowing us to treat them separately.

The strength of neutrino self-interaction, as usual parametrized by μ, scales as $\propto r^{-4}$, reflecting the usual radial dilution of the flux ($\propto r^{-2}$) with the other two powers coming from angular dependence of the interaction – as the neutrino rays become more collinear going further from the core, the

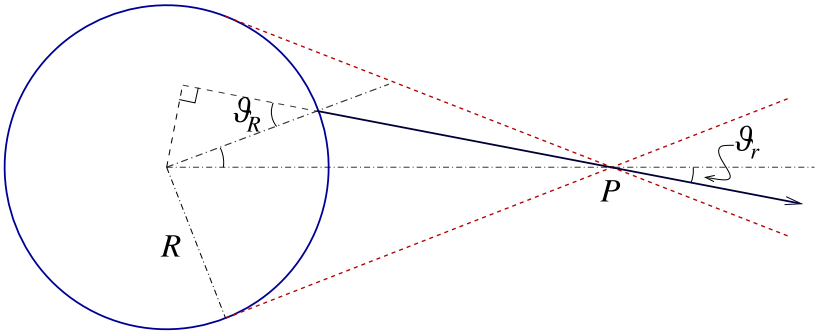

Figure 4.4: Geometry of the neutrino propagation. Figure adapted from [Duan 2006].

interaction drops for another two powers. Close to the core, where neutrino fluxes are extremely large, neutrino self-interaction dominates the evolution. During the accretion phase, the matter potential is comparable to ν–ν one, so the delicate interplay those two effects can have significant impact.

Instead of a homogeneous system that evolves in time, in the case of a supernova we consider a stationary system that evolves in space. Since neutrinos propagate at the speed of light, it is safe to consider snapshots of supernova explosion and evolve fluxes for each snapshot independently. The occupation numbers ($\varrho_{\mathbf{p}}$ matrix elements) depend both on spatial coordinates and on momenta, but there is no conceptual problem as long as we consider spatial variations that are slow on the scale of the inverse neutrino momenta.

In the Eq. 4.4 the factor $(1-\mathbf{v_q}\cdot\mathbf{v_p}) = (1-\cos\vartheta_{\mathbf{pq}})$ represents the current-current nature of the weak interaction where $\mathbf{v_p} = \mathbf{p}/p$ is the velocity. If the gas is isotropic, as in the early Universe, this term averages to 1. In general, also matter potential would have a similar term, but in the absence of net flux of matter, it is safe to neglect it. If the system is axially symmetric relative to some direction, the angular factor simplifies after an azimuthal integration to [Duan 2006, Raffelt 2007]

$$(1 - \mathbf{v_q}\cdot\mathbf{v_p}) \to (1 - v_{\mathbf{q}}v_{\mathbf{p}}) \ , \tag{4.5}$$

where the velocities are along the symmetry axis.

The multi-angle effects are crucial for understanding the evolution of neutrinos from a SN, so we cannot reduce the equations to plane waves moving in the same direction. However, we can take advantage of the global spherical symmetry, implying that the ensemble is represented by matrices that depend on a radial coordinate r, the zenith angle relative to the radial direction ϑ_R, and the energy E, which in the relativistic limit is identical to momentum $p = |\mathbf{p}|$.

A neutrino is launched from a radius R, at an angle ϑ_R relative to the radial direction (see Fig. 4.4), has a radial velocity

$$v_R = \cos\vartheta_R \ . \tag{4.6}$$

At the point P, the neutrino trajectory forms an angle ϑ_r with the radial direction, implied by simple geometry to be [Duan 2006]

$$R\sin\vartheta_R = r\sin\vartheta_r \ . \tag{4.7}$$

Therefore, the radial velocity at r is

$$v_{u,r} = \cos\vartheta_r = \sqrt{1-\frac{R^2}{r^2}\,u} \ , \tag{4.8}$$

where a new angular variable is introduced

$$u = 1 - v_R^2 = \sin^2\vartheta_R \ . \tag{4.9}$$

It is convenient to label the angular modes with u, because the physical zenith angle for the same ray changes with distance so that the equations would be more complicated. Labeling the angular dependence with u recognizes the uniqueness of a neutrino ray emitted ad one angle.

The density matrices $\varrho_{p,u,r}$ are not especially useful to describe a spherically symmetric system because they vary with radius even in the absence of oscillations. A quantity that is conserved in the absence of oscillations is the total flux matrix

$$\mathsf{J}_r = 4\pi r^2 \int \frac{\mathrm{d}^3\mathbf{p}}{(2\pi)^3}\,\varrho_{\mathbf{p},r}\,v_{\mathbf{p},r} \ . \tag{4.10}$$

To express the integral in comoving variables, we observe that $\mathrm{d}^3\mathbf{p}$ in spherical coordinates is $p^2\mathrm{d}p\,\mathrm{d}\varphi\,\mathrm{d}\cos\vartheta_r$ and that Eq. (4.8) implies

$$\left|\frac{\mathrm{d}\cos\vartheta_r}{\mathrm{d}u}\right| = \frac{1}{2v_{u,r}}\,\frac{R^2}{r^2} \ . \tag{4.11}$$

Therefore, we finally define the differential flux matrices

$$\mathsf{J}_{p,u,r} = \frac{R^2p^2\varrho_{p,u,r}}{2\pi} \ , \tag{4.12}$$

where we have used $\int\mathrm{d}\varphi = 2\pi$ for axial symmetry. The total flux matrix is now just

$$\mathsf{J}_r = \int_0^1 \mathrm{d}u \int_0^\infty \mathrm{d}p\ \mathsf{J}_{p,u,r} \ . \tag{4.13}$$

In the absence of oscillations, the total and differential fluxes are conserved, $\partial_r \mathsf{J}_r = 0$ and $\partial_r \mathsf{J}_{p,u,r} = 0$.

Since the radial velocity along a neutrino trajectory is $v_{u,r} = \mathrm{d}r_u/\mathrm{d}t = \cos\vartheta_{u,r}$, taking the radial distance instead of time as the independent variable in Eq. 4.3 transforms the derivative $\partial_t \to v_{u,r}\partial_r$, so that the equation of motion become $\mathrm{i}\partial_r \mathsf{J}_{p,u,r} = v_{u,r}^{-1}[\mathsf{H}, \mathsf{J}_{p,u,r}]$. In other words, we project the evolution along a given trajectory to an evolution along the radial direction. For vacuum oscillations this has the effect of "compressing" the oscillation pattern for non-radial modes, so that even for monochromatic neutrinos, the effective vacuum oscillation frequency depends on both r and u.

The equations of motion for the flux matrices are finally [Esteban-Pretel 2008b]

$$\mathrm{i}\partial_r \mathsf{J}_{p,u,r} = [\mathsf{H}_{p,u,r}, \mathsf{J}_{p,u,r}] \tag{4.14}$$

with the Hamiltonian

$$\begin{aligned} \mathsf{H}_{p,u,r} &= \frac{\mathsf{M}^2}{2p} v_{u,r}^{-1} + \lambda \mathsf{L}\, v_{u,r}^{-1} \\ &+ \frac{\sqrt{2}\, G_\mathrm{F}}{4\pi r^2} \int \mathrm{d}u' \int \mathrm{d}q \left(\frac{1}{v_{u,r} v_{u',r}} - 1 \right) (\mathsf{J}_{q,u',r} - \bar{\mathsf{J}}_{q,u',r}) \end{aligned} \tag{4.15}$$

and the same for $\bar{\mathsf{J}}_{q,u',r}$ with $\frac{\mathsf{M}^2}{2p} \to -\frac{\mathsf{M}^2}{2p}$.

4.2.2 Polarization vectors

There is no unique way to introduce polarization vectors. In fact, the number of conventions used in the literature is probably comparable to number of authors, with some contributing more to the entropy of the field. One definition suitable in the SN context is

$$\begin{aligned} \mathsf{J}_{p,u,r} &= \frac{F(\nu_e)_{p,u} + F(\nu_x)_{p,u}}{2} + \frac{F(\bar\nu_e) - F(\bar\nu_x)}{2} \mathbf{P}_{p,u,r} \cdot \boldsymbol{\sigma} \ , \\ \bar{\mathsf{J}}_{p,u,r} &= \frac{F(\bar\nu_e)_{p,u} + F(\bar\nu_x)_{p,u}}{2} + \frac{F(\bar\nu_e) - F(\bar\nu_x)}{2} \overline{\mathbf{P}}_{p,u,r} \cdot \boldsymbol{\sigma} \ , \end{aligned} \tag{4.16}$$

where $\boldsymbol{\sigma}$ is the vector of Pauli matrices. The quantity $F(\nu_\alpha)_{p,u}$ is the number flux of ν_α neutrinos emitted from the neutrino sphere with energy $E \in (p, p + dp)$ and at an angle $\sin^2\vartheta_R \in (u, u + du)$. The total number flux of flavor α is a simple integral $F(\nu_\alpha) = \int \mathrm{d}p \int \mathrm{d}u\, F(\nu_\alpha)_{p,u}$. Note that the normalization of the second term is the same and it is the difference between flux of $\bar\nu_e$'s and $\bar\nu_x$'s. As a consequence, at the neutrino sphere we have the normalization

$$P_z = |\mathbf{P}| = 1 + \epsilon \quad \text{and} \quad \bar P_z = |\bar{\mathbf{P}}| = 1 \ , \tag{4.17}$$

where epsilon in the asymmetry of the spectra

$$\epsilon = \frac{F(\nu_e) - F(\bar{\nu}_e)}{F(\bar{\nu}_e) - F(\bar{\nu}_x)} \ . \tag{4.18}$$

The first terms in Eqs. 4.16 are simply $\frac{1}{2}\mathrm{Tr}(\mathsf{J}_{p,u,r})$, i.e. they represent the sum of the fluxes and are constant during the evolution, reflecting the conservation of number of neutrinos in the absence of momentum-exchanging processes. Being proportional to the identity matrix, they disappear under the commutator in the equations of motion.

At the neutrino sphere we have a coherent state $\mathsf{J}^{init}_{p,u,R} = \mathrm{diag}(F(\nu_e)_{p,u}, F(\nu_x)_{p,u})$, so the initial conditions for the polarization vectors are

$$\begin{aligned} P^z_{p,u,R} &= |\mathbf{P}_{p,u,R}| = \frac{F(\nu_e)_{p,u} - F(\nu_x)_{p,u}}{F(\bar{\nu}_e) - F(\bar{\nu}_x)} \quad \text{and} \\ \bar{P}^z_{p,u,R} &= |\bar{\mathbf{P}}_{p,u,R}| = \frac{F(\bar{\nu}_e)_{p,u} - F(\bar{\nu}_x)_{p,u}}{F(\bar{\nu}_e) - F(\bar{\nu}_x)} \ . \end{aligned} \tag{4.19}$$

Finally, we use the definition of the polarization vectors(Eq. 4.16) in the equations of motion 4.15 to obtain the equations for the polarization vectors

$$\begin{aligned} \partial_r \mathbf{P}_{p,u,r} = \ & \Big[v^{-1}_{u,r} \left(\omega_p \, \mathbf{B} + \lambda \, \mathbf{L} \right) + \sqrt{2} \, G_{\mathrm{F}} \, \tfrac{F(\bar{\nu}_e) - F(\bar{\nu}_x)}{4\pi r^2} \ldots \\ \ldots \ & \int \mathrm{d}p' \int \mathrm{d}u' \left(\tfrac{1}{v_{u,r} v_{u',r}} - 1 \right) \left(\mathbf{P}_{p',u',r} - \overline{\mathbf{P}}_{p',u',r} \right) \Big] \times \mathbf{P}_{p,u,r} \end{aligned} \tag{4.20}$$

and similarly for antineutrinos.

In general, full multi-angle–multi-energy simulations are very difficult. Even for a toy model of a SN, with a black body emission at the neutrino sphere $R_\nu = 10$ km, and a matter profile as in Fig. 4.3, a proper simulation is very challenging. We must resort to simplifications.

4.3 Single-angle approximation

The easiest way to get a grasp of the effects a SN neutrino flux can suffer is to neglect the multi-angle nature of the problem. Of course, far from being realistic, this simplification overlooks a very important effect of kinematical decoherence due to different trajectories in both vacuum and matter terms, but it offers a clean playground to study the effects of various terms in the equations of motion. It also preserves the energy structure of the spectra, the only thing detectable on Earth.[3]

[3] Seen from Earth, a supernova is a point-like object, so no angular resolution is ever possible.

The main idea is to assume an angular mode representative for all. For a black body emission, in which all of the angular modes are equally occupied, it is natural to take neutrinos emitted at $\vartheta_R = 45°$ ($u_0 = 0.5$) as the representative ones. In this case, there is no integration over u and all the radial velocities appearing in the equation are set to

$$v = \sqrt{1 - \frac{R^2}{2r^2}} \ . \tag{4.21}$$

The angular dependence in the self-interaction term simplifies to

$$\frac{1}{v_{u_0,r} v_{u_0,r}} - 1 \to \frac{R^2}{2r^2} \frac{1}{1 - \frac{R^2}{2r^2}} \ , \tag{4.22}$$

making it depend only on the difference of the total polarization vectors

$$\mu_r \left(\mathbf{P}_r - \overline{\mathbf{P}}_r \right) \times \mathbf{P}_{p,r} \ . \tag{4.23}$$

Here we have introduced the radial dependent neutrino self-interaction strength μ as

$$\mu_r = \sqrt{2}\, G_{\mathrm{F}} \ \frac{F(\bar{\nu}_e) - F(\bar{\nu}_x)}{4\pi R^2} \ \frac{R^4}{2r^4} \ \frac{1}{1 - \frac{R^2}{2r^2}} \ . \tag{4.24}$$

For large distances from the core, it scales as $\propto R^4/2r^4$.[4] The equations of motion for polarization vectors can now be written in a concise form

$$\begin{aligned} \partial_r \mathbf{P}_{p,r} &= \left[+\omega_p \, \mathbf{B} + \lambda \, \mathbf{L} + \mu_r \left(\mathbf{P}_r - \overline{\mathbf{P}}_r \right) \right] \times \mathbf{P}_{p,r} \\ \partial_r \overline{\mathbf{P}}_{p,r} &= \left[-\omega_p \, \mathbf{B} + \lambda \, \mathbf{L} + \mu_r \left(\mathbf{P}_r - \overline{\mathbf{P}}_r \right) \right] \times \mathbf{P}_{p,r} \end{aligned} \tag{4.25}$$

4.3.1 Self-interaction suppression in supernovae

The self-maintaining coherence of bipolar oscillations plays very important role in the SN neutrino physics. Contrary to the case exposed in Sec. 1.5.2, in the SN environment, neutrino–self-interaction strength scales as r^{-4}, so the behavior is somewhat different. Unlike the exact periodic motion as in Fig. 1.4,

[4] Some authors [Duan 2006, Fogli 2007] prefer to reduce the equations to a single-angle by assuming all the angular modes behave as the radial one. In this case, one writes equations only for $u = 0$, but does not neglect the other angular modes. Instead, the integration over angles in Eq. 4.20 is actually performed to obtain somewhat different radial dependence of $(1 - \sqrt{1 - R^2/r^2})^2$. At large radii, this "averaged angle" approximation scales as $\propto R^4/4r^4$, i.e. is weaker than the strict single-angle approach by a factor of two. In comparing with the multi-angle simulations, it turns out that the single-angle grasps better the relevant effects.

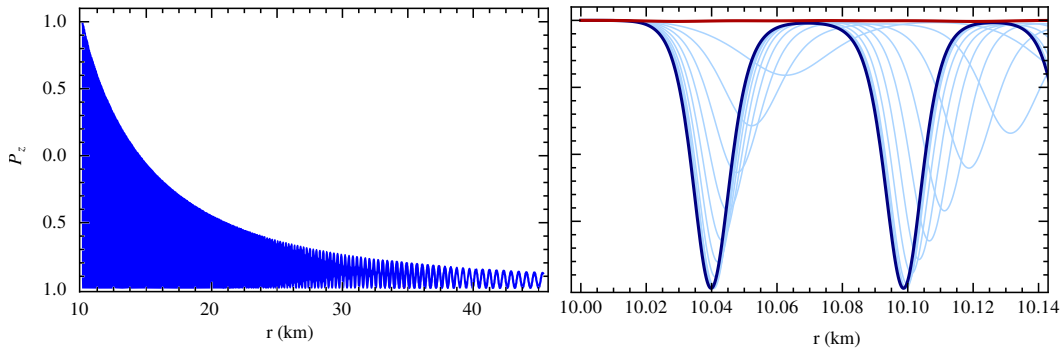

Figure 4.5: *Left Panel:* P_z for ν_e and $\overline{\nu}_e$ in a toy supernova model (inverted hierarchy, mixing angle $\theta = 0.02$, single frequency $\omega = 0.3$ km^{-1}, $\mu = 0.3 \times 10^5$ km$^{-1}(R/r)^4$ and the radius of the neutrinosphere $R = 10$ km) with symmetric initial conditions ($\epsilon = 0$). *Right Panel:* Zoom in the region close to neutrinosphere in the left panel (thick blue curve). The thick red line shows the evolution of the flavor content in the presence of the small asymmetry $\epsilon = 0.01$. Thin blue lines correspond to various intermediate values $\epsilon \in \{0.001, 0.002, \ldots, 0.009\}$.

this case shows an evident decline of upper envelope of survival probability (Fig. 4.5 left panel). In the pendulum analogy, this effect is easy to understand: At the neutrinosphere, the system begins with the usual bipolar oscillations. As the pendulum oscillates, we adiabatically increase its moment of inertia μ^{-1} (μ decreases with radius), so at each swing, the pendulum does not have enough energy to reach to the previous height. In the end it settles in the position performing just harmonic oscillations around the direction $\mathbf{B}$.

However, the situations complicates in the presence of a non-vanishing neutrino asymmetry ϵ. If the asymmetry is large enough, the non-vanishing initial value of the total polarization vector $(\mathbf{P} - \overline{\mathbf{P}})$, multiplied by μ can make the self-interaction term high enough to completely suppress any evolution. The right panel of Figure 4.5 shows that: Prominent bipolar oscillations which reach almost complete conversions are very sensitive to even small values of asymmetry. The change in behavior is noticeable even for the asymmetry of a few thousandths. In this example the value $\epsilon = 0.01$ is enough to block flavor conversions, sticking all of the polarization vectors to one. Of course, as μ decreases, at some on-set radius it is not strong enough to hold the polarization vectors together and the bipolar oscillation start after all. So, interestingly, in the presence of asymmetry, bipolar oscillations are not associated with the limit of infinite self-interaction, but rather with the intermediate values.

In the single-angle approximation, a constant matter potential in Eq. 4.25

acts equally to all modes, so it has no physical effects. It can be made explicit by switching to a frame of reference that rotates around **B** with a frequency λ (see Sec. 1.4). This fast rotation around one direction then stabilizes the pendulum. However, the effect is just in the logarithmic delay of the onset radius of the bipolar phase. The same logarithmic dependence is observed with the decrease of the mixing angle, so the matter effect in the single-angle simulations can be mimicked by and artificially small mixing angle.

4.3.2 Spectral swaps

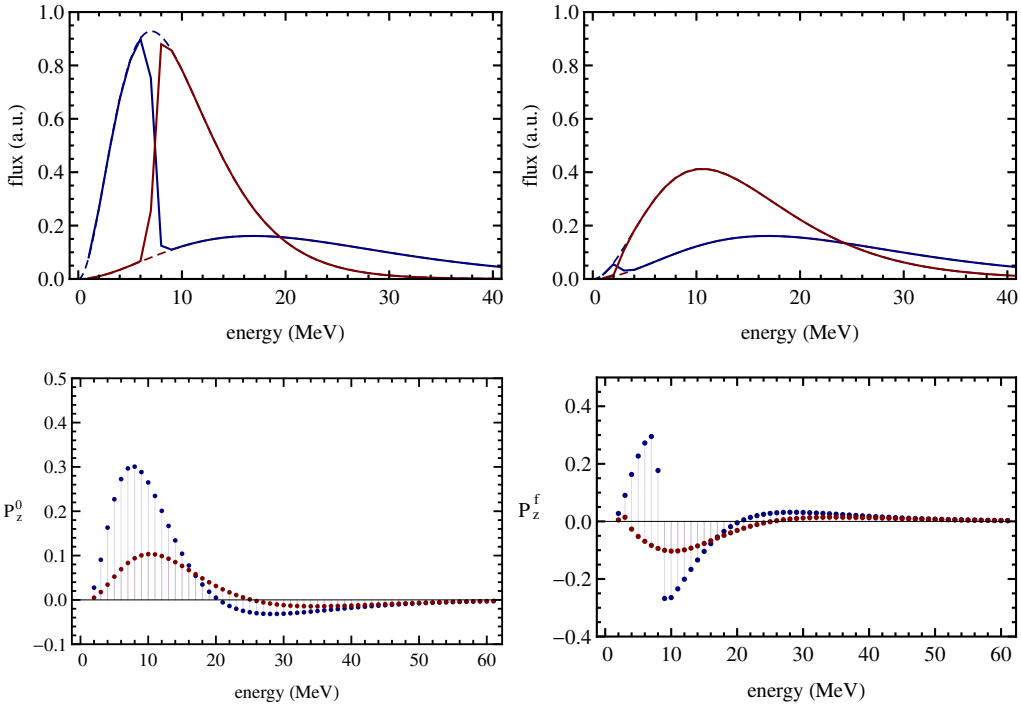

Figure 4.6: *Top:* Final spectra of neutrinos (top left) and antineutrinos (top right panel) superimposed on merely visible non-oscillated initial spectra (dashed lines). Blue curves are for electron and red curves for other flavor. *Bottom:* Initial (left) and final (right) spectra of the z component of the polarization vectors. Blue points represent P_z^i (blue points) and red points $\overline{P}_z^i$.

In a complex system with multiple number of modes, a typical outcome of a simulation is with some of the polarization vectors pointing down and some of them pointing up.[5] This shows up in the spectra as a spectral swap,

[5]Let me remind that the notion on what is vertical is determined by the mass-direction

probably the most peculiar phenomena observed in the physics of neutrinos streaming from a supernova — a part or a complete spectrum is swapped between neutrino species. In Figure 4.6 an example of spectral swaps is shown. We start with the equal luminosities and Fermi-Dirac spectra for all species, but different mean energies ($E_{\nu_e} = 10$, $E_{\bar{\nu}_e} = 15$ and $E_{\nu_x} = 24$ MeV), and we evolve it through potentials from Fig. 4.3. After the collective oscillations, the spectrum of neutrinos is the same as the original one until some energy E_{split}, and after that it is as the spectra of the other flavor. IN the antineutrino sector we have a almost complete swap.

In Figure 4.7 we see that the evolution of the individual polarization vectors is qualitatively the same. At first, until $\sim$ 60 km, very large asymmetry $\epsilon = 1.33$, typical for the cooling phase, in combination with high μ makes all the polarization vector precess with the same very high frequency, keeping them aligned and basically stuck together. The matter term in that region is also very high making the effective mixing angle very small, so that the synchronized oscillations have such a small amplitude that they are not even visible. After the matter term has dropped to some intermediate values, the common polarization vector, formed during the synchronization phase, begins to fall down and to perform bipolar oscillations. The decrease of μ makes the oscillations loose their amplitude and eventually die out and the polarization vectors are driven to their final positions. We are left with almost a complete swap in the antineutrino sector and a partial in the neutrino sector — the polarization vectors below the split energy are driven back to their initial position pointing upwards.

Qualitatively, we would not actually expect a complete conversion in both neutrino and antineutrino sectors: The initial conditions in supernova dictate the larger number of neutrinos than antineutrinos and the same number of other species, so if all the antineutrinos swapped, conservation of the net lepton number [Fogli 2007]

$$\int_{E_{\text{split}}}^{\infty} \mathrm{d}E(F^{\nu_e}_{E,R} - F^{\nu_x}_{E,R}) = \int_{0}^{\infty} \mathrm{d}E(F^{\bar{\nu}_e}_{E,R} - F^{\nu_x}_{E,R}) \tag{4.26}$$

prevents the same thing happening to neutrinos. For the example, from Eq. 4.26 the splitting energy if found to be $E_{\text{split}} \simeq 7$ MeV in a good agreement with observed situation. These heuristic arguments, of course, do not explain the dynamics of the system that allowed it to reach this state neither why the conversions in the antineutrino sector are almost complete. In fact, it can be shown that the formation of spectral splits is a general property of spectra with crossings and that in the limit of perfect adiabaticity, antineutrinos

always manifest complete flavor conversions. Any deviation from a complete swap in the antineutrino sector is related with the presence of matter terms and the μ radial slope [Fogli 2008].

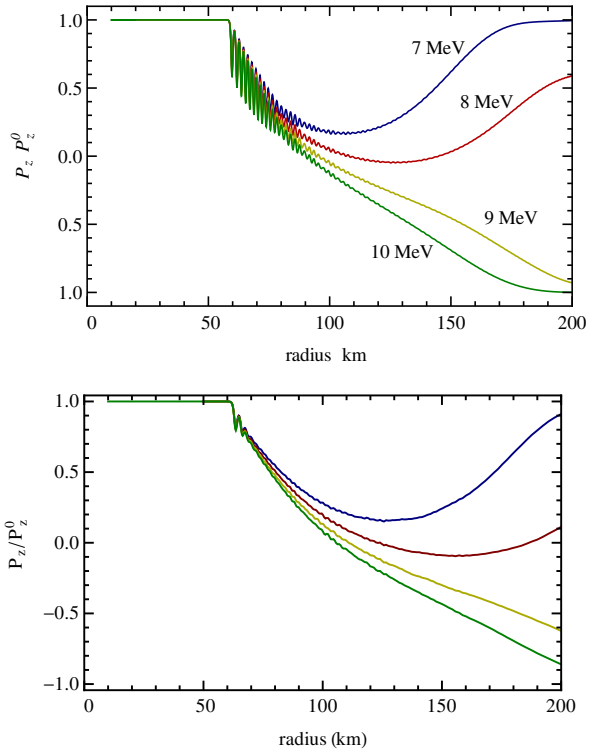

Figure 4.7: Radial evolution of P_z^i normalized to initial value for particular energies in the single-angle approximation (top panel) and in multi angle case (bottom panel) Synchronised, bipolar and the phase in which the spectral split is formed are clearly visible.

4.4 Multi-angle treatment

Incorporating the multi-angle nature of the problem in the simulations requires codes with more powerful integrators wit greater CPU-time demands. The presence of matter in multi-angle treatment is not as trivial as in the single-angle case — the matter term depends on the angle and introduces new source of kinematical decoherence, just as the vacuum term in previous considerations. Of course, also here the vacuum term leads to kinematical decoherence — it is different for each angle and p mode, but typically $\lambda \gg \omega$, so the decoherence due to the vacuum term can be neglected. Physically, it amounts to different angular modes arriving at the same radius had follow

different trajectories and acquiring different phases in the precession. So, if there was not for their internal interaction keeping them fixed one to another, they would quickly decohere. How quickly, of course, depends on the value of λ. Moreover, λ has the maximum at the same place as μ, close to neutrinosphere, so the interplay between these two effects must be treated with great care.

For the supernova spectra and the matter profile from the previous considerations (Fig. 4.6), a proper treatment of the angular modes does not yield in different final spectra [Fogli 2007]. Kinematical decoherence is noticeable only in the evolution of the individual polarization vectors (Fig. 4.7 bottom panel). For sufficiently large asymmetry, the radial variation of different angular modes is collective and they behave as if they were all emitted with the same angle relative to the radial direction. These conclusions are not analitically understood but are consistently observed in numerical simulations.

In general, the decoherence among different angular modes does occur and leads to different results with respect to the single-angle study. In fact it is self-accelerating if the asymmetry ϵ is very small and the matter densities are very high, such as during the accretion phase of the SN explosion.

In practice, the number of angular bins necessary to have a stable solution and extract any conclusion depends highly on the value of matter terms and the asymmetry, ranging from 60 (for the toy case described – moderate matter densities and large asymmetry) to $\mathcal{O}(10^3)$, for simulations of fluxes from a SN in accretion phase with high λ and small ϵ. This is the main problem in simulations of SN fluxes: We expect the highest neutrino signal during the accretion phase, exactly when the simulations are most difficult — the matter density can largely surpass the neutrino density and the neutrino asymmetry has the smallest values (see Fig. 4.8).

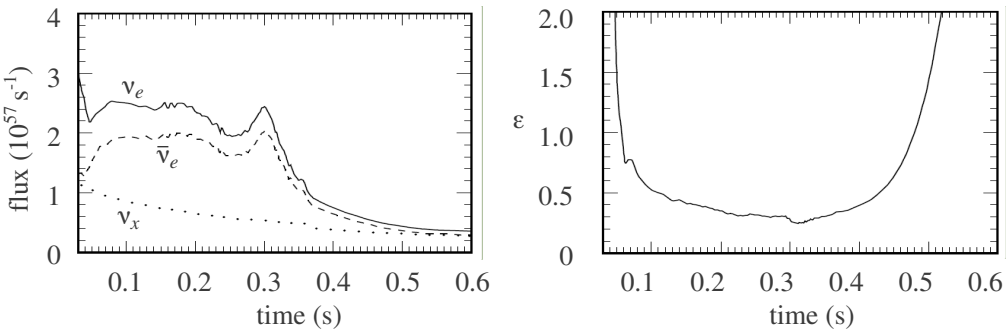

Figure 4.8: Time evolution of neutrinos fluxes and the asymmetry during the accretion phase, for a $10.8M_\odot$ model [Fischer 2010]. Adapted from [Chakraborty 2011].

Due to numerical difficulties, it is customary to reduce the energy modes to one, keeping the angular structure. The usual choice of a representative energy is 15 MeV, corresponding to a frequency $\omega \simeq 0.4$ km^{-1}. It is not essential since the main purpose is to determine if the dense matter affects the collective conversions.

Chapter 5

Flavor stability analysis for neutrinos streaming from a supernova

The neutrino-neutrino interactions make the neutrino flux evolution close to a supernova (SN) core numerically very challenging and are able even to completely swap spectra of different flavors [Dasgupta 2009]. It has been shown that the multi-angle matter effects can suppress the flavor evolution during the accretion phase when the matter density is higher or comparable to neutrino densities [Esteban-Pretel 2008a]. However, during this phase the interplay between neutrino collective effects and (ordinary) matter effects is most delicate and we are forced to make various simplifications of the problem (single-angle, single-energy, semi-isotropic radiation etc.). However, recent linearized stability analysis (LSA) of the flavor evolution equations, developed in Ref. [Banerjee 2011], allows for the first time the full analytic treatment of the problem, without the need for any of the mentioned simplifications.

5.1 Stability analysis

5.1.1 Linearized equation of motion

The equations of motion for the flux matrices J and $\bar{\mathsf{J}}$, derived in the previous Chapter, are driven by the Hamiltonian in Eq. 4.15. However, instead of writing down two equations for neutrinos and antineutrinos with the change in sign of vacuum frequency, it is sometimes useful to think of antineutrinos in the Dirac hole picture and represent them through negative occupation numbers for (differential) flux matrices $\mathsf{J}_{E,u,r}$ for negative energies. This sign convention simplifies the formalism and allows one never to distinguish between neutrinos and antineutrinos. The Hamiltonian driving the system now is written more concisely

$$\mathsf{H}_{p,u,r} = \frac{\mathsf{M}^2}{2p} v_{u,r}^{-1} + \lambda \mathsf{L}\, v_{u,r}^{-1} + \frac{\sqrt{2}\, G_{\mathrm{F}}}{4\pi r^2} \int \mathrm{d}u' \int \mathrm{d}q \left(\frac{1}{v_{u,r} v_{u',r}} - 1 \right) \mathsf{J}_{q,u',r} \ . \quad (5.1)$$

The vacuum oscillations are described by the vacuum frequency matrix

$$\frac{\mathsf{M}^2}{2p} = \pm\frac{\omega}{2}\begin{pmatrix}\cos 2\theta & \sin 2\theta \\ \sin 2\theta & -\cos 2\theta\end{pmatrix} \ , \tag{5.2}$$

background matter through the matrix $\lambda\mathsf{L} = \mathrm{diag}(\lambda, 0)$ and $v_{u,r}$ is the radial projection of neutrino velocity at the radius r. The upper sign refers to the inverted hierarchy and the lower to normal. If not explicitly stated, only the inverted hierarchy will be considered, but we should keep in mind that going back to normal hierarchy requires just a switch $\omega \to -\omega$. As before, the angular dependence is labeled with $u = \sin^2\vartheta_R = (1-\cos^2\vartheta_r)\, r^2/R^2$, where R is the radius of the neutrinosphere. Henceforth we drop the explicit subscript r to denote the r-dependence of all quantities.

Instead of polarization vectors, matrix formalism is more apt for this chapter. Useful quantity to describe the flavor content is the swapping matrix S, defined through

$$\mathsf{J}_{p,u} = \frac{\mathrm{Tr}\,\mathsf{J}_{p,u}}{2} + \frac{F^e_{p,u,R} - F^x_{p,u,R}}{2}\,\mathsf{S}_{p,u} \ , \tag{5.3}$$

where $F^{e,x,R}_{p,u}$ are differential flavor fluxes at the inner boundary radius R. For positive energies $p > 0$, $F^{e,x} \equiv F^{\nu_e,\nu_x}$, while for negative energies $p < 0$, $F^{e,x} \equiv -F^{\bar\nu_e,\nu_x}$.

Normalization of the swapping matrix is chosen so that at the boundary radius, where neutrinos are emitted, it has only diagonal entries

$$\mathsf{S}_{p,u} \equiv \begin{pmatrix} s_{p,u} & S_{p,u} \\ S^*_{p,u} & -s_{p,u}\end{pmatrix} = \begin{pmatrix}1 & 0 \\ 0 & -1\end{pmatrix} \ , \tag{5.4}$$

i.e. initial condition in terms of the swapping matrix reduce to $s = 1$, $S = 0$.

As always, the flux summed over all flavors, $\mathrm{Tr}\,\mathsf{J}_{p,u} = F^e_{p,u} + F^x_{p,u}$, is conserved in our free-streaming limit and does not contain any information relevant for physics, which is contained only in the trace-free part of the Hamiltonian. The vacuum term defined as in Eq. 5.2 is already traceless, the background medium term reduces to $\lambda\mathsf{L} \xrightarrow{-\mathrm{Tr}} \frac{\lambda}{2}\,\mathrm{diag}(+1,-1)$ and the self-interaction can be written as

$$\begin{aligned}\frac{\sqrt{2}\,G_\mathrm{F}}{4\pi r^2}\int\int\cdots\mathsf{J}_{q,u',r} \quad &\xrightarrow{-\mathrm{Tr}} \quad \frac{\sqrt{2}\,G_\mathrm{F}}{4\pi r^2}\int\int\cdots\frac{F^e_{q,u',R} - F^x_{q,u',R}}{2}\,\mathsf{S}_{q,u',r} \\ &= \quad \mu_R\,\frac{R^2}{2r^2}\int\int\cdots g_{q,u'}\,\mathsf{S}_{q,u',r} \ . \end{aligned} \tag{5.5}$$

The parameter μ_R is defined as

$$\mu_R = \sqrt{2}\,G_\mathrm{F}\frac{F^{\bar\nu_e}_R - F^{\nu_x}_R}{4\pi R^4} \ , \tag{5.6}$$

while $g_{p,u}$ is the flavor difference spectrum

$$g_{p,u} = \frac{F^{\nu_e}_{p,u,R} - F^{\nu_x}_{p,u,R}}{F^{\bar{\nu}_e}_{R} - F^{\nu_x}_{R}} \text{ for } E > 0\,, \text{ and}$$
$$g_{p,u} = \frac{F^{\bar{\nu}e}_{p,u,R} - F^{\nu_x}_{p,u,R}}{F^{\bar{\nu}_e}_{R} - F^{\nu_x}_{R}} \text{ for } E > 0\ . \tag{5.7}$$

It is adimensional (up to integration) with the normalization in antineutrino sector

$$\int_{-\infty}^{0} \mathrm{d}E \int_{0}^{1} \mathrm{d}u\, g_{p,u} = \frac{-F^{\bar{\nu}_e}_{R} - (-F^{\nu_x}_{R})}{F^{\bar{\nu}_e}_{R} - F^{\nu_x}_{R}} = -1\ . \tag{5.8}$$

The integration of $g_{p,u}$ over both neutrinos and antineutrinos gives the asymmetry of the spectra

$$\int_{-\infty}^{\infty} \mathrm{d}E \int_{0}^{1} \mathrm{d}u\, g_{p,u} = -1 + \frac{F^{\nu_e}_{R} - F^{\nu_x}_{R}}{F^{\bar{\nu}_e}_{R} - F^{\nu_x}_{R}} = \epsilon\ . \tag{5.9}$$

For the purpose of discussing analytical aspects of the problem, it is more convenient to label the energy modes by their vacuum frequency $\omega = \frac{|\Delta m^2_{31}|}{2E} = 5.96\ \mathrm{km}^{-1}\left(\frac{\mathrm{MeV}}{E}\right)$. The equations essentially do not change except for the Jacobian of the integration in the ν–ν term which can be incorporated in the g-spectrum. The region around $\omega = 0$ corresponds to high-E tail and the high-ω tails fall off as ω^{-4} (see Fig. 5.1). The overall normalization is still fixed by $\int_{-\infty}^{0} \mathrm{d}\omega \int_{0}^{1} \mathrm{d}u\, g_{\omega,u} = -1$.

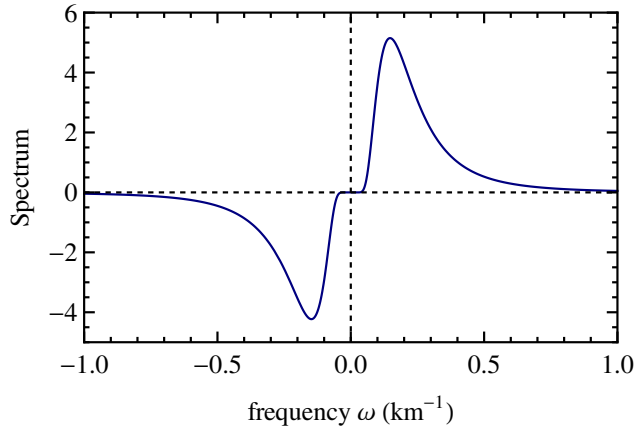

Figure 5.1: An example of the g_ω-spectrum for Fermi-Dirac (anti)neutrinos in the absence of other flavor. Temperature $T = 10$ MeV and degeneracy parameter $\xi = 0.1$, corresponding to the asymmetry $\epsilon = 0.2$.

The equation of motion for the swap matrix is now $\mathrm{i}\partial_r \mathsf{S}_{\omega,u} = [\mathsf{H}_{\omega,u}, \mathsf{S}_{\omega,u}]$, or explicitly

$$\begin{aligned} \mathrm{i}\partial_r s_{\omega,u} &= H_{\omega,u} S^*_{\omega,u} - H^*_{\omega,u} S_{\omega,u} \\ \mathrm{i}\partial_r S_{\omega,u} &= 2\left(S_{\omega,u} h_{\omega,u} - H_{\omega,u} s_{\omega,u}\right) \end{aligned} \tag{5.10}$$

with the Hamiltonian

$$\mathsf{H}_{\omega,u} \equiv \begin{pmatrix} h_{\omega,u} & H_{\omega,u} \\ H^*_{\omega,u} & -h_{\omega,u} \end{pmatrix} \ , \tag{5.11}$$

where the elements of the Hamiltonian are

$$\begin{aligned} h_{\omega,u} &= \mu_R \frac{R^2}{2r^2} \int \mathrm{d}\omega' \int \mathrm{d}u' \left(\frac{1}{v_u v_{u'}} - 1\right) g_{\omega',u'}\, s_{\omega',u'} + \left(\frac{\omega}{2}\cos 2\theta + \frac{\lambda}{2}\right)\frac{1}{v_u} \ , \\ H_{\omega,u} &= \mu_R \frac{R^2}{2r^2} \int \mathrm{d}\omega' \int \mathrm{d}u' \left(\frac{1}{v_u v_{u'}} - 1\right) g_{\omega',u'}\, S_{\omega',u'} + \frac{\omega}{2}\sin 2\theta\, \frac{1}{v_u} \end{aligned} \tag{5.12}$$

As a next step towards linearized equations suitable for linear analysis, we expand the radial velocity from Eq. 4.8 for large distance from the source

$$v_r = 1 + \frac{u}{2}\frac{R^2}{r^2} \ , \tag{5.13}$$

where bimodal oscillations actually begin. We are interested in small-amplitude limit of the Equations 5.10, so we set $s = 1$. The vacuum mixing angle is small, so it is safe to put $\cos 2\theta = 1$. Since $\lambda \gg \omega$ we can also neglect a small radius-dependent spread of frequencies $\omega\,(1 + uR^2/2r^2) \simeq \omega$. These approximations significantly simplify the elements of the Hamiltonian matrix

$$\begin{aligned} h_{\omega,u} &= \mu \int \mathrm{d}\omega' \int \mathrm{d}u' \frac{u+u'}{2}\, g_{\omega',u'} + \frac{\omega+\lambda}{2}\left(1 + \frac{u}{2}\frac{R^2}{r^2}\right) \ , \\ H_{\omega,u} &= \mu \int \mathrm{d}\omega' \int \mathrm{d}u' \frac{u+u'}{2}\, g_{\omega',u'} S_{\omega',u'} \ , \end{aligned} \tag{5.14}$$

where the usual definition of neutrino self-interaction is used

$$\mu = \mu_R \frac{R^4}{2r^4} \ . \tag{5.15}$$

The differential equation for $S_{\omega,u}$ now has terms common for all modes, $S_{\omega,u}\lambda$ and $S_{\omega,u}\int \mathrm{d}\omega' \int \mathrm{d}u' u'\, g_{\omega',u'} S_{\omega',u'}$. Such terms engender only pure precession same for all modes and are of no interest, so we can safely drop them out. There is also a term proportional to the overall integration of the g-spectrum, already defined as the asymmetry ϵ.

Finally, we arrive to the equation for $S_{\omega,u}$

$$\mathrm{i}\partial_r S_{\omega,u} = [\omega + u(\lambda + \epsilon\mu)]\, S_{\omega,u} - \mu \int du'\, d\omega'\, (u + u')\, g_{\omega' u'}\, S_{\omega',u'} \quad , \tag{5.16}$$

where the matter potential is redefined to incorporate also the imprint of the multiangle effects

$$\lambda := \lambda \frac{R^2}{2r^2} = \sqrt{2}\, G_{\mathrm{F}}(n_e - n_{\bar{e}}) \frac{R^2}{2r^2} \quad . \tag{5.17}$$

So defined, the background matter potential scales as $1/r^{\sim 4}$, just as μ (the additional two powers are from the usual matter density profiles $n_e \propto 1/r^{\sim 2}$). This is the linearized form of the general equations of motion and provides the starting point for the stability analysis.

Let me now just summarize the crucial elements of the analysis performed. Besides the small-amplitude approximation $|S_{\omega,u}| \ll 1$, we have taken the neutrinos to be far from the neutrino sphere, $(R/r)^2 \ll 1$, yet before the MSW resonance region, so that the ordinary matter effect is large and the effective mixing angle in matter is small ($\cos\theta = 1$). A proper treatment for non-zero mixing angle actually provides the initial disturbance to kick-start exponentially growing modes. Here, however, we do not ask how the instability gets started, but only discuss the existence of the exponentially growing modes.

5.1.2 Eigenvalue equation

For the purpose of stability analysis, the question is whether the small quantity $S_{\omega,u}$ does manifest exponential growth with radius. To investigate it, we write the solution of the linear differential equation 5.16 in the form

$$S_{\omega,u} = Q_{\omega,u}\, e^{-\mathrm{i}\Omega r} \tag{5.18}$$

where the eigenvector $Q_{\omega,u}$ and the frequency Ω are in general complex numbers. A purely real Ω would correspond to a pure precession mode, and a possible imaginary part would imply an exponential growth. This ansatz leads to the eigenvalue equation for $Q_{\omega,u}$ [Banerjee 2011],

$$(\omega + u\bar{\lambda} - \Omega)\, Q_{\omega,u} = \mu \int du'\, d\omega'\, (u + u')\, g_{\omega' u'}\, Q_{\omega',u'} \quad , \tag{5.19}$$

where $\bar{\lambda} \equiv \lambda + \varepsilon\mu$. Implicitly, $Q_{\omega,u}$ carries also a label Ω, because for every Ω, in general exist a different $Q_{\omega,u}$.

Note that if $(Q_{\omega,u}, \Omega)$ satisfy the eigenvalue equation 5.19, so do their complex conjugates $(Q^*_{\omega,u}, \Omega^*)$. Therefore, for each complex solution $\Omega = \gamma + \mathrm{i}\kappa$

there exist another solution $\Omega = \gamma - \mathrm{i}\kappa$. A positive imaginary part corresponds to exponential growth and a negative one to exponential decay toward the asymptotic solution $S_{\omega,u} = 0$. Since they always appear in pairs it is enough to determine one.

The right-hand side of the Eq. 5.19 is of the form $a + bu$, so we can search for a solution of the form

$$Q_{\omega,u} = \frac{a + bu}{\omega + u\bar{\lambda} - \Omega} \ , \tag{5.20}$$

with a and b complex numbers that in general do not depend on either ω or u. Inserting this ansatz in the eigenvalue equation provides

$$a + bu = \mu \int \mathrm{d}u' \, \mathrm{d}\omega' \, g_{\omega',u'} \, \frac{(u + u')(a + b\,u')}{\omega' + u'\bar{\lambda} - \Omega} \ . \tag{5.21}$$

The structure of this equation is more transparent if we define the integrals

$$I_n = \int \mathrm{d}u \, \mathrm{d}\omega \, g_{\omega,u} \, \frac{u^n}{\omega + u\bar{\lambda} - \Omega} \ . \tag{5.22}$$

Then our eigenvalue equation becomes

$$a + bu = \mu \Big[(aI_1 + bI_2) + (aI_0 + bI_1)u \Big] \ . \tag{5.23}$$

This equation is supposed to be satisfied for every u, so we need to match the coefficients of the linear u polynomial on both sides separately. We can then write this in matrix form

$$\mu^{-1} \begin{pmatrix} a \\ b \end{pmatrix} = \begin{pmatrix} I_1 & I_2 \\ I_0 & I_1 \end{pmatrix} \begin{pmatrix} a \\ b \end{pmatrix} \ . \tag{5.24}$$

This has the form of an eigenvalue equation for a 2×2 matrix and so the nontrivial solutions exist if

$$\det \left[\begin{pmatrix} I_1 & I_2 \\ I_0 & I_1 \end{pmatrix} - \mu^{-1} \right] = 0 \tag{5.25}$$

or explicitly

$$(I_1 - \mu^{-1})^2 = I_0 I_2 \ . \tag{5.26}$$

This equation is the basis of the stability analysis of the neutrino flux streaming from a supernova.

To summarize, the necessary ingredients for the stability analysis are:

(i) the adimensional $g_{\omega,u}$-spectrum going in the integrals in Eq. 5.22 and whose total integrals gives the asymmetry ϵ,

(*ii*) absolute values of the neutrino fluxes $F_R^{\bar{\nu}_e}$ and $F_R^{\nu_x}$ at the neutrino sphere, for the definition of μ_R and later μ (Eqs. 5.15 and 5.6), and

(*iii*) the matter density profile $n_e(r)$, which goes into definition of matter potential λ (Eq. 5.17).

Of course, the first two ingredients are degenerate with having distributions for all three species $F_R^{\nu_e}$, $F_R^{\bar{\nu}_e}$ and $F_R^{\nu_x}$.

Normal hierarchy

Turning to the normal hierarchy case corresponds to the change $\omega \to -\omega$ in Eq. 5.16 to obtain and equation for the off-diagonal elements of the swap matrix $\tilde{S}_{\omega,u}$ in the normal hierarchy

$$\mathrm{i}\partial_r \tilde{S}_{\omega,u} = [-\omega + u(\lambda + \epsilon\mu)]\, \tilde{S}_{\omega,u} - \mu \int du'\, d\omega'\, (u + u')\, g_{\omega' u'}\, \tilde{S}_{\omega',u'} \quad , \tag{5.27}$$

In terms of the solution $S_{\omega,u}$ of Eq. 5.16, the solution of this equation is given by

$$\tilde{S}_{\omega,u}(\mu, \lambda, g_{\omega,u}) \;\; = \;\; S^*_{\omega,u}(\mu, -\lambda, -g_{\omega,u}) = S^*_{\omega,u}(-\mu, -\lambda, g_{\omega,u}) \;\; . \tag{5.28}$$

Since S and S^* should have the same stability behavior, this implies that the stability conditions for normal hierarchy are the same as those for the inverted hierarchy with a change in the sign of $g_{\omega,u}$ or μ and the additional change in the sign of λ.

5.2 Comparison with simulations

5.2.1 Schematic spectra

To completely appreciate the linearized flavor-stability analysis exposed in the previous section, it was necessary to confront it with numerical simulations. For this, we have chosen the analysis of the flavor conversion during the accretion phase of a supernova performed by Chakraborty et al. [Chakraborty 2011]. Although they have assumed a schematic model with semi-isotropic and monochromatic spectra ($\omega_0 = 0.4$ km^{-1}), these simulations are numerically very demanding because of high neutrino fluxes which contribute to the stiffness and unreliability of the system and even higher matter densities which are supposed to suppress any flavor evolution.

They have performed numerical simulation of the neutrino flavor evolution for the $10.8\, M_\odot$ model at various post bounce times (Fig. 4.8) and found

that partial flavor conversions do occur after all, but in a small time-window $200\,\mathrm{ms} \lesssim t_{\mathrm{pb}} \lesssim 300\,\mathrm{ms}$.

From the point of view of the stability analysis, $g_{\omega,u}$ spectrum has a very

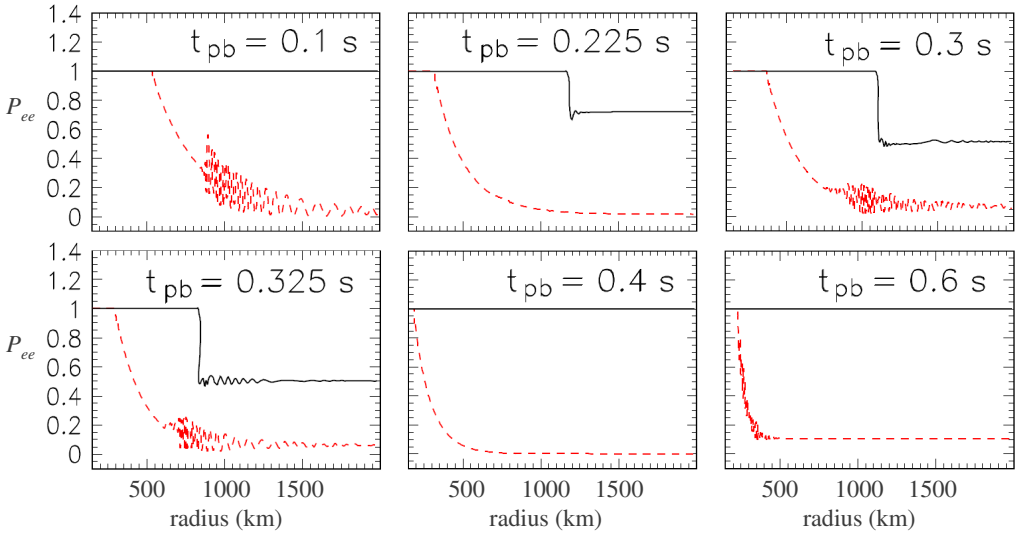

Figure 5.2: Survival probability for electron antineutrinos as a function of radius for different snapshots of a $10.8 M_{\odot}$ model from Fig. 4.8 [Fischer 2010]. Red dashed lines are results of evolution without matter. Figure adopted from [Chakraborty 2011].

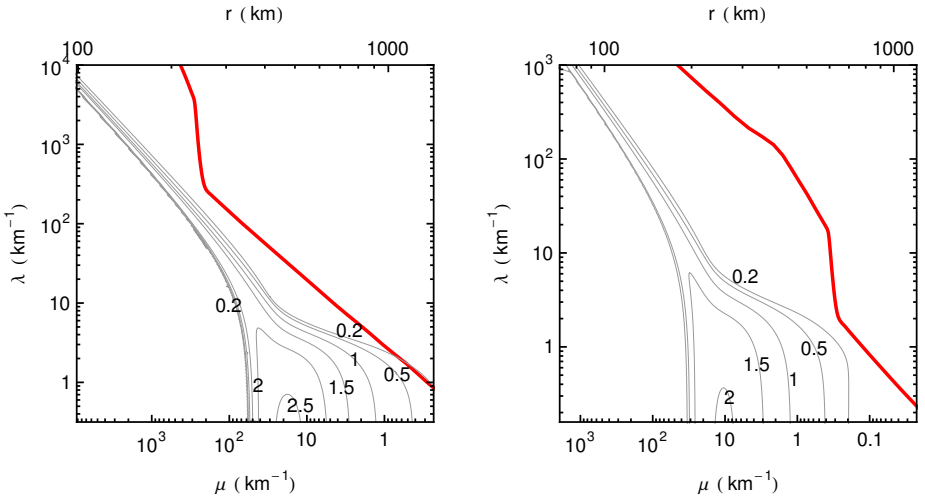

Figure 5.3: Contours of κ and the trajectory of SN (thick red line) at $t =$ 300 ms (left) and 400 ms (right) post bounce for a $10.8\,M_{\odot}$ model discussed in Ref. [Chakraborty 2011].

simple form

$$g_{\omega,u} = -\delta(\omega + \omega_0) + (1 + \varepsilon)\,\delta(\omega - \omega_0) \tag{5.29}$$

and the integrals I_n can be solved analytically. Then it is straightforward to find a combination (γ, κ) for each pair (μ, λ). This is exactly what we did for each of the snapshots in Fig. 5.2 — we have basically scanned the plane (μ, λ) in search of the solution with $\kappa \neq 0$ Figure 5.3 summarize the results of our scan for two representative snapshots at $t = 300$ ms and $t = 400$ ms post bounce, where we plot the isocontrours of κ in the (μ, λ)-plane. In the same plane, we then draw a parametric curve $(\mu(r), \lambda(r))$ a supernova actually follows, so called *trajectory*. Basically, since the radial dependence of μ is a pure power law, the trajectory can be plotted vs. r as well. Note that high λ and high μ region in the upper left corner of the plot is close to the proto-neutron star.

The scale of the system is set by its mean vacuum frequency, usually of $\mathcal{O}(0.1)$, so the instability region could be defined as $\kappa \simeq 0.1$. If the trajectory of the supernova enters the instability region, exponentially growing modes exist, and the flavor conversion do occur. Of course, being a linearized and approximate, the flavor stability analysis cannot answer the question of the final state of the system, but rather only if anything happens at all.

Using the linearized stability analysis we obtain [Sarikas 2011a] the same results as from the simulations [Chakraborty 2011]: when their spectra are stable, the SN trajectory does not cross the instability region, and for snapshots where they see partial flavor conversion we see trajectory of the SN entering the instability region far from the neutrinosphere; we even find the exact onset radius at which it happens! Figure 5.3 shows the region where $\kappa \neq 0$ solutions exist together with its isocontours and the trajectory of the supernova in (μ, λ) plane.

5.2.2 Two instability crossings

We find interesting a possibility of two instability crossings if the supernova is following the path $\lambda \sim 0.4\,\mu$. In that case it would cross twice the IR. We run few simulations that confirmed this scenario.

The outcome of one of them is shown in Fig. 5.4. Again we find the same type and quality of agreement as when comparing with the simulations [Chakraborty 2011]. When $\kappa > 0$, the off-diagonal element of the swap matrix $|S|$ oscillates and grows exponentially and the system is unstable, while for $\kappa = 0$, it just oscillates periodically, i.e. system is stable.

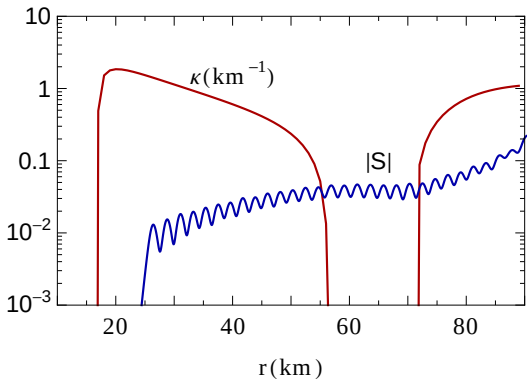

Figure 5.4: Instability parameter κ and the off-diagonal element of the swap matrix $|S|$ as a function of radius for a toy model with two instability crossings (semi-isotropic emission at $R = 10$ km, $\mu_r = 7 \times 10^4\,\mathrm{km}^{-1}\,\frac{R^4}{2r^4}$, $\lambda_r = 0.43\,\mu_r$).

5.3 Application to multi-energy spectra

Excited by the power the stability analysis showed confronted with simulations, in Ref [Sarikas 2011b], we have tried to apply it to the realistic supernova spectra, without any simplifications and to exploit the potential of the method in its fullness.

5.3.1 Realistic accretion-phase spectra

We have obtained spectra from a spherically symmetric simulation of a supernova evolved through the accretion phase performed by the Garching Astrophysics Group [Hudepohl 2010], using a $15\,M_\odot$ progenitor star. The artificial triggering of an explosion was not necessary because our interest is limited to the accretion phase, but otherwise the SN model is comparable to Ref. [Chakraborty 2011]. We have used several snapshots with the same outcome and we illustrate our findings with one taken at 280 ms post bounce.

We have fitted the neutrino fluxes to analytic functions of E and u. Typically the fitted functions undershoot the data, but not more than 10% in total luminosity. Considering the fact that only flux difference is important for the stability analysis, our approach is justified.

Figure 5.5 shows the spectra in energy and the u variable. A ν_e excess from deleptonization is evident and we have a $\bar{\nu}_e$ flux almost twice that of ν_x. The average energies for ν_e, $\bar{\nu}_e$ and ν_x are 15.3, 18.1, and 16.9 MeV respectively. To define u we had to choose the base radius R, usually referred as the radius of neutrino-sphere. In reality, the definition of a neutrino-sphere as a sphere of radius at which the optical depth of a neutrino ray equals 2/3 is not good

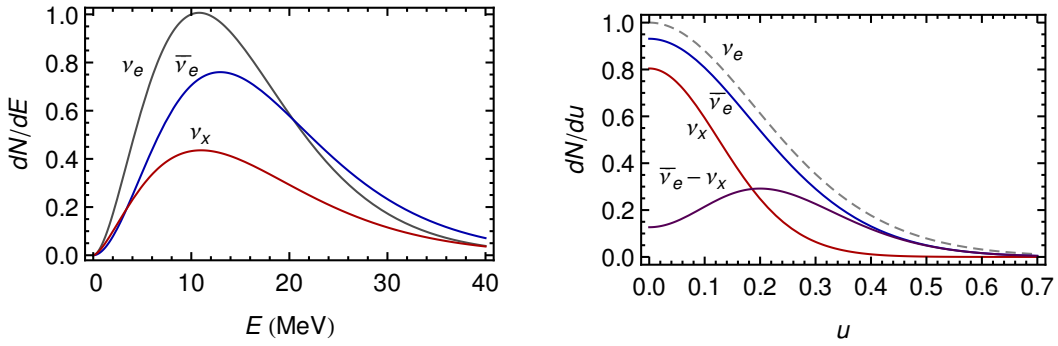

Figure 5.5: Flux spectra for our 280 ms SN model. The angle variable $0 \leq u \leq 1$ is based on $R = 44.7$ km.

enough for the purpose of studying the flux evolution. Moreover, the choice of R is rather arbitrary, as long is chosen far enough that neutrinos are free-streaming, but not before eventual flavor conversions. We choose $R = 44.7$ km as the radius closest to the PNS after which neutrinos just free-stream and the angular modes encompass most of the u range. Choosing it at even larger distance would correspond to more radially peaked spectra.

In the right panel of Figure 5.5 we show the the corresponding angular distributions. The deviation of the real spectra from the black body emission is significant[1]. In fact, isotropic emission from a neutrino sphere is not a good description because neutrino "last scattering surface" in the context of supernovae is actually a thick layer (as it is in general also for the photons of CMB). More energetic neutrinos are last scattered at larger distance than the low energy ones and the effect is also different for different species. Electron neutrinos emerge from a more broader region than the other flavors. That is why the ν_x emission is more "peaked" in the radial direction with respect to electron one [Raffelt 2001].

Moreover, the $\bar{\nu}_e$ and ν_x intensities are similar in the radial direction with the excess $\bar{\nu}_e$ flux largely arising from its broader angular distribution (larger emission region). Flavor oscillations depend on the difference of the e and x distributions, which is small in the radial direction. Interestingly, then, it turns out that the situation in the multi-angle analysis is more similar to a single angle one because the modes which are affected the most are concentrated around $u \sim 0.2$. The angular distributions do not cross, although in principle there could have been a forward ν_x excess.

The neutrino flux difference distribution $g(\omega, u)$ is shown in Fig. 5.6. It

[1] One should keep in mind that the typical model prevailing in the SN neutrino community was the black-body emission with all u-modes equally populated.

is negative for anti-neutrinos ($\omega < 0$) because $F_{\bar{\nu}_e} > F_{\bar{\nu}_x}$. For $\omega \sim 0.2$ km^{-1} there is a spectral crossing as a function of u, i.e. for large E the ν_x flux does exceed the ν_e flux in the forward direction.

Self-induced oscillations exchange the positive and negative parts of $g(\omega, u)$, leaving fixed the overall flavor content $\varepsilon = (F_{\nu_e} - F_{\nu_x})/(F_{\bar{\nu}_e} - F_{\nu_x}) - 1 = \int d\omega\, du\, g(\omega, u)$. Our $g(\omega, u)$ is mostly negative for anti-neutrinos and mostly positive for neutrinos, so collective oscillations largely correspond to pair conversions $\nu_e\bar{\nu}_e \leftrightarrow \nu_x\bar{\nu}_x$. Accretion-phase distributions are "single crossed" in this sense, i.e. $g(\omega, u)$ changes sign essentially only on the line $\omega = 0$, because of the large excess of the ν_e and $\bar{\nu}_e$ fluxes. Significant multiple crossings are typical for the cooling phase [Dasgupta 2009].

5.3.2 Results

Up to the MSW region, the matter effect is so large that the flux matrix $\mathsf{J}_{E,u}$ is very nearly diagonal in the weak-interaction basis, the usual approximation made in SN neutrino transport. Neutrinos remain stuck in flavor eigenstates unless the off-diagonal $\mathsf{J}_{E,u}$ elements start growing by the self-induced instability. To find the latter we linearize the EoM in the small off-diagonal amplitudes.

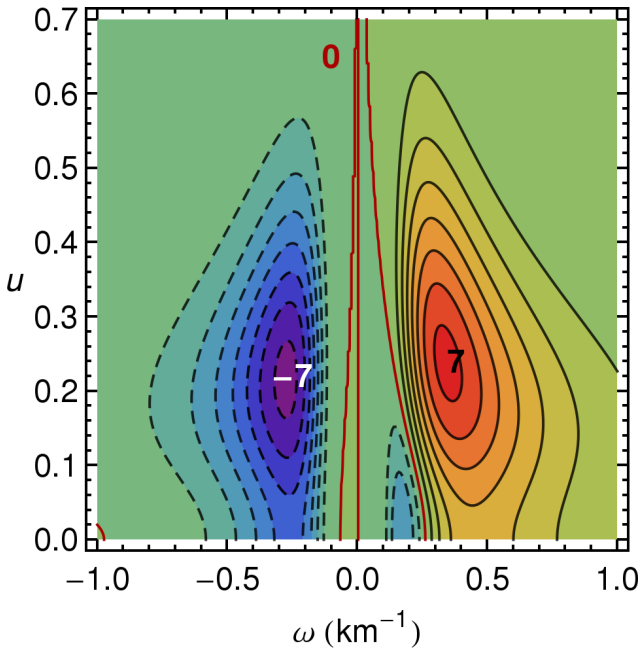

Figure 5.6: Distribution $g(\omega, u)$ describing the neutrino fluxes. The numbers denote the isocontours $g(\omega, u) = 0$, and the maximal and minimal values $g(\omega, u) = \pm 7$. The integral over negative frequencies is normalized to -1.

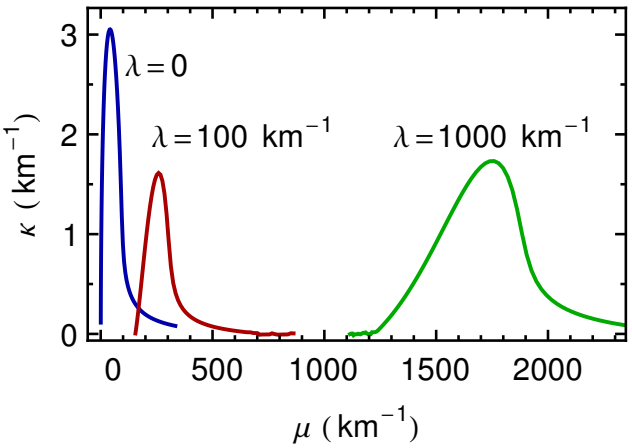

Figure 5.7: Growth rate κ for our SN model as a function of μ for various λ values as indicated.

Figure 5.7 shows $\kappa(\mu)$ for different values of λ. It is evident that increasing the matter potential, the $\kappa > 0$ region shifts toward larger μ values. The notion of matter multi-angle suppresion now also gets more concrete – what has used to be instable region, increased λ can make it stable again.

In Fig. 5.8 we show contours of κ in the (μ, λ) plane, just as in Fig.5.3. The difference is that for realistic spectra the integrals 5.22 cannot be determined analytically, but rather numerically. This affects significantly the CPU-time demands for the analysis, but we are still well bellow the values a typical simulation needs.

The findings are qualitativelly the same as in the previous section: for large μ and λ values, the system is unstable for $\lambda \sim \mu$. In other words, if the local neutrino number density is much smaller or much larger than the local electron density, the system is stable.

We also show the locus of $[\mu(r), \lambda(r)]$ along the radial direction. Since $\mu(r) \propto r^{-4}$, the red solid line in Fig. 5.8 is essentially the SN density profile. The step-like feature is the shock wave where the matter density drops by about an order of magnitude. Without matter ($\lambda = 0$), neutrinos would enter the instability strip at $\mu \sim 100$, corresponding to $r \sim 150$ km. We find similar results for all other snapshots at times 150, 400, 500 and 600 ms postbounce, i.e., neutrinos do not encounter a self-induced instability.

5.4 Summary

In order to interpret correctly and non-ambiguously the neutrino signal from a next galactic SN and to extract as much physics as possible from it, it is

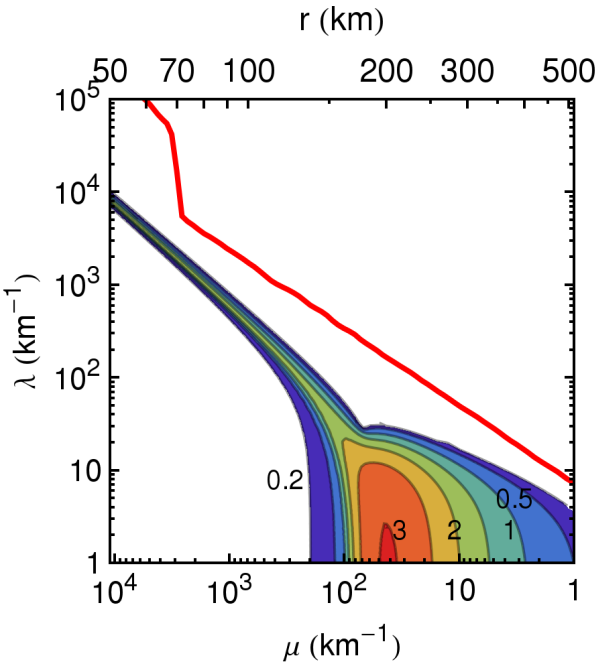

Figure 5.8: Contours for the growth rate κ in km^{-1}. Also shown is the profile for our 280 ms SN model. The vertical axis essentially denotes the density, the horizontal axis the radius ($\mu \propto r^{-4}$).

crucial to understand the evolution of neutrinos from the SN core to Earth detectors. The inherent non-linearity of the flavor evolution close to the SN core makes the problem very difficult to solve. That is why one usually resorts to various simplifications and approximations – single-energy, single-angle, semi-isotropic emission etc.

Linearized stability analysis [Banerjee 2011] makes it possible to treat the problem for the first time analytically without the need for any special assumptions. We have performed LSA for models from Ref. [Chakraborty 2011] and compared the results with the outcome of the numerical simulations and we have found a surprising level of agreement. We are able to predict whether and when the instability occurs without significant computing power and/or time. Of course, if we are interested in what happens *after* the instability has developed and the final outcome of the flavor evolution, we have to go back to simulations. Stability analysis can not answer those questions, but it can help reduce the computing time for the simulations: instead of evolving from an arbitrary radius (often deep inside the stability region), we can now run a simulation directly from the point close to instability and save all the time it would take to reach it in the first place.

We are now also able to perform the stability analysis of an arbitrary SN

model. For an accretion-phase SN model and concomitant neutrino fluxes with realistic energy and angle distributions, self-induced flavor conversions do not occur. One should apply this method to a broader class of models to see if our conclusion is generic. It also remains to extend a linearized analysis to cases without cylindrical symmetry of the angular distribution in view of Sawyer's concerns about a significant multi-angle instability [Sawyer 2009]. In realistic 3D models, the neutrino distribution is not cylindrically symmetric and even if this were the case, in principle even a small fluctuation could trigger a novel instability if it were to exist.

Recent experimental evidence suggests that the neutrino mixing angle θ_{13} is not very small [Fogli 2011], a point that should become clear with the ongoing round of reactor and long-baseline experiments. In this case one can distinguish the neutrino mass hierarchy in a high-statistics SN neutrino signal by the presence or absence of Earth matter effects, but only if collective oscillations do not exchange flavors before the MSW region. If the collective flavor swap were fully operational, the mass hierarchy could be distinguished for an extremely small value of θ_{13} where the MSW conversion is no longer adiabatic [Dasgupta 2008]. If θ_{13} is "large" in this sense, the absence of collective flavor oscillations during the SN accretion phase, if generic, is good news.

Conclusions

During my Ph.D. training I have contributed to the understanding of some cosmological and astrophysical aspects of neutrino physics. The central theme in both fields is the nontrivial evolution of mixed neutrinos giving rise to effects *a priori* not expected.

In the context of cosmology, I have worked in the Astroparticle physics group of the Physics Department of the University of Naples and the Naples section of the National Institute of Nuclear Physics (INFN). Together with Dr. Sergio Pastor (Institute for Particle Physics – IFIC, Valencia), we have examined the largest BBN-allowed asymmetries in the lepton sector. Electric charge neutrality constrains the electron asymmetry to be the same as the baryon asymmetry $\mathcal{O}(10^{-10})$, so virtually all the lepton asymmetry resides in the neutrino sector. All three species of neutrinos affect the expansion rate at the epoch of primordial nucleosynthesis, and electron flavor directly influences the neutron–proton balance. That is why the primordial abundances of light elements are sensitive to neutrino properties and it is possible to constrain them with present-day observations. Our results offer the best constraints on the initial and final lepton asymmetries, which depend on the value of the mixing angle θ_{13}. The values obtained are still orders of magnitude larger than the baryon asymmetry.

Since we explicitly followed the neutrino distributions, we were also able to put constraints on the maximal contribution of neutrinos to the total energy density of the Universe at the epoch of BBN, usually expressed by the effective number of neutrinos $N_{\rm eff}$. This is important because the same parameter can be obtained from other independent probes such as analysis of the cosmic microwave background. By the beginning of 2013, we expect the Planck mission to publish the most precise measurement of $N_{\rm eff}$ so far. Our results on $N_{\rm eff}$ will then be a clear guideline to whether or not the Planck value will signal the presence of extra contributions to the energy density at the epoch of BBN. A measurement larger then our constraint will be the first evidence of a new particle beyond the Standard Model.

Among all astrophysical environments, core-collapse supernovae are most important for the physics of neutrinos. The formation of a neutron star in the center of the explosion necessarily involves the emission of a vast number of neutrinos, which carry away the lepton number. For a typical supernova at a typical galactic distance of $\sim$10 kpc, existing neutrino detectors on Earth can see a high-statistics signal. The next such event will help us constrain many

of the still-unknown properties of neutrinos and may definitely answer some of the hot questions in neutrino physics. It will also provide a unique insight into the dynamics of the most energetic phenomena in the Universe, which are not yet completely understood by modern physics.

To properly understand the signal, we must account for all the effects neutrinos experience on their way from the supernova core to our detectors. To this end we perform numerical simulations. Very often, however, the CPU-time demands are so high, that we are led to various simplifications and approximations whose justification is sometimes arguable. Under the supervision of Prof. Georg Raffelt at the Max Planck Institute for Physics in Munich, I set out to understand the evolution of neutrinos from a supernova during the accretion phase, when the measured signal would also have its peak. This means that we must deal simultaneously with the high density of neutrinos themselves and the high density of the accreted matter.

We chose to work with realistic spectra obtained from a simulation performed by the core-collapse supernovae group of the Max Planck Institute for Astrophysics in Garching. The answer one expects only on the basis of qualitative estimates was virtually impossible to confirm through numerical simulations. It turned out that it is obtained much easier, if we analyze the problem from the stability point of view. We have proved that no neutrino flavor conversions happen in the region close enough to influence the simulations of supernovae, hence confirming their consistency. Our result also provided a definite answer on precisely what effects should be taken into account when interpreting the next supernova neutrino signal.

The equations of neutrino oscillations at high densities are the same for both the early Universe and supernovae. It is therefore interesting to note how the same underlying physics leaves different imprint in them. We have seen that we always have a first phase of the evolution in which the two refractive terms — of the ordinary matter and of other neutrinos — suppress the evolution so the system is virtually static. In the early Universe we then go inevitably through the epoch of flavor conversions and the presence of collisions. Their effectiveness is the reason why we speak about the degree of equilibration between different species and their impact on observables such as N_{eff}. On the other hand, in a supernova we have to pay attention to the delicate interplay between matter suppression and the neutrino self-interaction to understand if the evolution remains trivial or not. In the latter case, the non-homogeneity of the system is to blame for a possible development of spectral swaps, the interesting features in general very difficult to predict. Whether or not these effects happen and their possible impact on the observables to be measured in the near future was the main focus of my activity.

The ongoing experiments and observations promise a fruitful next few years. We expect reactor neutrino experiments (Double Chooz, Reno and Daya Bay) will determine the nonzero value of θ_{13} beyond a reasonable doubt on a year timescale, opening a path to determine the value of the CP-violating phase. Likewise, the Planck collaboration is scheduled to publish analysis of the cosmic microwave background with the highest precision ever. Within a few years, β-decay experiments, such as KATRIN, will reach a level of sensitivity on the absolute neutrino mass comparable to the cosmological bounds. The results of these efforts and possible surprises (a nearby supernova) will ensure the significant role of neutrinos in our understanding of the Universe. In the absence of new physics from the LHC, neutrino physics offers the strongest link between physics on the microscale and on the largest scales observable.

Bibliography

[Abazajian 2002] K. N. Abazajian, J. F. Beacom and N. F. Bell. *Stringent constraints on cosmological neutrino anti-neutrino asymmetries from synchronized flavor transformation.* Phys. Rev. **D66** 013008 (2002).

[Abazajian 2011] K. N. Abazajian, E. Calabrese, A. Cooray, F. De Bernardis, S. Dodelson *et al. Cosmological and Astrophysical Neutrino Mass Measurements.* Astropart. Phys. **35** 177–184 (2011).

[Abe 2011] K. Abe *et al. Indication of Electron Neutrino Appearance from an Accelerator-produced Off-axis Muon Neutrino Beam.* Phys. Rev. Lett. **107** 041801 (2011).

[Adam 2011] T. Adam *et al. Measurement of the neutrino velocity with the OPERA detector in the CNGS beam* (2011).

[Adamson 2007] P. Adamson, C. Andreopoulos, Arms *et al. Measurement of neutrino velocity with the MINOS detectors and NuMI neutrino beam.* Phys. Rev. D **76** 072005 (2007).

[Andreotti 2011] E. Andreotti, C. Arnaboldi, F. T. Avignone, M. Balata, I. Bandac *et al. 130Te Neutrinoless Double-Beta Decay with CUORICINO.* Astropart.Phys. **34** 822–831 (2011).

[Aver 2010] E. Aver, K. A. Olive and E. D. Skillman. *A New Approach to Systematic Uncertainties and Self-Consistency in Helium Abundance Determinations.* JCAP **1005** 003 (2010).

[Banerjee 2011] A. Banerjee, A. Dighe and G. Raffelt. *Linearized flavor-stability analysis of dense neutrino streams.* Phys. Rev. **D84** 053013 (2011).

[Barger 2003a] V. Barger, J. P. Kneller, P. Langacker, D. Marfatia and G. Steigman. *Hiding relativistic degrees of freedom in the early universe.* Phys. Lett. **B569** 123–128 (2003).

[Barger 2003b] V. Barger, J. P. Kneller, H.-S. Lee, D. Marfatia and G. Steigman. *Effective number of neutrinos and baryon asymmetry from BBN and WMAP.* Phys. Lett. **B566** 8–18 (2003).

[Bell 1999] N. F. Bell, R. R. Volkas and Y. Y. Y. Wong. *Relic neutrino asymmetry evolution from first principles.* Phys. Rev. **D59** 113001 (1999).

[Blondin 2003] John M. Blondin, Anthony Mezzacappa and Christine DeMarino. *Stability of standing accretion shocks, with an eye toward core collapse supernovae.* Astrophys.J. **584** 971–980 (2003). * Brief entry *.

[Bowen 2002] R. Bowen, S. H. Hansen, A. Melchiorri, J. Silk and R. Trotta. *The Impact of an extra background of relativistic particles on the cosmological parameters derived from microwave background anisotropies.* Mon. Not. Roy. Astron. Soc. **334** 760 (2002).

[Buras 2003] R. Buras, M. Rampp, H. Thomas Janka and K. Kifonidis. *Improved models of stellar core collapse and still no explosions: What is missing?* Phys.Rev.Lett. **90** 241101 (2003).

[Chakraborty 2011] S. Chakraborty, T. Fischer, A. Mirizzi, N. Saviano and R. Tomas. *Analysis of matter suppression in collective neutrino oscillations during the supernova accretion phase.* Phys. Rev. **D84** 025002 (2011).

[Cuoco 2004] A. Cuoco, F. Iocco, G. Mangano, G. Miele, O. Pisanti *et al. Present status of primordial nucleosynthesis after WMAP: results from a new BBN code.* Int. J. Mod. Phys. **A19** 4431–4454 (2004).

[Cyburt 2005] R. H. Cyburt, B. D. Fields, K. A. Olive and E. Skillman. *New BBN limits on physics beyond the standard model from He-4.* Astropart. Phys. **23** 313–323 (2005).

[Dasgupta 2008] B. Dasgupta, A. Dighe and A. Mirizzi. *Identifying neutrino mass hierarchy at extremely small theta(13) through Earth matter effects in a supernova signal.* Phys. Rev. Lett. **101** 171801 (2008).

[Dasgupta 2009] B. Dasgupta, A. Dighe, G. G. Raffelt and A. Yu. Smirnov. *Multiple Spectral Splits of Supernova Neutrinos.* Phys. Rev. Lett. **103** 051105 (2009).

[De Kerret 2011] H. De Kerret. *First Results from Double Chooz experiment* (2011).

[Dodelson 2003] Scott Dodelson. *Modern cosmology* (2003).

[Dolgov 1981] A. D. Dolgov. *Neutrinos in the Early Universe.* Sov. J. Nucl. Phys. **33** 700–706 (1981).

[Dolgov 2002a] A. D. Dolgov. *Neutrinos in cosmology.* Phys. Rept. **370** 333–535 (2002).

[Dolgov 2002b] A. D. Dolgov, S. H. Hansen, S. Pastor, S. T. Petcov, G. G. Raffelt *et al. Cosmological bounds on neutrino degeneracy improved by flavor oscillations.* Nucl. Phys. **B632** 363–382 (2002).

[Duan 2006] H. Duan, G. M. Fuller, J. Carlson and Y.-Z. Qian. *Simulation of Coherent Non-Linear Neutrino Flavor Transformation in the Supernova Environment. 1. Correlated Neutrino Trajectories.* Phys. Rev. **D74** 105014 (2006).

[Enqvist 1999] K. Enqvist, K. Kainulainen and A. Sorri. *On chaoticity of the amplification of the neutrino asymmetry in the early universe.* Phys. Lett. **B464** 199–205 (1999).

[Esteban-Pretel 2008a] A. Esteban-Pretel, A. Mirizzi, S. Pastor, R. Tomas, G. G. Raffelt *et al. Role of dense matter in collective supernova neutrino transformations.* Phys. Rev. **D78** 085012 (2008).

[Esteban-Pretel 2008b] Andreu Esteban-Pretel, Sergio Pastor, Ricard Tomas, Georg G. Raffelt and Gunter Sigl. *Decoherence in supernova neutrino transformations suppressed by deleptonization.* J.Phys.Conf.Ser. **136** 042073 (2008).

[Fischer 2010] T. Fischer, S. C. Whitehouse, A. Mezzacappa, F.-K. Thielemann and M. Liebendorfer. *Protoneutron star evolution and the neutrino driven wind in general relativistic neutrino radiation hydrodynamics simulations.* Astron. Astrophys. **517** A80 (2010).

[Fogli 2007] G. L. Fogli, E. Lisi, A. Marrone and A. Mirizzi. *Collective neutrino flavor transitions in supernovae and the role of trajectory averaging.* JCAP **0712** 010 (2007).

[Fogli 2008] G. L. Fogli, E. Lisi, A. Marrone, A. Mirizzi and I. Tamborra. *Low-energy spectral features of supernova (anti)neutrinos in inverted hierarchy.* Phys. Rev. **D78** 097301 (2008).

[Fogli 2011] G. L. Fogli, E. Lisi, A. Marrone, A. Palazzo and A. M. Rotunno. *Evidence of $\theta_{13} > 0$ from global neutrino data analysis* (2011).

[Fumagalli 2011] M. Fumagalli, J. M. O'Meara and J. X. Prochaska. *Detection of Pristine Gas Two Billion Years after the Big Bang* (2011).

[Hamann 2008] J. Hamann, J. Lesgourgues and G. Mangano. *Using BBN in cosmological parameter extraction from CMB: A Forecast for PLANCK.* JCAP **0803** 004 (2008).

[Hannestad 1995] S. Hannestad and J. Madsen. *Neutrino decoupling in the early universe.* Phys. Rev. **D52** 1764–1769 (1995).

[Hannestad 2006] S. Hannestad, G. G. Raffelt, G. Sigl and Y. Y. Y. Wong. *Self-induced conversion in dense neutrino gases: Pendulum in flavour space.* Phys. Rev. **D74** 105010 (2006).

[Hansen 2002] S. H. Hansen, G. Mangano, A. Melchiorri, G. Miele and O. Pisanti. *Constraining neutrino physics with BBN and CMBR.* Phys. Rev. **D65** 023511 (2002).

[Hudepohl 2010] L. Hudepohl, B. Muller, H. T. Janka, A. Marek and G. G. Raffelt. *Neutrino Signal of Electron-Capture Supernovae from Core Collapse to Cooling.* Phys. Rev. Lett. **104** 251101 (2010).

[Iocco 2009] F. Iocco, G. Mangano, G. Miele, O. Pisanti and P. D. Serpico. *Primordial Nucleosynthesis: from precision cosmology to fundamental physics.* Phys. Rept. **472** 1–76 (2009).

[Izotov 2010] Y. I. Izotov and T. X. Thuan. *The primordial abundance of 4He: evidence for non-standard big bang nucleosynthesis.* Astrophys. J. **710** L67–L71 (2010).

[Janka 2007] H.-T. Janka, K. Langanke, A. Marek, G. Martinez-Pinedo and B. Mueller. *Theory of Core-Collapse Supernovae.* Phys. Rept. **442** 38–74 (2007).

[Kolb 1990] E. W. Kolb and M. S. Turner. *The Early universe.* Front. Phys. **69** 1–547 (1990).

[Komatsu 2011] E. Komatsu *et al. Seven-Year Wilkinson Microwave Anisotropy Probe (WMAP) Observations: Cosmological Interpretation.* Astrophys. J. Suppl. **192** 18 (2011).

[Kraus 2005] Ch. Kraus, B. Bornschein, L. Bornschein, J. Bonn, B. Flatt *et al. Final results from phase II of the Mainz neutrino mass search in tritium beta decay.* Eur.Phys.J. **C40** 447–468 (2005).

[Lund 2010] T. Lund, A. Marek, C. Lunardini, H.-T. Janka and G. Raffelt. *Fast time variations of supernova neutrino fluxes and their detectability.* Phys. Rev. **D82** 063007 (2010).

[Maki 1962] Z. Maki, M. Nakagawa and S. Sakata. *ReM.s on the unified model of elementary particles.* Prog. Theor. Phys. **28** 870–880 (1962).

[Mangano 2002] G. Mangano, G. Miele, S. Pastor and M. Peloso. *A Precision calculation of the effective number of cosmological neutrinos.* Phys. Lett. **B534** 8–16 (2002).

[Mangano 2005] G. Mangano, G. Miele, S. Pastor, T. Pinto, O. Pisanti *et al. Relic neutrino decoupling including flavor oscillations.* Nucl. Phys. **B729** 221–234 (2005).

[Mangano 2011a] G. Mangano, G. Miele, S. Pastor, O. Pisanti and S. Sarikas. *Constraining the cosmic radiation density due to lepton number with Big Bang Nucleosynthesis.* JCAP **1103** 035 (2011).

[Mangano 2011b] G. Mangano, G. Miele, S. Pastor, O. Pisanti and S. Sarikas. *Updated BBN bounds on the cosmological lepton asymmetry for non-zero theta13* (2011).

[McKellar 1994] B. H. J. McKellar and M. J. Thomson. *Oscillating doublet neutrinos in the early universe.* Phys. Rev. **D49** 2710–2728 (1994).

[Mikheev 1986] S. P. Mikheev and A. Yu. Smirnov. *Resonant amplification of neutrino oscillations in matter and solar neutrino spectroscopy.* Nuovo Cim. **C9** 17–26 (1986).

[Nakamura 2010] K. Nakamura *et al. Review of particle physics.* J. Phys. **G37** 075021 (2010).

[Notzold 1988] D. Notzold and G. Raffelt. *Neutrino Dispersion at Finite Temperature and Density.* Nucl. Phys. **B307** 924 (1988).

[Nunokawa 2008] H. Nunokawa, S. J. Parke and J. W. F. Valle. *CP Violation and Neutrino Oscillations.* Prog. Part. Nucl. Phys. **60** 338–402 (2008).

[Pastor 2002] S. Pastor, G. G. Raffelt and D. V. Semikoz. *Physics of synchronized neutrino oscillations caused by selfinteractions.* Phys. Rev. **D65** 053011 (2002).

[Pastor 2009] S. Pastor, T. Pinto and G. G. Raffelt. *Relic density of neutrinos with primordial asymmetries.* Phys. Rev. Lett. **102** 241302 (2009).

[Pisanti 2008] O. Pisanti, A. Cirillo, S. Esposito, F. Iocco, G. Mangano *et al. PArthENoPE: Public Algorithm Evaluating the Nucleosynthesis of Primordial Elements.* Comput. Phys. Commun. **178** 956–971 (2008).

[Pontecorvo 1968] B. Pontecorvo. *Neutrino Experiments and the Problem of Conservation of Leptonic Charge.* Sov. Phys. JETP **26** 984–988 (1968).

[Raffelt 1993] G. Raffelt, G. Sigl and L. Stodolsky. *NonAbelian Boltzmann equation for mixing and decoherence.* Phys. Rev. Lett. **70** 2363–2366 (1993).

[Raffelt 1996] G. G. Raffelt. *Stars as laboratories for fundamental physics: The astrophysics of neutrinos, axions, and other weakly interacting particles* (1996).

[Raffelt 2001] G. G. Raffelt. *Muon-neutrino and tau-neutrino spectra formation in supernovae.* Astrophys. J. **561** 890–914 (2001).

[Raffelt 2007] G. G. Raffelt and G. Sigl. *Self-induced decoherence in dense neutrino gases.* Phys. Rev. **D75** 083002 (2007).

[Samuel 1993] S. Samuel. *Neutrino oscillations in dense neutrino gases.* Phys. Rev. **D48** 1462–1477 (1993).

[Sarikas 2011a] S. Sarikas and G. Raffelt. *Flavor stability analysis of supernova neutrino fluxes compared with simulations.* (2011). To appear in Proceedings of HaνSE workshop.

[Sarikas 2011b] S. Sarikas, G. G. Raffelt, L. Hudepohl and H.-T. Janka. *Flavor stability of a realistic accretion-phase supernova neutrino flux.* (2011).

[Sawyer 2009] R. F. Sawyer. *The multi-angle instability in dense neutrino systems.* Phys. Rev. **D79** 105003 (2009).

[Scholberg 2007] Kate Scholberg. *Supernova neutrino detection* (2007).

[Schwetz 2011] T. Schwetz, M. Tortola and J. W. F. Valle. *Where we are on θ_{13}: addendum to 'Global neutrino data and recent reactor fluxes: status of three-flavour oscillation parameters'.* New J. Phys. **13** 109401 (2011).

[Serpico 2004] P. D. Serpico, S. Esposito, F. Iocco, G. Mangano, G. Miele *et al. Nuclear reaction network for primordial nucleosynthesis: A Detailed analysis of rates, uncertainties and light nuclei yields.* JCAP **0412** 010 (2004).

[Serpico 2005] P. D. Serpico and G. G. Raffelt. *Lepton asymmetry and primordial nucleosynthesis in the era of precision cosmology.* Phys. Rev. **D71** 127301 (2005).

[Sigl 1993] G. Sigl and G. Raffelt. *General kinetic description of relativistic mixed neutrinos.* Nucl. Phys. **B406** 423–451 (1993).

[Simha 2008] V. Simha and G. Steigman. *Constraining The Universal Lepton Asymmetry*. JCAP **0808** 011 (2008).

[Steigman 2007] G. Steigman. *Primordial Nucleosynthesis in the Precision Cosmology Era*. Ann. Rev. Nucl. Part. Sci. **57** 463–491 (2007).

[Stodolsky 1987] L. Stodolsky. *On the Treatment of Neutrino Oscillations in a Thermal Environment*. Phys. Rev. **D36** 2273 (1987).

[Super-K] Super-Kamiokande webpage. http://www-sk.icrr.u-tokyo.ac.jp/sk/index-e.html.

[SNEWS] Supernova Early Warning System webpage. http://snews.bnl.gov/.

[Weinberg 2008] S. Weinberg. *Cosmology* (2008).

[Wolfenstein 1978] L. Wolfenstein. *Neutrino Oscillations in Matter*. Phys. Rev. **D17** 2369–2374 (1978).

[Wong 2002] Y. Y. Y. Wong. *Analytical treatment of neutrino asymmetry equilibration from flavor oscillations in the early universe*. Phys. Rev. **D66** 025015 (2002).

[Wurm 2011] Michael Wurm *et al. The next-generation liquid-scintillator neutrino observatory LENA* (2011).

Neutrino Oscillations at High Densities: Cosmological and Astrophysical Aspects

Abstract:

This doctoral thesis treats the effects of neutrino oscillations in the early universe and supernovae. The main probe for the context of the early universe is big bang nucleosynthesis (BBN). I explain the general link between neutrinos and BBN with an emphasis on the degeneracy between neutrino asymmetry and extra degrees of freedom. I show how the degenerate effects of both oscillations and collisions lead to observables detectable in the near future that brake this degeneracy and draw bounds on neutrino asymmetry and their contribution to the energy density of the universe in the current epoch. Considering astrophysical aspects, I analyze the significance of a proper treatment of neutrino evolution to understand the neutrino signal from the next galactic supernova (SN). I show the type of effects collective neutrino conversions can produce and the numerical difficulties confronted. Finally, I show how that stability analysis can complement a numerical treatment and provide definitive answers in some example cases.

Keywords: neutrinos, big bang nucleosynthesis, neutrino: supernova, neutrino: asymmetry, neutrino: oscillations, lepton number, physics of the early universe, primordial asymmetries, MSW effect, neutrino: mass hierarchy, stability analysis